The Dissertation Committee for Hongki Min
certifies that this is the approved version of the following dissertation:

Possible Ordered States in Graphene Systems

Committee:

Allan H. MacDonald, Supervisor

Leonard Kleinman, Supervisor

Qian Niu

Michael P. Marder

Brian A. Korgel

Possible Ordered States in Graphene Systems

by

Hongki Min, B.S.

DISSERTATION

Presented to the Faculty of the Graduate School of
The University of Texas at Austin
in Partial Fulfillment
of the Requirements
for the Degree of

DOCTOR OF PHILOSOPHY

THE UNIVERSITY OF TEXAS AT AUSTIN
August 2008

Dedicated to my family.

Acknowledgments

I must admit that pursuing my graduate studies here at the University of Texas at Austin gave me a rare opportunity to be under the tutelage of talented professors. However, today I feel chiefly indebted to my advisor Dr. Allan MacDonald for the patience and sincerity he has shown me in regard to this dissertation. I would like to take this opportunity to express my gratitude, first and foremost, to him for successfully guiding me through my graduate studies with his encouraging advice and propitious assistance.

My gratitude also goes to my group members, Yafis Barlas, Rafi Bistritzer, Ion Garate, Jeil Jung, Wei-Cheng Lee, Maria Moura, Tami Pereg-Barnea, Jung-Jung Su, Dagim Tilahun, Cheng-Ching Joseph Wang and Fan Zhang, and to my former group members, Rembert Duine, Paul Haney, Jason Hill, Sergey Maslennikov, Kentaro Nomura, Alvaro Nunez, Enrico Rossi, Yun-Pil Shim, Murat Tas and Janice Trinidad. I have realized that the friendship that we were able to establish during my stay here in Austin has truly inspired me in many ways. A special thanks to Ion Garate, my all-time officemate and great friend. I would also like to extend my thanks to Becky Drake for her kindness and the immense help she provided with administrative work.

I am grateful to my collaborators Bhagawan Sahu and Marco Polini for giving me their generous assistance and tireless support while we were working on several projects together. I am likewise thankful to my committee members Professors Leonard Kleinman, Qian Niu, Michael Marder and Brian Kogel, for their beneficent feedback on this dissertation.

To all the members of the UT Red Devils soccer team, I also wish to convey my overwhelming gratitude. All of you have been a great source of refreshment as I underwent through an otherwise tedious process of graduate studies.

I would also like to thank all my friends whom I have failed to mention, but will be remembered. The friendship we built during my stay in Austin shall forever be etched in my heart, as I hope that it does in yours as well. My stay here could not have ended quite meaningfully as it has today, had I not encountered my friends who brightened my life with laughter and joy.

Finally, I wish to thank my family for the unconditional love and unwavering support that they have shown me not only in the course of my studies, but in my life as well. They have truly been an infinite fountain of strength and hope for me. They have always stood by my side, especially in strenuous times I confronted during my studies. Even though I know that words are not enough to fully thank their unparalleled love and support, I want to offer them my immeasurable love and thanks.

HONGKI MIN
The University of Texas at Austin
August 2008

Possible Ordered States in Graphene Systems

Publication No. ____________________

Hongki Min, Ph.D.
The University of Texas at Austin, 2008

Supervisors: Allan H. MacDonald
Leonard Kleinman

Graphene is a two dimensional honeycomb lattice of carbon atoms which has recently attracted considerable attention because of rapid experimental progress, and because of its novel physical properties. In this work, we will discuss recent theoretical work in which we have proposed new types of ordered electronic states in graphene bilayers, including pseudospin magnets which show spontaneous charge transfer between two layers, and excitonic superfluids which could have remarkably high transition temperatures. This work will conclude with some speculations on the possibility of radically new types of electronic devices in these systems whose operation is based on collective electronic behavior.

Table of Contents

Acknowledgments **v**

Abstract **vii**

List of Tables **xi**

List of Figures **xii**

Chapter 1. Introduction **1**

1.1 Why graphene? 1

1.2 Outline of thesis 4

Chapter 2. Electronic Structure of Graphene Monolayers **7**

2.1 Introduction 8

2.2 Tight-binding model 10

2.2.1 Two-center hopping 10

2.2.2 Atomic spin-orbit interactions 12

2.2.3 External gate electric fields 12

2.3 Perturbation theory 13

2.3.1 Unperturbed Hamiltonian matrix at K and K' 13

2.3.2 Low-energy effective Hamiltonian 14

2.4 *Ab initio* density functional theory calculations 17

2.5 Discussion 19

Chapter 3. Electronic Structure of Graphene Bilayers **23**

3.1 Introduction 23

3.2 *Ab initio* density functional theory calculations 26

3.2.1 External electric fields 26

3.2.2 Energy bands 28

3.2.3 Evolution of tight-binding model parameters with U_{ext} . 30
3.3 Screening theories 33
3.3.1 Continuum Hartree potential models 33
3.3.2 Lattice Hartree potential models 37
3.4 Discussion 42

Chapter 4. Electronic Structure of Graphene Multilayers 44
4.1 Introduction 44
4.2 π-orbital continuum model 45
4.2.1 Stacking diagrams 45
4.2.2 Energy band structure 48
4.2.3 Landau level spectrum 57
4.2.4 Quantum Hall conductivity 63
4.3 Chiral decomposition of energy spectrum 65
4.3.1 Partitioning rules 66
4.3.2 Degenerate state perturbation theory 68
4.4 Discussion 76
4.4.1 Effects of remote hopping 76
4.4.2 Quantum Hall effect 77
4.4.3 Effects of the same stacking inside 80
4.4.4 Summary 81

Chapter 5. Pseudospin Magnetism in Graphene 83
5.1 Introduction 83
5.2 Chiral two-dimensional electron system Hartree-Fock Theory . 85
5.3 Pseudospin magnet phase diagram 88
5.4 Discussion 93

Chapter 6. Exciton Condensation in Graphene Bilayers 96
6.1 Introduction 96
6.2 Two-band mean-field theory 100
6.3 Linearized gap equation 104
6.4 Phase stiffness 104
6.5 Discussion 107

Chapter 7. Conclusion **110**

Appendices **113**

Appendix A. Tight-binding Model **114**
- A.1 Basic formulation 114
- A.2 Application to graphene 116

Appendix B. *Ab initio* Electronic Structure Calculation **118**
- B.1 Density functional theory 118
  - B.1.1 Hohenberg-Kohn theorem 118
  - B.1.2 Kohn-Sham equations 119
  - B.1.3 Exchange-correlation energy 122
- B.2 Pseudopotential theory 123

Appendix C. Hartree-Fock Theory **126**
- C.1 Many-body operators 126
  - C.1.1 One-body operators 126
  - C.1.2 Two-body operators 128
- C.2 Hartree-Fock theory 130
  - C.2.1 Hartree terms 130
  - C.2.2 Fock terms 131
  - C.2.3 Application to 2D electron gas with pseudospin 132

Appendix D. Two-component Formalism **134**
- D.1 Hamiltonian 134
- D.2 Green's function 135
- D.3 Berry curvature 135

Bibliography **138**

Index **146**

Vita **148**

List of Tables

2.1 Two-center matrix elements for hoping between s and p orbitals along a direction specified by the unit vector (n_x, n_y, n_z). . . . 11

2.2 Matrix elements of $\boldsymbol{L} \cdot \boldsymbol{S}$ for p orbitals. 12

2.3 Matrix elements of $eE_{ext}z$. The only nonvanishing matrix element is the one between the s and p_z orbitals to which the value $eE_{ext}z_0$ is assigned. 13

2.4 Tight-binding model matrix elements at the K and K' points in the absence of spin-orbit interactions and external electric fields. The first (second) sign corresponds to the $K(K')$ point. 14

2.5 Unnormalized unperturbed eigenvectors at the K and K' points arranged in increasing order of energies assuming $0 < \gamma_+ < 2\beta < \gamma_-$. The first (second) sign corresponds to the $K(K')$ point. 15

2.6 The effective spin-orbit matrix at the K point. 15

2.7 The effective spin-orbit matrix at K' point. 16

2.8 Hopping parameters for a graphene taken from Ref. [21]. . . . 16

4.1 Chirality decomposition for $N = 3, 4, 5, 6$ layer stacks. 68

List of Figures

1.1 Energy band structure of graphene at low energies. Adapted from Ref. [3]. 1

1.2 Hall conductivity σ_{xy} and longitudinal resistivity ρ_{xx} of graphene as a function of carrier concentration at $B = 14$ T and $T = 4$ K. Inset: σ_{xy} in bilayer graphene for which the quantization sequence is normal except that $\sigma_{xy} = 0$ is absent. Adapted from Ref. [16]. 2

1.3 Charge carrier density (open circles) and mobility (filled circles) of graphene as a function of gate voltage. The solid line corresponds to the estimated charge induced by the gate voltage. Adapted from Ref. [17]. 3

1.4 Energy gap vs ribbon width. The inset shows energy gap vs relative angle for the device sets. Dashed lines in the inset show the value of the energy gap as predicted by the empirical scaling of the energy gap vs ribbon width. Adapted from Ref. [18]. . . 4

2.1 Graphene band structure for $\xi = 0$ and $\xi = 300\xi_0$ using the tight-binding model with nonorthogonal orbitals. Hopping parameters were taken from Ref. [21] and $\xi_0 = 6$ meV was used for the atomic spin-orbit coupling strength. 18

2.2 Energy gap for $\lambda_R = 0$ as a function of spin-orbit coupling strength from the *ab initio* calculation, from the tight-binding model with nonorthogonal orbitals, and from the analytic expression in Eq. (2.1). 20

3.1 Structure of a graphene bilayer with honeycomb lattice constant $a = 2.46$ Å and interlayer separation $d = 3.35$ Å. 24

3.2 Schematic illustration of a circuit with a bilayer graphene channel sensitive to an external gate voltage. The graphene channel is separated from the front and back gates by a SiO_2 layer. The channel resistance change will be rapid and large when the graphene channel is undoped and isolated from the gate electrodes, as illustrated here. In this case, the total charge density in the bilayer system is fixed and the chemical potential lies in the gap opened by the gate voltage. This geometry could also be used to capacitively probe the correlation physics of the isolated bilayer system, as discussed in the text. 25

3.3 An averaged Coulomb potential of a cross section vs z for total external potential $U_{ext} = 0$ eV and $U_{ext} = 1$ eV. Here, z_0 is the superlattice period and the cross section was chosen to include equal number of atoms in each layer. 27

3.4 Bilayer graphene band structure in the absence of an external electric field. 29

3.5 Bilayer graphene band structure near the K point for U_{ext}=0, 0.5, and 1 eV. 30

3.6 (a) Evolution of the graphene bilayer screened on-site energy difference U, extracted from the *ab initio* DFT bands as explained in the text, with the external potential U_{ext}. The external potential is strongly screened. (b) Evolution of the interlayer tunneling amplitude γ_1 with U_{ext}. 31

3.7 Comparison of band gap as a function of the on-site energy difference U obtained from the *ab initio* DFT calculations (open circles) with the tight-binding result for $\gamma_3 = 0$ (dashed line) and $\gamma_3 = 0.3$ eV (solid line). 32

3.8 The ratio of the external electric potential U_{ext} to the interlayer energy difference inferred from the *ab initio* DFT calculation compared with the value of the same ratio in tight-binding model self-consistent Hartree calculations, both with and without crystalline inhomogeneity corrections. The tight-binding model calculations used γ_0=2.6 eV for the intralayer tunneling amplitude, γ_1=0.34 eV for the interlayer tunneling amplitude, and γ_3=0.3 eV for the interlayer A-$\tilde{B}$ coupling. 35

3.9 Splitting of Hartree potentials $\big(\epsilon_l^{(H)} - \epsilon_h^{(H)}\big)/\big(\epsilon_l^{(H)} + \epsilon_h^{(H)}\big)$ as a function of (a) the external electric potential U_{ext} and (b) the corresponding density inhomogeneity $\big(\Delta n_l - \Delta n_h\big)/\big(\Delta n_l + \Delta n_h\big)$ in the lattice Hartree potential model. 41

4.1 (a) Energetically favored stacking arrangements for graphene sheets. The honeycomb lattice of a single sheet has two triangular sublattices, labeled by α and β. Given a starting graphene sheet, the honeycomb lattice for the next layer is usually positioned by displacing either α or β sublattice carbon atoms along a honeycomb edge. There are therefore in three distinct two-dimensional (2D) sheets, labeled by A, B, and C. Representative α and β sublattice positions in A, B, and C layers are identified in this illustration. It is also possible to transform between layer types by rotating by $\pm 60^\circ$ about a carbon atom on one of the two sublattices. (b) Each added layer cycles around this stacking triangle in either the right-handed or the left-handed sense. Reversals of the sense of this rotation tend to increase the number of low-energy pseudospin doublets N_D. In graphite, Bernal (AB) stacking corresponds to a reversal at every step and orthorhombic (ABC) stacking corresponds to no reversals. . . 46

4.2 Stacking sequences and linkage diagrams for $N = 3, 4, 5$ layer stacks. The low-energy band and Landau level structures of a graphene stacks with nearest-neighbor hopping are readily read off these diagrams as explained in the text. Shaded ovals link α and β nearest interlayer neighbors. 47

4.3 Band structure near the K point for (a) trilayer and (b) tetralayer graphene with AA stacking for nearest intralayer neighbor hopping $t = 3$ eV and nearest interlayer neighbor hopping $t_\perp = 0.1t$. 50

4.4 Band structure near the K point for (a) trilayer and (b) tetralayer graphene with AB stacking for nearest intralayer neighbor hopping $t = 3$ eV and nearest interlayer neighbor hopping $t_\perp = 0.1t$. 53

4.5 Band structure near the K point for (a) trilayer and (b) tetralayer graphene with ABC stacking for nearest intralayer neighbor hopping $t = 3$ eV and nearest interlayer neighbor hopping $t_\perp = 0.1t$. 56

4.6 Band structure near the K point for tetralayer graphene with (a) ABCB stacking and (b) ABBC stacking for nearest intralayer neighbor hopping $t = 3$ eV and nearest interlayer neighbor hopping $t_\perp = 0.1t$. 57

4.7 Landau levels of (a) trilayer and (b) tetralayer graphene with AA stacking for nearest intralayer neighbor hopping $t = 3$ eV and nearest interlayer neighbor hopping $t_\perp = 0.1t$. Landau levels were shown up to $n = 10$. 59

4.8 Landau levels of (a) trilayer and (b) tetralayer graphene with AB stacking for nearest intralayer neighbor hopping $t = 3$ eV and nearest interlayer neighbor hopping $t_\perp = 0.1t$. Landau levels up to $n = 10$ are shown. 61

4.9 Landau levels of (a) trilayer and (b) tetralayer graphene with ABC stacking for nearest intralayer neighbor hopping $t = 3$ eV and nearest interlayer neighbor hopping $t_\perp = 0.1t$. Landau levels up to $n = 10$ are shown. 63

4.10 Landau levels of tetralayer graphene with (a) ABCB stacking and (b) ABBC stacking for nearest intralayer neighbor hopping $t = 3$ eV and nearest interlayer neighbor hopping $t_\perp = 0.1t$. Landau levels up to $n = 10$ are shown. 64

4.11 Landau level spectrum near the K valley as a function of γ_3 for an AB stacked bilayer for (a) $B = 0.1$ T and (b) $B = 1$ T. Here $t = 3$ eV, $t_\perp = 0.1t$, and $\omega_c = eB/mc$, with $m = t_\perp/2v^2$, were used. 77

4.12 Landau level spectrum near the K valley as a function of γ_2 for an ABA stacked trilayer for (a) $B = 1$ T and (b) $B = 10$ T. Here $t = 3$ eV, $t_\perp = 0.1t$, and $\omega_c = eB/mc$, with $m = t_\perp/2v^2$, were used. Note that for this case the Landau level structures near K and K' valleys are not identical. 78

4.13 Noninteracting system Hall conductivity as a function of the Fermi energy for all inequivalent four-layer graphene stacks when $B = 10$ T, $t = 3$ eV, and $t_\perp = 0.1t$. The dependence of the Hall conductivity on Fermi energy is simply related to the dependence of the Hall conductivity on total electron density. The Hall conductivity calculations shown in this figure assume neutralizing ionized donors spread equally between the four layers. 79

4.14 Stacking diagrams for tetralayer graphene with (a) ABBC stacking and (b) ABBA stacking. Shaded ovals link nearest interlayer neighbors. 80

5.1 Pseudospin orientation in a graphene bilayer broken symmetry state. In this figure the arrows represent both the magnitude and the direction of the $\hat{x}$-$\hat{y}$ projection of the pseudospin orientation $\hat{n}$ as obtained from a mean-field-theory calculation for a neutral, unbiased bilayer with coupling constant $\alpha = 1$. The arrows are shorter in the core of the momentum space vortex because the pseudospins in the core have rotated spontaneously toward the $\hat{z}$ or $-\hat{z}$ direction. 85

5.2 Ratio of exchange kernels, $F_\perp(k, k')/F_z(k, k')$ of the bilayer chiral (left) and non-chiral (right) model with $k_c d = 0.2$. Here the non-chiral model means no $\cos(J\phi)$ term in $F_\perp(k, k')$ in Eq. (5.9). 89

5.3 Phase diagram of C2DES's with $J = 2$ and $J = 1$. For the $J = 2$ bilayer case we have taken $\bar{d} = 0.2$. Pseudospin magnetism occurs at strong coupling α and weak doping f. ($1+f = n_{\uparrow}+n_{\downarrow}$ where the pseudospin density $n_{\sigma} = \sum_{\boldsymbol{k},i}\langle\hat{c}^{\dagger}_{\boldsymbol{k},i,\sigma}\hat{c}_{\boldsymbol{k},i,\sigma}\rangle/\mathcal{N}$ and $\mathcal{N} = \sum_{\boldsymbol{k},i} 1$.) In the $J = 2$ bilayer case, the Hartree potential favors smaller total polarization so that the initial normal (N) state instability (blue separatrix) is to antiferromagnetic (AF) states in which the pseudospin polarizations of different valley and spin components cancel. At larger α, the normal state is unstable (green separatrix) to ferromagnetic (F) pseudospin states. In the $J = 1$ monolayer case $\bar{d} = 0$ so the phase boundaries (red separatrix) of F and AF broken-symmetry states coincide. . . 90

5.4 Condensation energy per electron $\delta\varepsilon$ [in units of $\varepsilon_0(k_{\rm c})$] as a function of α for an undoped ($f = 0$) $J = 2$ C2DES for both ferro state. 91

5.5 Condensation energy per electron $\delta\varepsilon$ [in units of $\varepsilon_0(k_{\rm c})$] as a function of α for an undoped ($f = 0$) $J = 2$ C2DES for antiferro state. 92

5.6 Metastable configurations of the pseudospin ferromagnet as a function of bias voltage $V_{\rm g}$ [in units of $\varepsilon_0(k_{\rm c})$] with $\alpha = 1$ and $f = 0$. We find self-consistent solutions of the gap equations (5.7)-(5.8) in which the pseudospin polarization has the same sense in all four components (ferromagnetic), in three of the four components (ferrimagnetic), or in half of the four components (antiferromagnetic). 93

5.7 In-plane projected pseudospin orientation of (a) $J = 1$, (b) $J = 2$, (c) $J = 3$ and (d) $J = 4$ chiral two-dimensional electron systems for $V_{\rm g} = 0$, $\alpha = 1$ and $f = 0$. For $J > 1$, the arrows are shorter near the core of the momentum space vortex because the pseudospins near the core have rotated spontaneously toward $\hat{z}$ or $-\hat{z}$ direction indicating the pseudospin magnetic state. . . . 95

6.1 Left: Schematic illustration of a graphene bilayer exciton condensate channel in which two single-layer graphene sheets are separated by a dielectric (SiO_2 in this illustration) barrier. We predict that electron and hole carriers induced by external gates will form a high-temperature exciton condensate. Right: The two band model in which the two remote bands indicated by dashed lines are neglected. 98

6.2 Normal to superfluid phase diagram showing the dependence of the critical temperature T_c in Kelvin on the distance between layers d in nm and external bias electric field E_{ext} in V/nm. . 100

6.3 Mean-field theory energy bands for $\alpha = 1$, $T = 0$ and $k_{\rm F}^{(0)} d = 1$. ($E_{\rm F}^{(0)} = \hbar v k_{\rm F}^{(0)} = V_g/2$.) Note that $k_{\rm F} < k_{\rm F}^{(0)}$ because E_{ext} is screened. 103

6.4 Mean-field critical temperature (red solid line with circles), upper bound of KT temperature (blue dotted line with squares), KT temperature temperature (black dashed line with stars) in Kelvin as a function of interlayer separation d in nm for an external bias electric field $E_{ext} = 0.5$ V/nm. 105

7.1 Pseudospin (charge) polarization $\zeta = (n_\uparrow - n_\downarrow)/(n_\uparrow + n_\downarrow)$ of a graphene bilayer as a function of gate voltage $\bar{V}_{\rm g}$ [in units of $\varepsilon_0(k_{\rm c})$] assuming fully polarized ferromagnetic states with $\alpha = 1$ and $f = 0$. 111

Chapter 1

Introduction

1.1 Why graphene?

Graphene[1] is a two-dimensional honeycomb lattice of carbon atoms that has attracted considerable attention recently because of experimental progress [4–7] that has raised hopes for applications in nanoelectronics, and because of exotic chiral features [8–15] in its electronic structure.

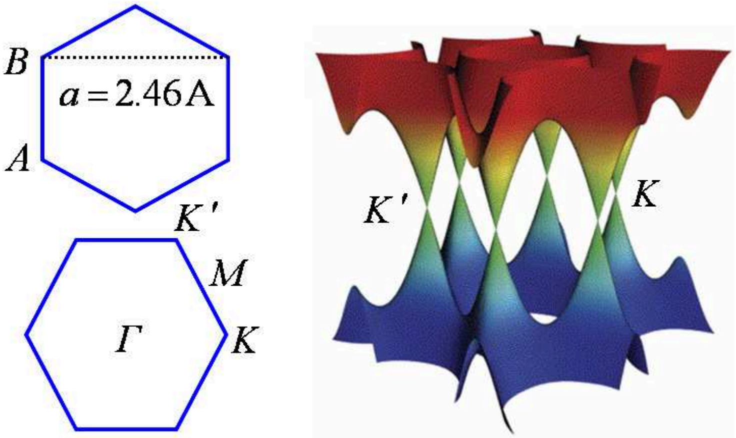

Figure 1.1: Energy band structure of graphene at low energies. Adapted from Ref. [3].

In a single-layer graphene, the A sublattice to B sublattice hopping am-

---

[1] For recent technical and popular reviews, see [1–3]

plitude vanishes at two inequivalent points K and K' on the edge of the honeycomb lattice Brillouin zone (BZ); away from these points, the hopping amplitude grows linearly with wavevector and has a phase which winds along with the orientation of the wavevector measured from the high-symmetry points. The band structure of an isolated graphene layer is therefore described at low energies by a two-dimensional massless Dirac equation with linear dispersion centered on the hexagonal corners of the honeycomb lattice Brillouin zone (Fig. 1.1). This property is responsible for many of the novel electronic properties of graphene sheets.

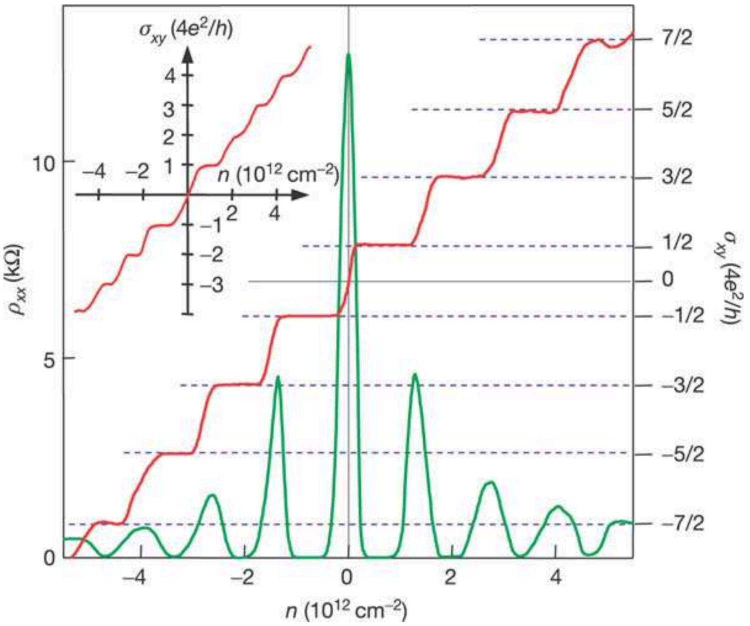

Figure 1.2: Hall conductivity σ_{xy} and longitudinal resistivity ρ_{xx} of graphene as a function of carrier concentration at $B = 14$ T and $T = 4$ K. Inset: σ_{xy} in bilayer graphene for which the quantization sequence is normal except that $\sigma_{xy} = 0$ is absent. Adapted from Ref. [16].

One of the most remarkable properties of graphene is its half integer quantum Hall effect (Fig. 1.2), confirmed by recent experiments [16, 17]. This electronic property follows directly from the system's Dirac-like band structure [8, 9].

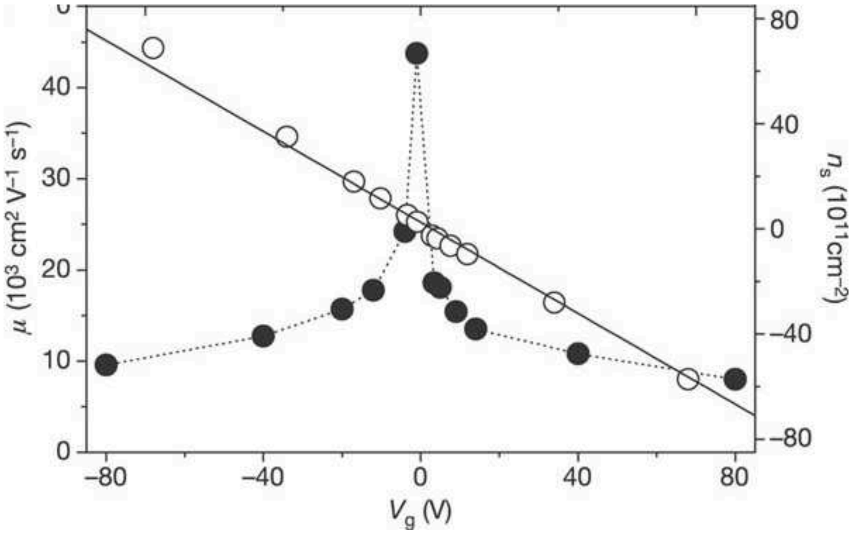

Figure 1.3: Charge carrier density (open circles) and mobility (filled circles) of graphene as a function of gate voltage. The solid line corresponds to the estimated charge induced by the gate voltage. Adapted from Ref. [17].

High mobilities ($\mu > 10^4$ cm^2/Vs which is already an order of magnitude higher than that of modern Si transistors) make graphene a promising candidate for future electronic applications (Fig. 1.3). Moreover, μ remains high even at highest electric-field-induced concentrations ensuring ballistic transport on a submicrometer scale even at room-temperature.

From the device application point of view, the fact that graphene remains metallic even at the neutrality point is a major problem because it

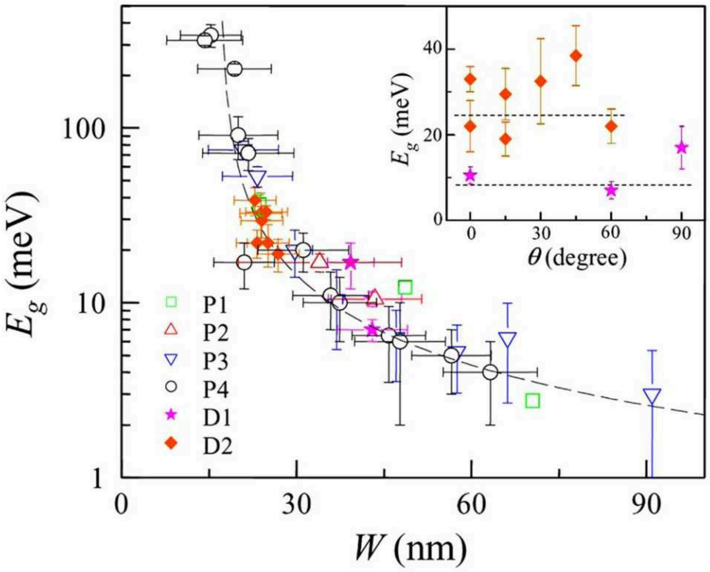

Figure 1.4: Energy gap vs ribbon width. The inset shows energy gap vs relative angle for the device sets. Dashed lines in the inset show the value of the energy gap as predicted by the empirical scaling of the energy gap vs ribbon width. Adapted from Ref. [18].

means that a graphene-based transistor cannot be closed by any external gate voltage. One way to overcome this problem is to engineer the semiconductor gaps by spatial confinement (Fig. 1.4), which allows the graphene-based transistor to operate in the same way as Si-based ones.

1.2 Outline of thesis

Here we give an outline of this work.

In chapter 2 we study effects of spin-orbit interactions in an isolated graphene sheet. Starting from a microscopic tight-binding model and using second order perturbation theory, we derive explicit expressions for the intrinsic and Rashba spin-orbit interaction induced gaps. *Ab initio* electronic structure calculations were performed as a partial check on the validity of the tight-binding model.

In chapter 3 we study the gate-voltage induced energy gap that occurs in graphene bilayers using *ab initio* density functional theory. We also quantify the role of crystalline inhomogeneity using a tight-binding model self-consistent Hartree calculation.

In chapter 4 we study the electronic structure of arbitrarily stacked graphene multilayers. Using a π-orbital continuum model and degenerate state perturbation theory, we show that the low-energy electronic structure of arbitrarily stacked graphene multilayers consists of chiral pseudospin doublets with a conserved chirality sum.

In chapter 5 we predict that neutral graphene bilayers are pseudospin magnets in which the charge density-contribution from each valley and spin spontaneously shifts to one of the two layers. The band structure of this system is characterized by a momentum-space vortex which is responsible for unusual competition between kinetic and interaction energies leading to symmetry breaking in the vortex core.

In chapter 6 we discuss about a possibility of exciton condensation in graphene bilayers. We present estimates which suggest that the Kosterlitz-Thouless temperatures of these two-dimensional counterflow superfluids can approach room temperature, which will be very useful in future electronic device applications.

In chapter 7 we will conclude this work by proposing a new electronic device scheme based on collective behavior of many electrons.

Chapter 2

Electronic Structure of Graphene Monolayers

In this chapter, we discuss about the electronic structure of graphene monolayers focusing on the effects of spin-orbit interactions. Starting from a microscopic tight-binding model and using second order perturbation theory, we derive explicit expressions for the intrinsic and Rashba spin-orbit interaction induced gaps in the Dirac-like low-energy band structure of an isolated graphene sheet. The Rashba interaction parameter is first order in the atomic carbon spin-orbit coupling strength ξ and first order in the external electric field E_{ext} perpendicular to the graphene plane, whereas the intrinsic spin-orbit interaction which survives at $E_{ext} = 0$ is second order in ξ. The spin-orbit terms in the low-energy effective Hamiltonian have the form proposed recently by Kane and Mele. *Ab initio* electronic structure calculations were performed as a partial check on the validity of the tight-binding model. [1]

---

[1] The contents of this chapter are based on the article: Hongki Min, J. E. Hill, N. A. Sinitsyn, B. R. Sahu, Leonard Kleinman, and A. H. MacDonald, *Intrinsic and Rashba spin-orbit interactions in graphene sheets*, Phys. Rev. B **74**, 165310 (2006).

2.1 Introduction

In a recent paper, Kane and Mele [8] showed that symmetry allowed spin-orbit interactions can generate an energy gap and convert graphene from a two dimensional zero gap semiconductor to an insulator with a quantized spin Hall effect [13]. The quantized spin Hall conductivity can be zero or nonzero, depending on the relative strength of intrinsic and Rashba spin-orbit interactions. The temperature at which the spin Hall effect can be observed, and the sample quality requirements for its occurrence, depend on the absolute magnitude of these two spin-orbit interaction terms in the band structure. (Kane and Mele [8] argued on the basis of rough estimates of the spin-orbit interaction scale, that the quantum spin Hall effect in graphene should be observable at relatively accessible temperatures of the order of 1°K.) Motivated by the fundamental interest associated with the spin Hall effect and spin-orbit interactions in graphene, we have attempted to estimate, on the basis of microscopic considerations, the strength of both interactions.

In order to allow for a Rashba interaction, we account for the presence of an external gate electric field E_{ext} of the type used experimentally in graphene to move the Fermi energy away from the Dirac point. (Importantly this electric field explicitly removes inversion through the graphene plane from the symmetry operations of the system.) Then, starting from a microscopic tight-binding model with atomic spin-orbit interactions of strength ξ, we use perturbation theory to derive expressions for the spin-orbit coupling terms that appear in the low-energy Hamiltonian. At leading order in ξ only the

Rashba spin-orbit interaction term ($\propto E_{ext}$) appears. The intrinsic ($E_{ext} = 0$) spin-orbit coupling has a leading contribution proportional to ξ^2. Both terms have the form proposed by Kane and Mele [8] on the basis of symmetry considerations. According to our theory the respective coupling constants are given by the following expressions:

$$\lambda_{SO} = \frac{|s|}{18(sp\sigma)^2}\,\xi^2 \ , \tag{2.1}$$

and

$$\lambda_R = \frac{eE_{ext}z_0}{3(sp\sigma)}\,\xi, \tag{2.2}$$

where $|s|$ and $(sp\sigma)$ are tight-binding model parameters explained more fully below, E_{ext} is a perpendicular external electric field, and z_0 is proportional to the atomic size of carbon. The coupling constants λ_{SO} and λ_R have numerical values $\sim$ 100 times smaller and $\sim$ 100 times larger, respectively, than the estimates of Kane and Mele [8] with $\lambda_{SO} < \lambda_R$ at the largest reasonable values of E_{ext}. Together, these estimates suggest that the quantum spin Hall effect will be observable in ideal samples only at temperatures below ~ 0.01°K in a zero-field limit.

This chapter is organized as follows. In Section 2.2, we briefly summarize the tight-binding model used to represent graphene in this chapter. Section 2.3 describes some details of the perturbation theory calculation. In Section 2.4, we discuss *ab initio* density functional theory calculations we have carried out as a partial check on the tight-binding model and on the atomic approximation for spin-orbit interactions used in the perturbation theory calculations. We conclude in Section 2.5 with a brief summary and present our conclusions.

2.2 Tight-binding model

2.2.1 Two-center hopping

For our analytic perturbation theory calculations we choose the simplest possible tight-binding model with carbon s and p orbitals, a two-center Slater-Koster approximation [19] for nearest-neighbor hopping, and orthogonality between Wannier functions centered on different sites assumed. This gives a tight-binding Hamiltonian of the form

$$\begin{aligned} H_{A,\mu;A,\mu'}(\boldsymbol{k}) = H_{B,\mu;B,\mu'}(\boldsymbol{k}) &= t_{\mu}\delta_{\mu,\mu'}, \\ H_{A,\mu;B,\mu'}(\boldsymbol{k}) = H^{*}_{B,\mu';A,\mu}(\boldsymbol{k}) &= \sum_{i=1}^{3} e^{i\boldsymbol{k}\cdot\boldsymbol{N}_i} t_{\mu,\mu'}(\boldsymbol{N}_i), \end{aligned} \tag{2.3}$$

where μ, μ' label the four orbitals on each site, A and B represent the two distinct sites in the honeycomb lattice unit cell, and $\boldsymbol{N}_i$ is one of the three vectors connecting a lattice site and its near neighbors. We choose a coordinate system in which the honeycomb's Bravais lattice has primitive vectors

$$\boldsymbol{a}_1 = a(1,0)\ , \qquad \boldsymbol{a}_2 = a\Big(\frac{1}{2}, \frac{\sqrt{3}}{2}\Big), \tag{2.4}$$

where $a = 2.46$Å is the lattice constant of graphene. The corresponding reciprocal lattice vectors are

$$\boldsymbol{b}_1 = \frac{4\pi}{\sqrt{3}a}\Big(\frac{\sqrt{3}}{2}, -\frac{1}{2}\Big)\ ,\ \boldsymbol{b}_2 = \frac{4\pi}{\sqrt{3}a}(0,1), \tag{2.5}$$

and the near-neighbor translation vectors are:

$$\boldsymbol{N} = \left\{ a\Big(0, \frac{1}{\sqrt{3}}\Big), a\Big(-\frac{1}{2}, -\frac{1}{2\sqrt{3}}\Big), a\Big(\frac{1}{2}, -\frac{1}{2\sqrt{3}}\Big) \right\}. \tag{2.6}$$

The site-diagonal matrix elements t_μ are the atomic energies of s and p orbitals, with the latter chosen as the zero of energy.

t_s	s	t_{p_x,p_x}	$n_x^2(pp\sigma) + (1 - n_x^2)(pp\pi)$
t_p	p	t_{p_y,p_y}	$n_y^2(pp\sigma) + (1 - n_y^2)(pp\pi)$
$t_{s,s}$	$(ss\sigma)$	t_{p_z,p_z}	$n_z^2(pp\sigma) + (1 - n_z^2)(pp\pi)$
t_{s,p_x}	$n_x(sp\sigma)$	t_{p_x,p_y}	$n_x n_y(pp\sigma) - n_x n_y(pp\pi)$
t_{s,p_y}	$n_y(sp\sigma)$	t_{p_x,p_z}	$n_x n_z(pp\sigma) - n_x n_z(pp\pi)$
t_{s,p_z}	$n_z(sp\sigma)$	t_{p_y,p_z}	$n_y n_z(pp\sigma) - n_y n_z(pp\pi)$

Table 2.1: Two-center matrix elements for hoping between s and p orbitals along a direction specified by the unit vector (n_x, n_y, n_z).

In Table 2.1 we reproduce for completeness the relationship between the required nearest-neighbor hopping matrix elements $t_{\mu,\mu'}$ and the four independent Slater-Koster parameters $(ss\sigma)$, $(sp\sigma)$, $(pp\sigma)$, and $(pp\pi)$ whose numerical values specify this model quantitatively. If the graphene lattice is placed in the $\hat{x}$-$\hat{y}$ plane, $n_z = 0$ for hops on the graphene lattice and the atomic p_z orbitals decouple from other orbitals. This property is more general than our model, since it follows from the graphene plane inversion symmetry that orbitals which are even and odd under this symmetry operation will not be coupled, and is key to the way in which weak spin-orbit interactions influence the low-energy bands. For the basic formulation of a tight-binding model and its application to graphene, see Appendix A.

2.2.2 Atomic spin-orbit interactions

The microscopic spin-orbit interaction is

$$H_{SO} = \frac{1}{2(m_e c)^2} (\nabla V \times \boldsymbol{p}) \cdot \boldsymbol{S}. \tag{2.7}$$

Since ∇V is largest near the atomic nuclei, spin-orbit interactions are normally accurately approximated by a local atomic contribution of the form:

$$H_{SO} = \sum_{i,l} P_{il} \; \xi_l \; \boldsymbol{L}_i \cdot \boldsymbol{S}_i, \tag{2.8}$$

where i is a site index, P_{il} denotes projection onto angular momentum l on site i, ξ_l is the atomic spin-orbit coupling constant for angular momentum l, and $\boldsymbol{S}$ is the spin operator on site i. For our model spin-orbit coupling occurs only among the p orbitals. In Table 2.2 we reproduce the $\boldsymbol{L} \cdot \boldsymbol{S}$ matrix elements for p orbitals in a $(p_x, p_y, p_z) \times (\uparrow, \downarrow)$ basis.

Orb	$p_{x,\uparrow}$	$p_{x,\downarrow}$	$p_{y,\uparrow}$	$p_{y,\downarrow}$	$p_{z,\uparrow}$	$p_{z,\downarrow}$
$p_{x,\uparrow}$	0	0	-0.5i	0	0	0.5
$p_{x,\downarrow}$	0	0	0	0.5i	-0.5	0
$p_{y,\uparrow}$	0.5i	0	0	0	0	-0.5i
$p_{y,\downarrow}$	0	-0.5i	0	0	-0.5i	0
$p_{z,\uparrow}$	0	-0.5	0	0.5i	0	0
$p_{z,\downarrow}$	0.5	0	0.5i	0	0	0

Table 2.2: Matrix elements of $\boldsymbol{L} \cdot \boldsymbol{S}$ for p orbitals.

2.2.3 External gate electric fields

Finite carrier densities have been generated in graphene by applying an external gate voltage. The resulting electric field E_{ext} lifts inversion symmetry in the graphene plane. An electric field E_{ext} can also be produced by accidental doping in the substrate or cap layer or by atomic length scale charge rearrangements near the graphene/substrate or graphene/cap-layer interfaces. To model this important effect we consider an additional local atomic single-particle Stark-effect term of the form

$$H_{EF} = eE_{ext} \sum_i z_i \tag{2.9}$$

where i is a site index. In our s-p tight-binding model the only nonvanishing matrix element of H_{EF} is the one between the s and p_z orbitals to which we assign the value $eE_{ext}z_0$, shown in Table 2.3.

Orb	s	p_x	p_y	p_z
s	0	0	0	$eE_{ext}z_0$
p_x	0	0	0	0
p_y	0	0	0	0
p_z	$eE_{ext}z_0$	0	0	0

Table 2.3: Matrix elements of $eE_{ext}z$. The only nonvanishing matrix element is the one between the s and p_z orbitals to which the value $eE_{ext}z_0$ is assigned.

2.3 Perturbation theory

2.3.1 Unperturbed Hamiltonian matrix at K and K'

The low-energy Hamiltonian is specified by the Dirac Hamiltonian and by the spin-orbit coupling terms at K and K'. We choose the inequivalent hexagonal corner wavevectors K and K' to be $K = \frac{1}{3}(2\boldsymbol{b}_1 + \boldsymbol{b}_2) = (\frac{4\pi}{3a}, 0)$ and $K' = -K$. Table 2.4 and Table 2.5 list the Hamiltonian matrix elements

Orbital	A,s	A,p_x	A,p_y	A,p_z	B,s	B,p_x	B,p_y	B,p_z
A,s	s	0	0	0	0	$\pm i\alpha$	α	0
A,p_x	0	0	0	0	$\mp i\alpha$	$-\beta$	$\mp i\beta$	0
A,p_y	0	0	0	0	$-\alpha$	$\mp i\beta$	β	0
A,p_z	0	0	0	0	0	0	0	0
B,s	0	$\pm i\alpha$	$-\alpha$	0	s	0	0	0
B,p_x	$\mp i\alpha$	$-\beta$	$\pm i\beta$	0	0	0	0	0
B,p_y	α	$\pm i\beta$	β	0	0	0	0	0
B,p_z	0	0	0	0	0	0	0	0

Table 2.4: Tight-binding model matrix elements at the K and K' points in the absence of spin-orbit interactions and external electric fields. The first (second) sign corresponds to the $K(K')$ point.

and the corresponding eigenvectors. Here s is the on-site energy of s orbitals relative to p orbitals, $\alpha \equiv \frac{3}{2}(sp\sigma)$, $\beta \equiv \frac{3}{4}\left[(pp\sigma) - (pp\pi)\right]$, and $\gamma_{\pm} = \frac{\sqrt{s^2+8\alpha^2}\pm s}{2}$. Note that the σ bands are decoupled from the π bands. When the spin-degree of freedom is included, the $E_{ext} = 0$ eigenstates at K and K' are fourfold degenerate. Below we refer to this degenerate manifold as D.

2.3.2 Low-energy effective Hamiltonian

We treat the atomic spin-orbit interaction and the external electric fields as a perturbation:

$$\Delta H = H_{SO} + H_{EF}. \tag{2.10}$$

The effective Hamiltonian which lifts the $E_{ext} = 0$ degeneracy is given by the second-order degenerate state perturbation theory expression [20]:

$$H^{(2)}_{m,n} = \sum_{l \notin D} \frac{\left\langle m^{(0)}\right| \Delta H \left|l^{(0)}\right\rangle \left\langle l^{(0)}\right| \Delta H \left|n^{(0)}\right\rangle}{E_D - E^{(0)}_l} \tag{2.11}$$

E	A, s	A, p_x	A, p_y	A, p_z	B, s	B, p_x	B, p_y	B, p_z
$-\gamma_-$	$-\gamma_-$	0	0	0	0	$\mp i\alpha$	α	0
$-\gamma_-$	0	$\mp i\alpha$	$-\alpha$	0	$-\gamma_-$	0	0	0
-2β	0	$\pm i$	-1	0	0	$\pm i$	1	0
0	0	0	0	1	0	0	0	0
0	0	0	0	0	0	0	0	1
γ_+	γ_+	0	0	0	0	$\mp i\alpha$	α	0
γ_+	0	$\mp i\alpha$	$-\alpha$	0	γ_+	0	0	0
2β	0	$\mp i$	1	0	0	$\pm i$	1	0

Table 2.5: Unnormalized unperturbed eigenvectors at the K and K' points arranged in increasing order of energies assuming $0 < \gamma_+ < 2\beta < \gamma_-$. The first (second) sign corresponds to the $K(K')$ point.

where $m, n \in D$. An elementary calculation then shows that the matrix elements of $H^{(2)}_{m,n}$ (at the K point) are those listed in Table 2.6 with λ_{SO} and λ_R defined by Eqs. (2.1) and (2.2) respectively. Similar results are obtained at the K' point given by Table 2.7.

Orb	$A, p_{z,\uparrow}$	$A, p_{z,\downarrow}$	$B, p_{z,\uparrow}$	$B, p_{z,\downarrow}$
$A, p_{z,\uparrow}$	0	0	0	0
$A, p_{z,\downarrow}$	0	$-2\lambda_{SO}$	$2i\lambda_R$	0
$B, p_{z,\uparrow}$	0	$-2i\lambda_R$	$-2\lambda_{SO}$	0
$B, p_{z,\downarrow}$	0	0	0	0

Table 2.6: The effective spin-orbit matrix at the K point.

It follows that the effective spin-orbit interaction for π orbitals is

$$H_{eff} = -\lambda_{SO} + \lambda_{SO}\,\sigma_z\tau_z s_z + \lambda_R\left(\sigma_x\tau_z s_y - \sigma_y s_x\right) \tag{2.12}$$

where the σ_α Pauli matrices act in the A, B space with σ_z eigenstates localized on a definite site, $\tau_z = \pm 1$ for K, K' points, and the s_α are Pauli matrices acting

Orb	$A, p_{z,\uparrow}$	$A, p_{z,\downarrow}$	$B, p_{z,\uparrow}$	$B, p_{z,\downarrow}$
$A, p_{z,\uparrow}$	$-2\lambda_{SO}$	0	0	$2i\lambda_R$
$A, p_{z,\downarrow}$	0	0	0	0
$B, p_{z,\uparrow}$	0	0	0	0
$B, p_{z,\downarrow}$	$-2i\lambda_R$	0	0	$-2\lambda_{SO}$

Table 2.7: The effective spin-orbit matrix at K' point.

on the electron's spin. This Hamiltonian differs from the form proposed by Kane and Mele [8] only by the constant $-\lambda_{SO}$. The excitation spectrum has a gap $E_{gap} = 2(\lambda_{SO} - \lambda_R)$ and the system has a quantized spin Hall effect [8] for $0 < \lambda_R < \lambda_{SO}$.

To obtain quantitative estimates for the coupling constants we used the tight-binding model parameters listed in Table 2.8, taken from Ref. [21]. For the spin-orbit coupling parameter among the p orbitals we use $\xi = 6$ meV, a value obtained by fitting carbon atomic energy levels given by the *ab initio* electronic structure code described below. These values imply a graphene

Parameter	Energy (eV)	Overlap
s	-8.868	1
p	0	1
$ss\sigma$	-6.769	$+0.212$
$sp\sigma$	$+5.580$	-0.102
$pp\sigma$	$+5.037$	-0.146
$pp\pi$	-3.033	$+0.129$

Table 2.8: Hopping parameters for a graphene taken from Ref. [21].

energy gap at $\lambda_R = 0$ equal to

$$2\lambda_{SO} = \frac{|s|}{9(sp\sigma)^2}\xi^2 \approx 0.00114 \text{ meV} \approx k_B \times 0.0132°\text{K}. \tag{2.13}$$

Our estimates of λ_R are discussed later.

2.4 *Ab initio* density functional theory calculations

We have performed realistic *ab initio* electronic structure calculations [22] for inversion symmetric ($\lambda_R = 0$) graphene sheets using the projector augmented wave (PAW) [23] method with a Perdew-Burke-Ernzerhof (PBE) generalized gradient approximation (GGA) [24] density functional in order to partly test the quantitative accuracy of the conclusions reached here about spin-orbit interaction gaps based on a simplified electronic structure model. The calculations were performed using VASP (Vienna *ab initio* simulation package) [25]. In VASP, spin-orbit interactions are implemented in the PAW method which is based on a transformation that maps all electron wave functions to smooth pseudo wave functions. All physical properties are evaluated using pseudo wave functions. The spin-orbit interaction is evaluated taking into account only the spherical part of the potential inside muffin tins surrounding the carbon nuclei:

$$H_{SO} = \frac{1}{2(m_e c)^2}\frac{1}{r}\frac{dV}{dr}\boldsymbol{L}\cdot\boldsymbol{S}. \tag{2.14}$$

In order to make the gaps induced by spin-orbit interaction exceed the accuracy of VASP eigenvalues, we have artificially increased the strength of H_{SO} by up to 300 times by decreasing the speed of light c. (For a brief review on DFT, see Appendix B.)

Figure 2.1 shows the tight-binding band structure of graphene for $\xi = 0$ and $\xi = 300\xi_0$, where $\xi_0 = 6$ meV. The spin-orbit gap is not large on the scale of the full band width, even when enlarged by a factor of 300.

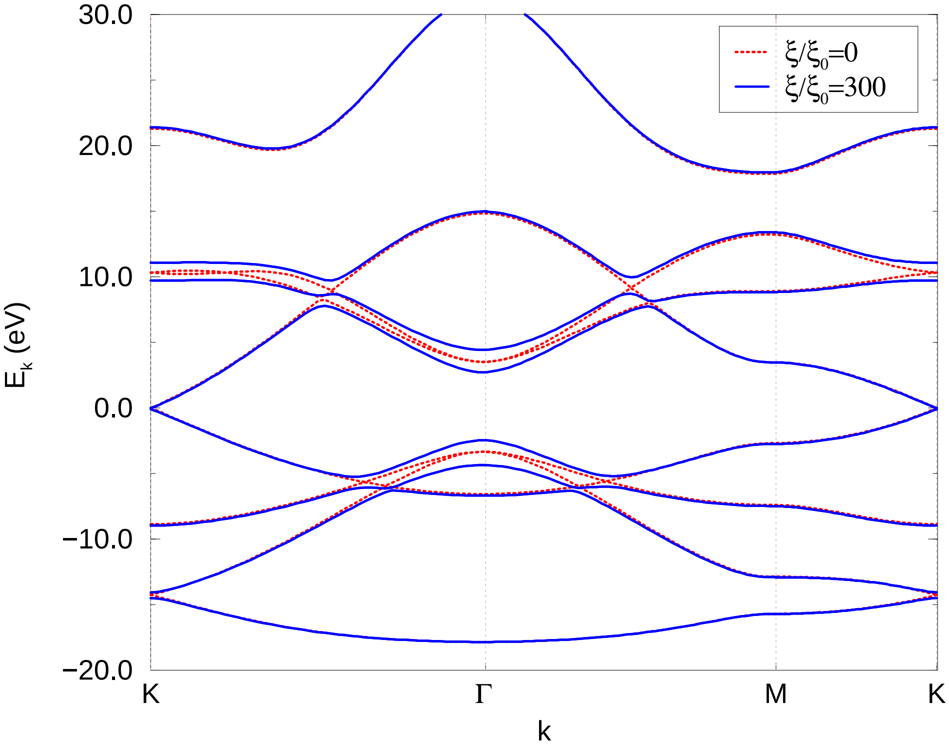

Figure 2.1: Graphene band structure for $\xi = 0$ and $\xi = 300\xi_0$ using the tight-binding model with nonorthogonal orbitals. Hopping parameters were taken from Ref. [21] and $\xi_0 = 6$ meV was used for the atomic spin-orbit coupling strength.

Figure 2.2 compares the *ab initio* calculation and tight-binding model low-energy gaps at the hexagonal Brillouin-zone corners for $\lambda_R = 0$, finding close agreement. Both approximations find a gap that grows as the second power of the spin-orbit coupling strength. The close agreement is perhaps not surprising given that VASP also makes an atomiclike approximation for the spin-orbit coupling strength. In our opinion, however, the neglected contributions from interstitial regions and from aspherical potentials inside the muffin-tin sphere are small and their contributions to energy levels tends toward even smaller values due to spatial averaging by the Bloch wave functions. We believe that these calculations demonstrate that the tight-binding model spin-orbit gap estimates are accurate.

2.5 Discussion

The intrinsic and Rashba spin-orbit interactions arise from mixing between π and σ bands due to atomic spin-orbit interactions alone in the case of λ_{SO} (Eq. (2.1)) and due to a combination of atomic spin-orbit and Stark interactions in the case of λ_R (Eq. (2.2)). These expressions for λ_{SO} and λ_R follow directly from Eq. (2.11) and from the eigenvectors and eigenenergies listed in Table 2.5. (The energetic ordering in Table 2.5 applies for $0 < \gamma_+ < 2\beta < \gamma_-$ which holds for the tight-binding parameters in Table 2.8.) The pure *p*-*p* hybridized bonding and antibonding states (energies $\pm 2\beta$ in Table 2.5) are symmetrically spaced with respect to the undoped Fermi level and do not make a net contribution to either λ_R or λ_{SO}. The *s*-*p* hybridized bonding states (energy $-\gamma_-$ in Table 2.5), on the other hand, are further from the Fermi energy

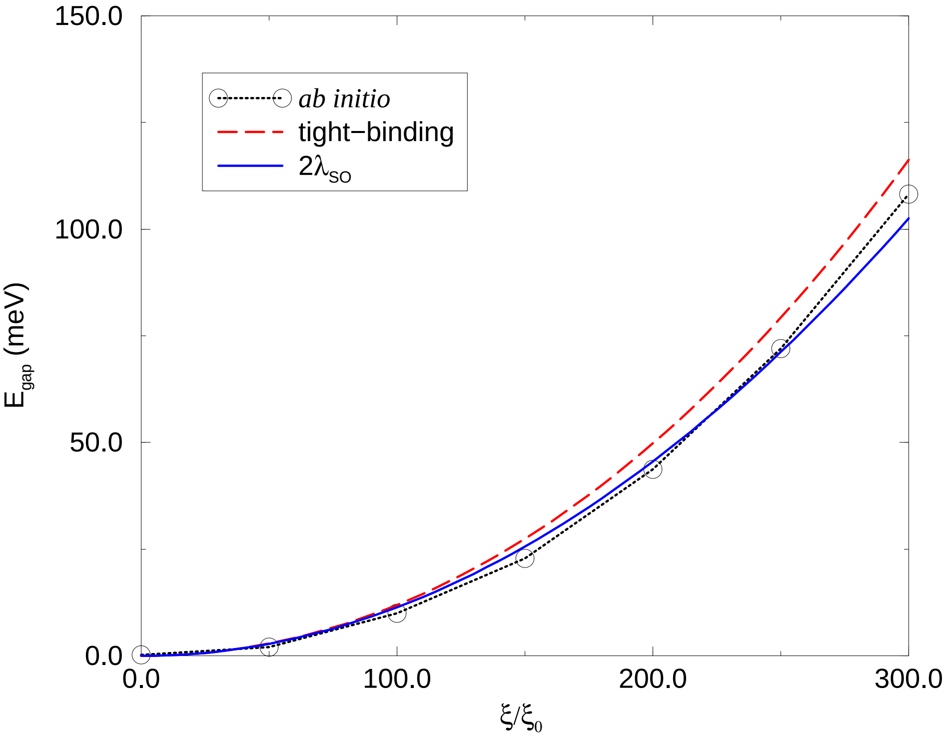

Figure 2.2: Energy gap for $\lambda_R = 0$ as a function of spin-orbit coupling strength from the *ab initio* calculation, from the tight-binding model with nonorthogonal orbitals, and from the analytic expression in Eq. (2.1).

than the corresponding antibonding states (energy $+\gamma_+$ in Table 2.5) because of the difference between atomic s and p energies. Their net contribution to λ_{SO} is proportional to s and inversely related to $sp\sigma$, which sets the scale of the energy denominators. Similar considerations explain the expression for λ_R which is proportional to ξ and $eE_{ext}z_0$ and inversely proportional to $sp\sigma$. λ_R vanishes at $E_{ext} = 0$ because of the inversion symmetry of an isolated graphene plane.

The numerical value of the Rashba interaction parameter λ_R obviously depends on the electric field perpendicular to the graphene plane which varies as the carrier density is modulated by a gate voltage. A typical value can be crudely estimated from Eq. (2.2), by assuming a typical electric field $E_{ext} \sim$ 50V/300nm [8], and using the value $z_0 \sim 3a_B \times \left(0.620\mathring{A}/0.529\mathring{A}\right)$ obtained by scaling the hydrogenic orbital Stark matrix element by the ratio of the atomic radii [26] of carbon and hydrogen:

$$\lambda_R = \frac{eE_{ext}z_0}{3(sp\sigma)}\,\xi \approx 0.0111 \text{ meV} \approx k_B \times 0.129°\text{K}. \qquad (2.15)$$

The value of λ_R is influenced by screening of the electric field at one graphene atom by the polarization of other graphene atoms and by dielectric screening in the substrate and cap layers, but these correction factors are expected to be $\sim$ 1. Note that our estimate for λ_{SO} is 100 times smaller than Kane's estimate,$\sim$ 1°K, whereas λ_R is 100 times larger than Kane's estimate, $\sim$ 0.5°mK. If our estimates are accurate, $\lambda_{SO} < \lambda_R$ at large gate voltages. For undoped samples, however, the requirement for a quantized spin Hall effect gap [8], $\lambda_{SO} > \lambda_R$, should still be achievable if accidental doping in the substrate and cap layer can be limited. When λ_{SO} is smaller than λ_R, the energy gap closes and graphene becomes a zero gap semiconductor with quadratic dispersion [8].

Our estimates suggest that the quantum spin Hall effect in graphene should occur only below $\sim$ 0.01°K, a temperature that is still accessible experimentally but not as convenient as $\sim$ 1°K. In addition, it seems likely that disorder will dominate over the spin-orbit couplings in current samples, so further progress in increasing the mobility of graphene sheets may also be necessary before the quantum spin Hall effect can be realized experimentally. We emphasize, however [13], that the spin Hall effect survives, albeit with a reduced magnitude, even when the spin-orbit gap is closed by disorder.

In summary, we have derived analytic expressions for the intrinsic and Rashba spin-orbit interaction coupling constants that appear in the low-energy Hamiltonian of a graphene sheet under a perpendicular external electric field. The Rashba interaction parameter is first order in the atomic carbon spin-orbit coupling strength ξ and the perpendicular external electric field E_{ext}, whereas the intrinsic spin-orbit interaction is second order in ξ and independent of E_{ext}. The estimated energy gap for $E_{ext} = 0$ is of the order of 0.01°K and agrees with realistic *ab initio* electronic structure calculations.

Chapter 3

Electronic Structure of Graphene Bilayers

In this chapter, we study the gate-voltage induced gap that occurs in graphene bilayers using *ab initio* density functional theory. Our calculations confirm the qualitative picture suggested by phenomenological tight-binding and continuum models. We discuss enhanced screening of the external interlayer potential at small gate voltages, which is more pronounced in the *ab initio* calculations, and quantify the role of crystalline inhomogeneity using a tight-binding model self-consistent Hartree calculation. [1]

3.1 Introduction

The band structure of an isolated graphene layer is described at low energies by a two-dimensional massless Dirac equation with linear dispersion, as discussed in the previous chapter. In bilayer graphene, the Bernal ($\tilde{A}$-B) stacking illustrated in Fig. 3.1 modifies this electronic structure in an interesting way [27–29]. At K and K', the states localized at the $\tilde{A}$ and B sites, are repelled from zero energy by interlayer tunneling; only states localized

---

[1] The contents of this chapter are based on the article: Hongki Min, Bhagawan Sahu, Sanjay K. Banerjee, and A. H. MacDonald, *Ab initio theory of gate induced gaps in graphene bilayers*, Phys. Rev. B **75**, 155115 (2007).

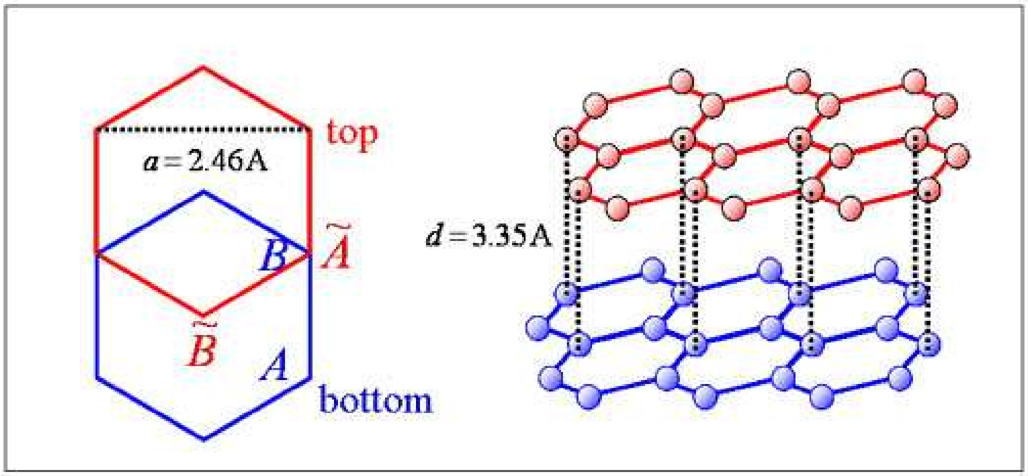

Figure 3.1: Structure of a graphene bilayer with honeycomb lattice constant $a = 2.46$ Å and interlayer separation $d = 3.35$ Å.

at A and $\tilde{B}$ are present at zero energy. When tunneling is included, the A to $\tilde{B}$ hopping is a second-order process via a virtual bonding or antibonding state at $\tilde{A}$ and B. The chirality of the low-energy bands is therefore doubled. Most intriguingly, an external potential which induces a difference between the A and $\tilde{B}$ site energies will open up a gap [30, 31] in the spectrum. Band gaps controlled by applying a gate bias have been studied experimentally using angle-resolved photoemission spectroscopy [32] and Shubnikov-de Haas analysis [33] of magnetotransport. This unique property of bilayer graphene has created considerable interest in part because it suggests the possibility of switching the conductance of a graphene bilayer channel over a wide range at a speed which is limited by gate-voltage switching, as illustrated schematically in Fig. 3.2.

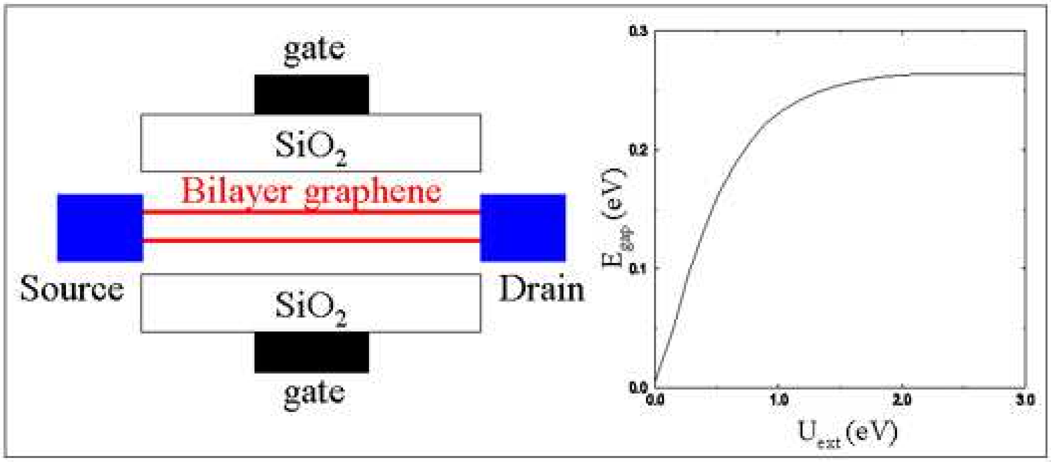

Figure 3.2: Schematic illustration of a circuit with a bilayer graphene channel sensitive to an external gate voltage. The graphene channel is separated from the front and back gates by a SiO$_2$ layer. The channel resistance change will be rapid and large when the graphene channel is undoped and isolated from the gate electrodes, as illustrated here. In this case, the total charge density in the bilayer system is fixed and the chemical potential lies in the gap opened by the gate voltage. This geometry could also be used to capacitively probe the correlation physics of the isolated bilayer system, as discussed in the text.

In this chapter, we report on an *ab initio* density functional theory (DFT) study of the influence of an external potential difference between the layers on the electronic structure of a graphene bilayer. We compare our results with the phenomenological tight-binding and continuum model Schrödinger-Poisson calculations used in previous theoretical analyses [31]. DFT predicts, in agreement with these works, that the external potential difference is strongly screened with a maximum energy gap value of ∼0.3 eV. There are, however, quantitative differences. In particular, the enhanced screening which occurs for weak external potentials is stronger in the DFT calculations. In an effort to improve the quantitative agreement, we have estimated the influence of crystalline inhomogeneity in a tight-binding model self-consistent Hartree calculation. This effect strengthens intralayer Coulomb interactions because the charge is spatially bunched, and therefore increases screening in a Hartree calculation, but does not fully account for differences between the two calculations.

3.2 *Ab initio* density functional theory calculations

We have performed *ab initio* DFT calculations [22] for an isolated graphene bilayer under a perpendicular external electric field using an all-electron linearized augmented plane wave plus local-orbital method incorporated in WIEN2K [34]. We used the generalized-gradient approximation [24] for the exchange and correlation potential. For a brief review on *ab intio* electronic structure calculations, see Appendix B.

3.2.1 External electric fields

To investigate the influence of an external electric field on a graphene bilayer, a periodic zigzag potential was applied along the z direction, perpendicular to the graphene planes, in a supercell [35]. The bilayer was placed at the center of the constant external electric field region and the size of the supercell was set to a large value ($\sim$16 Å) to minimize the interaction between bilayers in neighboring supercells. In order to resolve the small gaps produced by small external fields, we performed BZ sums using a relatively large number of **k** points (∼800) per irreducible wedge (5000 **k** points in the whole BZ). Total energies were convergent to within 0.0001 Ry.

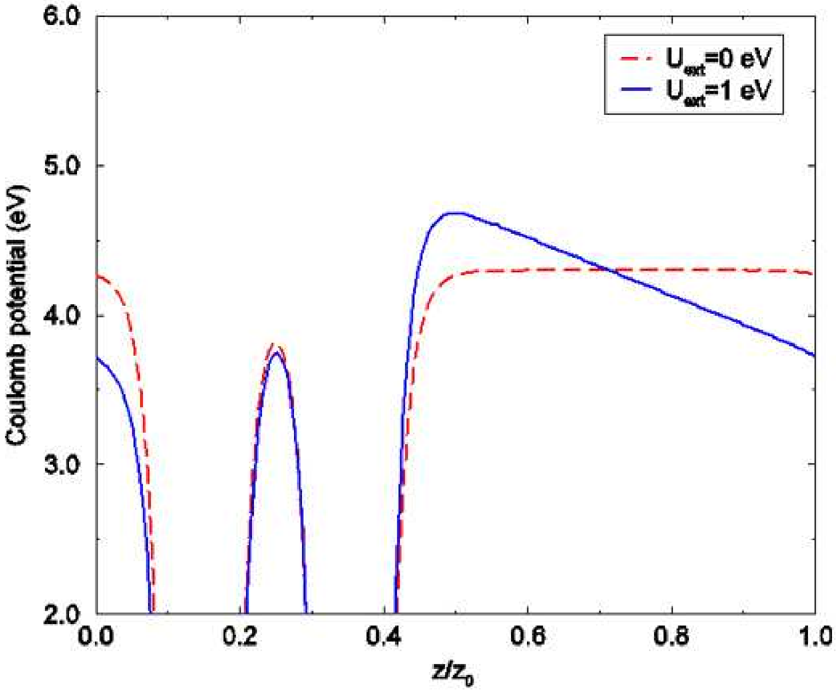

Figure 3.3: An averaged Coulomb potential of a cross section vs z for total external potential $U_{ext} = 0$ eV and $U_{ext} = 1$ eV. Here, z_0 is the superlattice period and the cross section was chosen to include equal number of atoms in each layer.

Figure 3.3 shows the Coulomb potential relative to the Fermi energy, laterally averaged along a line in the $\hat{x}$-$\hat{y}$ plane that includes an equal number of atoms in each layer, as a function of the z coordinate. The potential includes the Hartree electron-electron potential and the electron-ion interaction but not the external electric field potential or the exchange-correlation potential. The bilayer is centered around $z/z_0 = 0.25$, where z_0 is the superlattice period. (In the discussion below, we define the external potential energy U_{ext} as $U_{ext} = eE_{z,ext}d$, where $E_{z,ext}$ is an external electric field along the z direction and d is the interlayer separation of bilayer graphene which we take to be 3.35 Å.) In the absence of an electric field (dashed line), the Coulomb potential is flat in the vacuum region and the energy difference between the vacuum and the Fermi energy gives estimates of the work function of bilayer graphene to be $\sim$4.3 eV. In the presence of an electric field (solid line), charge transfer between the layers induces a potential which cancels the external potential in the vacuum region. The difference between the Coulomb energies of the two layers in the presence of an external electric field is closely related to the gate-voltage induced energy gap.

3.2.2 Energy bands

Figure 3.4 shows the DFT energy band structure of bilayer graphene in the absence of an applied external electric field. When $U_{ext} = 0$ eV, the low-energy band dispersion is nearly parabolic at two inequivalent corners, K and K', of the hexagonal BZ, as predicted by the π-orbital tight-binding and continuum model phenomenologies [30, 31]. The valence and conduction bands meet at the Fermi level.

In the absence of an external electric field, bilayer graphene, like single-layer graphene, is a zero-gap semiconductor. At finite U_{ext}, however, the low-energy bands near the K or K' point split, as explained in the Introduction.

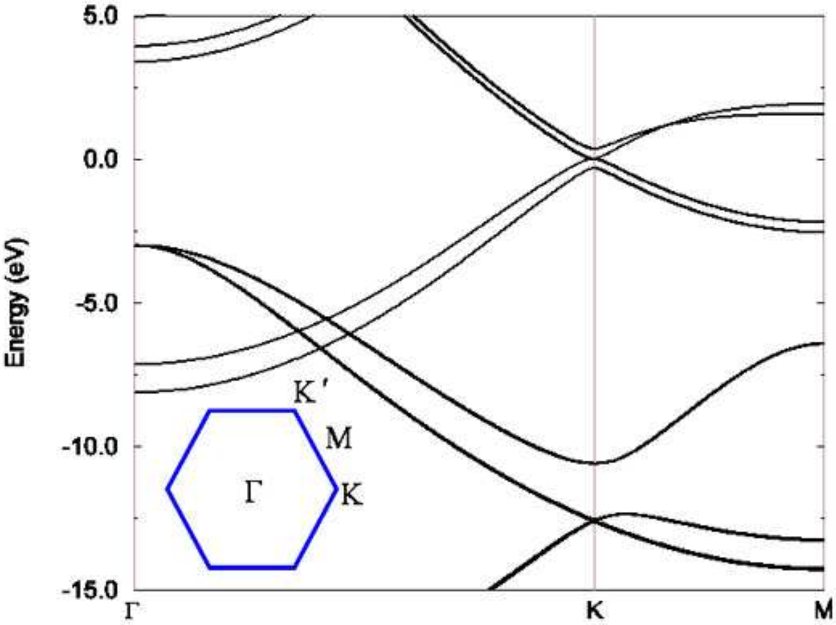

Figure 3.4: Bilayer graphene band structure in the absence of an external electric field.

Therefore, gated graphene bilayer systems are gate-voltage tunable narrow gap semiconductors [Fig. 3.5]. This property is unique, to our knowledge. It is worth noting that in the presence of an external electric field, the true energy gap does not occur at the K or K' point but slightly away from it. The low-energy spectrum develops a *Mexican hat* structure as the strength of the external electric field increases. This property is also captured by phenomenological models of graphene bilayers [31].

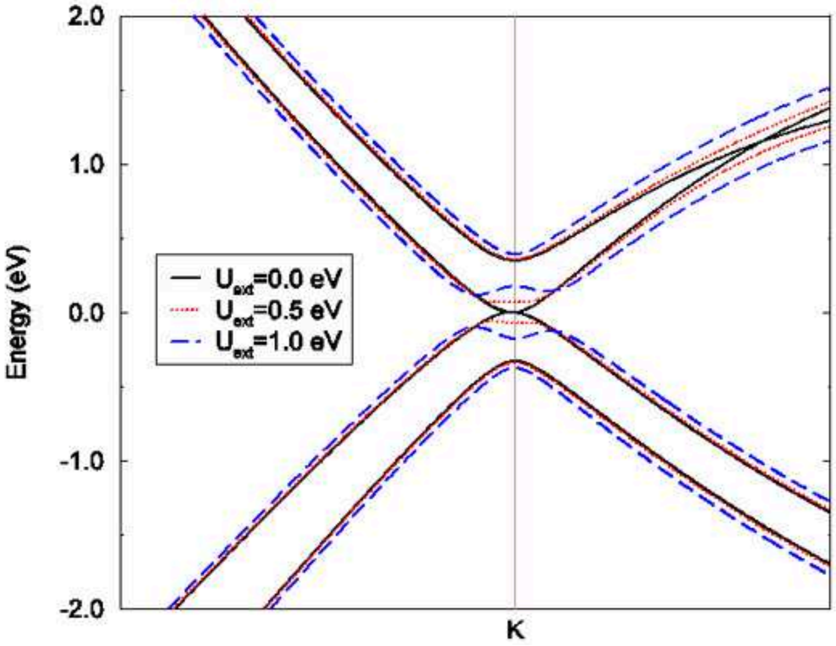

Figure 3.5: Bilayer graphene band structure near the K point for U_{ext}=0, 0.5, and 1 eV.

3.2.3 Evolution of tight-binding model parameters with U_{ext}

Figure 3.6 illustrates DFT predictions for the evolution of tight-binding parameters with the applied external potential. The tight-binding model expression for the four low-energy band eigenvalues at the K and K' points is $E_{K/K'} = \pm U/2, \pm\sqrt{\gamma_1^2 + U^2/4}$ [30], where U is the interlayer energy difference and γ_1 is the interlayer tunneling amplitude. (As we discuss below, this expression should, strictly speaking, be slightly modified in the presence of an external potential, but it still provides a convenient way of characterizing DFT predictions for the low-energy bands.) The values of U and γ_1 plotted in

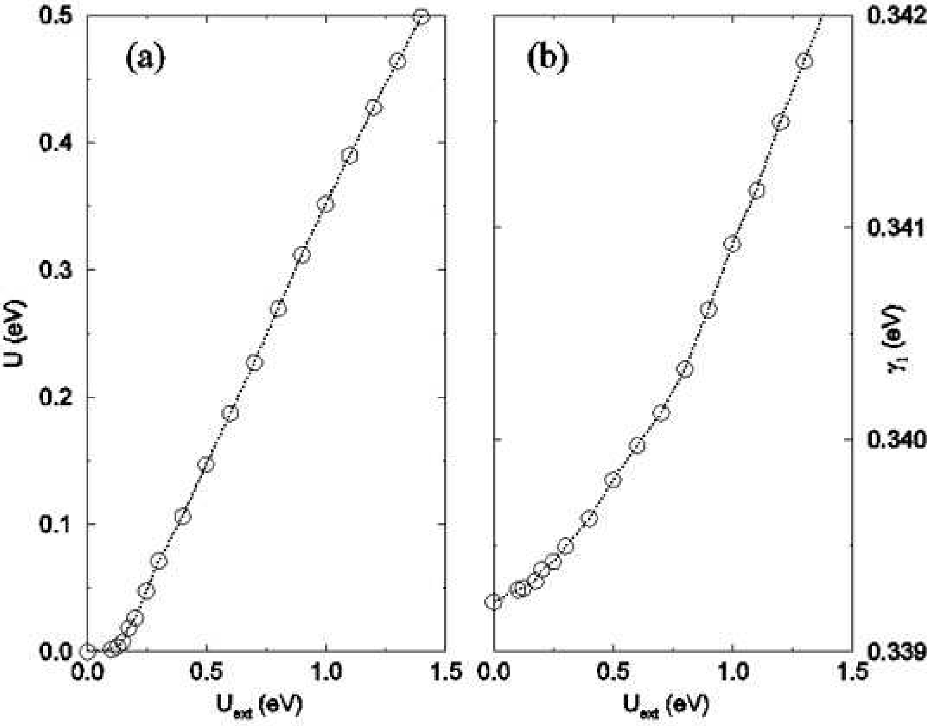

Figure 3.6: (a) Evolution of the graphene bilayer screened on-site energy difference U, extracted from the *ab initio* DFT bands as explained in the text, with the external potential U_{ext}. The external potential is strongly screened. (b) Evolution of the interlayer tunneling amplitude γ_1 with U_{ext}.

Fig. 3.6 represent this interpretation of the four lowest-energy DFT eigenvalues and clearly reflect substantial screening of the external interlayer potential by the Hartree potential plotted in Fig. 3.3. The interlayer coupling γ_1 increases monotonically as the external potential increases. The rate of increase is, however, ten times smaller than estimated in a recent experimental study [32] of a doped bilayer systems, possibly suggesting significant differences between doped and undoped systems. The intralayer nearest-neighbor π-electron hop-

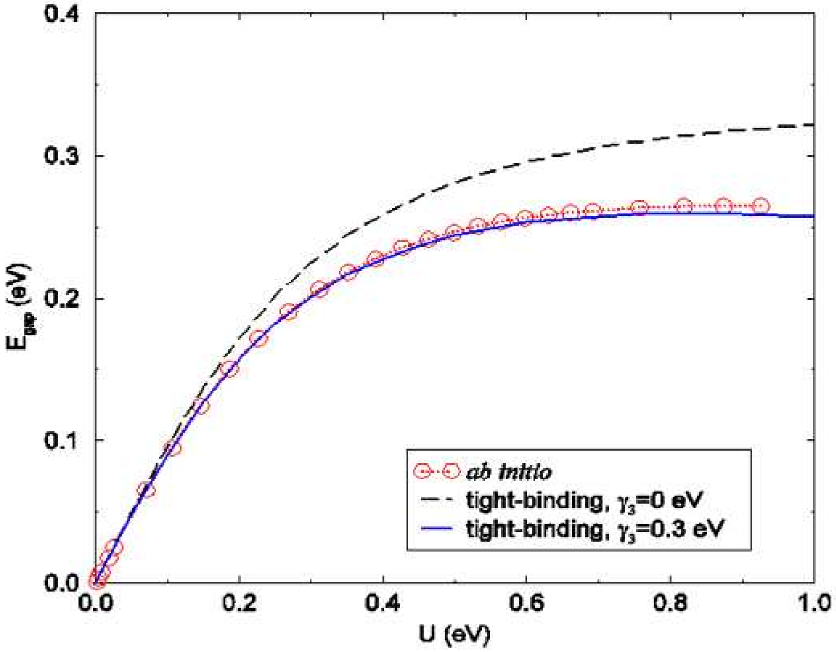

Figure 3.7: Comparison of band gap as a function of the on-site energy difference U obtained from the *ab initio* DFT calculations (open circles) with the tight-binding result for $\gamma_3 = 0$ (dashed line) and $\gamma_3 = 0.3$ eV (solid line).

ping amplitude γ_0 and the interlayer A-$\tilde{B}$ coupling γ_3 were fitted to reproduce the band dispersion around the K/K' points at low energies. We find $\gamma_0 \approx 2.6$ eV and $\gamma_3 \approx 0.3$ eV, nearly independent of the external electric field. This value for γ_0 corresponds to an in-plane velocity $v = \frac{\sqrt{3}}{2}\frac{a\gamma_0}{\hbar} \approx 8.4 \times 10^5$ m/s, where the lattice constant $a = 2.46$ Å.

Figure 3.7 compares the relationship between the on-site energy difference U extracted from the DFT calculations and the energy gap with the corresponding relationship in the tight-binding model. Note that the gap does not increase indefinitely with U but saturates at ~0.3 eV due to the *Mexican hat* structure shown in the bands illustrated in Fig. 3.4. For $\gamma_3 = 0$, we can estimate the approximate energy gap from the low-energy approximation of the tight-binding model given by $E_{gap} \approx |U|\gamma_1/\sqrt{\gamma_1^2 + U^2}$, where E_{gap} approaches $\gamma_1 \approx 0.34$ eV as U increases [31]. For $\gamma_3 \approx 0.3$ eV, however, E_{gap} is reduced from that of $\gamma_3 = 0$ and matches well with the DFT results. A nonzero value for γ_3 has a noticeable quantitative influence on the bands. This agreement confirms (unsurprisingly) that the tight-binding model captures the character of the low-energy bands in bilayer graphene. The most interesting physics is in the relationship between U and U_{ext}, which we now examine more closely.

3.3 Screening theories

3.3.1 Continuum Hartree potential models

The screening of the external potential has been examined previously for both doped and undoped bilayers using phenomenological approaches combined with the Poisson equation [31]. This type of analysis provides a good reference point for interpreting the DFT results so we start with a discussion of this picture. Consider a graphene bilayer with an interlayer separation d under an external electric field $E_{z,ext}$ along the z direction. Neglecting the finite thickness and crystalline inhomogeneity of the graphene layers, and screening external to the bilayer, the Poisson equation is

$$\boldsymbol{\nabla} \cdot \boldsymbol{E} = 4\pi(-e)\left[n_1\delta(z) + n_2\delta(z-d)\right], \tag{3.1}$$

where n_1 and n_2 are the net charge densities on the bottom and top layers, respectively. If the bilayer is placed on a gate dielectric such as silicon dioxide (SiO_2) and a voltage is applied between a gate and the bilayer, an excess charge carrier density $n = n_1 + n_2$ is supplied to the bilayer graphene and redistributed between the top and bottom layers due to an external electric field.

In order to compare with our DFT calculations, we focus here on the isolated bilayer case illustrated in Fig. 3.2, in which the total excess density $n = n_1 + n_2 = 0$. Let us define $\delta n = n_2 = -n_1$. From Eq. (3.1), we obtain the screened electric field E_z between the graphene sheets of the bilayer to be

$$E_z - E_{z,ext} = 4\pi e \delta n. \tag{3.2}$$

Adding the corresponding Hartree potential to the external potential, we obtain the screened interlayer potential difference as

$$U = U_{ext} + 4\pi e^2 d\, \delta n, \tag{3.3}$$

where $U = eE_z d$ and $U_{ext} = eE_{z,ext}d$.

To estimate the relationship between U and U_{ext}, we need only a theory for the dependence of δn on U. In the π-orbital tight-binding model, δn is given by the following integral over the BZ:

$$\delta n = \sum_{i \in occ} 2 \int_{BZ} \frac{d^2k}{(2\pi)^2} \big\langle \psi_i(\boldsymbol{k}) \big| \frac{\sigma_z}{2} \big| \psi_i(\boldsymbol{k}) \big\rangle, \tag{3.4}$$

where $|\psi_i(\boldsymbol{k})\rangle$ is a band eigenstate in the presence of U, $\sigma_z = \mathrm{diag}(1, 1, -1, -1)$ in the (top,bottom)×(A, B) basis, and the index i runs over all occupied states. The factor of 2 was included to account for spin degeneracy.

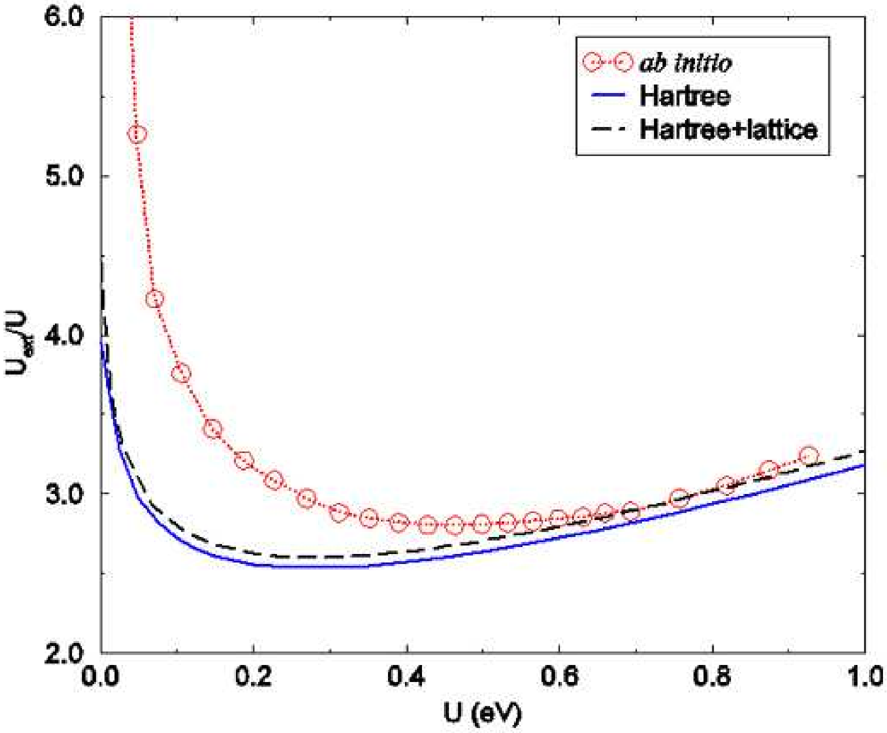

Figure 3.8: The ratio of the external electric potential U_{ext} to the interlayer energy difference inferred from the *ab initio* DFT calculation compared with the value of the same ratio in tight-binding model self-consistent Hartree calculations, both with and without crystalline inhomogeneity corrections. The tight-binding model calculations used γ_0=2.6 eV for the intralayer tunneling amplitude, γ_1=0.34 eV for the interlayer tunneling amplitude, and γ_3=0.3 eV for the interlayer A-$\tilde{B}$ coupling.

Figure 3.8 compares the screening ratio U_{ext}/U obtained from the *ab initio* DFT calculations with the screening ratio from π-orbital tight-binding model self-consistent Hartree calculations with and without corrections that account for the crystalline inhomogeneity within each layer as explained later. The agreement between the three different approaches is generally good especially at large potentials.

Note that as U approaches zero, U_{ext}/U increases in all approximations. This property reflects increased screening as the gap decreases and is explained most succinctly using the two-band continuum model [30] for the lowest-energy bands:

$$\begin{aligned} H_{eff} &\approx \frac{U}{2}\begin{pmatrix} 1 & 0 \\ 0 & -1 \end{pmatrix} - \frac{1}{2m}\begin{pmatrix} 0 & (\pi^\dagger)^2 \\ \pi^2 & 0 \end{pmatrix} \\ &= \boldsymbol{a}\cdot\boldsymbol{\sigma}, \end{aligned} \tag{3.5}$$

where $\pi = p_x + ip_y$, $m = \frac{\gamma_1}{2v^2}$, $\boldsymbol{a} = \left(-\frac{p_x^2-p_y^2}{2m}, -\frac{p_xp_y}{m}, \frac{U}{2}\right)$, and $\boldsymbol{\sigma}$ are 2×2 Pauli matrices describing the top and bottom layer low-energy sites. This Hamiltonian has simple spectra $\epsilon_\pm = \pm|\boldsymbol{a}|$ with eigenfunctions given by

$$|+\rangle = \begin{pmatrix} \cos\frac{\theta}{2}e^{-i\phi/2} \\ \sin\frac{\theta}{2}e^{i\phi/2} \end{pmatrix}, |-\rangle = \begin{pmatrix} -\sin\frac{\theta}{2}e^{-i\phi/2} \\ \cos\frac{\theta}{2}e^{i\phi/2} \end{pmatrix}, \tag{3.6}$$

where $\tan\theta = \frac{\sqrt{a_1^2+a_2^2}}{a_3}$ and $\tan\phi = \frac{a_2}{a_1}$. (For the two-component formalism, see Appendix D.) It follows that

$$\begin{aligned} \delta n &= 4\int_{|p|<p_c}\frac{d^2p}{(2\pi\hbar)^2}\langle -,\boldsymbol{p}|\frac{\sigma_z}{2}|-,\boldsymbol{p}\rangle \\ &= -\frac{1}{\pi\hbar^2}\int_0^{p_c} pdp\cos\theta(\boldsymbol{p}) \\ &= -\frac{mU}{2\pi\hbar^2}\ln\left[x_c + \sqrt{x_c^2+1}\right], \end{aligned} \tag{3.7}$$

where $x_c = \frac{p_c^2}{mU}$. We have inserted a factor of 4 in this continuum model calculation to account for both spin (↑ and ↓) and valley (K and K') degeneracies. The integral over wavevector was cut off at the radius $p_c \sim \sqrt{2m\gamma_1}$ beyond which the continuum model fails.

Inserting Eq. (3.7) in Eq. (3.3), we obtain

$$\begin{aligned} \frac{U_{ext}}{U} &= 1 - 4\pi e^2 d \, \frac{\delta n}{U} \\ &= 1 + 2\left(\frac{d}{a_B}\right)\left(\frac{m}{m_e}\right)\ln\left[x_c + \sqrt{x_c^2+1}\right], \end{aligned} \tag{3.8}$$

where $a_B = \hbar^2/m_e e^2$ is the Bohr radius and m_e is the bare electron mass. For small U, x_c is large and this simplifies to

$$\frac{U_{ext}}{U} \approx 2\left(\frac{d}{a_B}\right)\left(\frac{m}{m_e}\right)\ln\left[\frac{2p_c^2}{mU}\right]. \tag{3.9}$$

A related observation concerning the logarithmic divergence of the screening ratio at small gate voltages was made previously by McCann [31]. All three of our calculations exhibit this increased screening at weak external potentials, with the largest upturn in the *ab initio* calculations.

3.3.2 Lattice Hartree potential models

We now turn our attention to one important contribution to discrepancies between the *ab initio* DFT results and the predictions of self-consistent Hartree models similar to those described above, the role of crystalline inhomogeneity in bilayer and single-layer graphene electrostatics. We consider a general two-body interaction term $\hat{V}$,

$$\hat{V} = \frac{1}{2} \sum_{\lambda_1',\lambda_2',\lambda_1,\lambda_2} \langle \lambda_1'\lambda_2' | \, V \, | \lambda_1 \lambda_2 \rangle \, c^\dagger_{\lambda_1'} c^\dagger_{\lambda_2'} c_{\lambda_2} c_{\lambda_1}, \tag{3.10}$$

where $c^\dagger_\lambda$ and c_λ are creation and annihilation operators for a state λ. To capture the main consequences of crystalline inhomogeneity, we assume that the π-orbital Bloch states with crystal momentum $\boldsymbol{k}$ can be written as a linear combination of atomic orbitals,

$$\psi_{\boldsymbol{k},\lambda}(\boldsymbol{x}) = \frac{1}{\sqrt{N}} \sum_{\boldsymbol{R}} e^{i\boldsymbol{k}\cdot\boldsymbol{R}} \phi_\lambda(\boldsymbol{x} - \boldsymbol{R} - \boldsymbol{\tau}_\lambda) \tag{3.11}$$

where ϕ_λ is an atomiclike π orbital, $\boldsymbol{R}$ is a lattice vector, $\boldsymbol{\tau}_\lambda$ is the displacement of the sites in a unit cell with respect to the lattice vector, and N is the number of lattice sites. If we assume that the overlap of ϕ_λ-orbitals centered on different sites can be neglected and ignore the $\hat{z}$ direction spread of the graphene sheets, the interaction Hamiltonian simplifies to

$$\hat{V} = \frac{1}{2\Omega} \sum_{\boldsymbol{k}_1,\boldsymbol{k}_2,\boldsymbol{q}} \sum_{\lambda_1,\lambda_2} \tilde{V}_{\lambda_1,\lambda_2}(\boldsymbol{q}) \; c^\dagger_{\boldsymbol{k}_1+\boldsymbol{q},\lambda_1} c^\dagger_{\boldsymbol{k}_2-\boldsymbol{q},\lambda_2} c_{\boldsymbol{k}_2,\lambda_2} c_{\boldsymbol{k}_1,\lambda_1}, \tag{3.12}$$

where Ω is the area of the two-dimensional plane,

$$\tilde{V}_{\lambda_1,\lambda_2}(\boldsymbol{q}) = V_{\lambda_1,\lambda_2}(\boldsymbol{q}) \; w_{\lambda_1}(-\boldsymbol{q}) w_{\lambda_2}(\boldsymbol{q}) \; e^{i\boldsymbol{q}\cdot(\boldsymbol{\tau}_{\lambda_1} - \boldsymbol{\tau}_{\lambda_2})}, \tag{3.13}$$

$$V_{\lambda_1,\lambda_2}(\boldsymbol{q}) = \int d\boldsymbol{x} \; e^{-i\boldsymbol{q}\cdot\boldsymbol{x}} \; V_{\lambda_1,\lambda_2}(\boldsymbol{x}), \tag{3.14}$$

and

$$w_\lambda(\boldsymbol{q}) = \int d\boldsymbol{x} \; e^{-i\boldsymbol{q}\cdot\boldsymbol{x}} \; |\phi_\lambda(\boldsymbol{x})|^2 \, . \tag{3.15}$$

For the detailed description, see Appendix C.

Note that the labels $\boldsymbol{k}_1$ and $\boldsymbol{k}_2$ are restricted to the BZ, while $\boldsymbol{q}$ runs over the two-dimensional plane. In Eq. (3.14), $V_{\lambda_1,\lambda_2}(\boldsymbol{x}) = e^2/|\boldsymbol{x}|$ when λ_1 and λ_2 refer to sites in the same layer and $V_{\lambda_1,\lambda_2}(\boldsymbol{x}) = e^2/\sqrt{|\boldsymbol{x}|^2 + d^2}$ when λ_1 and λ_2 refer to layers separated by d. It follows that $V_{\lambda_1,\lambda_2}(\boldsymbol{q}) = 2\pi e^2/|\boldsymbol{q}|$ for labels in the same layer and $V_{\lambda_1,\lambda_2}(\boldsymbol{q}) = 2\pi e^2 \exp(-|\boldsymbol{q}|d)/|\boldsymbol{q}|$ for labels in different layers. Since the total charge of the bilayer is fixed in our calculations, only the differences between the various $\tilde{V}_{\lambda_1,\lambda_2}(\boldsymbol{q})$ values are relevant. For explicit calculations, we have used a Gaussian form factor $w_\lambda(\boldsymbol{q}) = e^{-|\boldsymbol{q}|^2 r_0^2/2}$ corresponding to $|\phi_\lambda(\boldsymbol{x})|^2 \propto e^{-|\boldsymbol{x}|^2/2r_0^2}$, where $r_0 \sim 0.48$ Å was obtained by fitting to the DFT valence orbitals.

This two-body Hamiltonian can be used to account for crystalline inhomogeneity in a graphene bilayer system with arbitrary electronic correlations. To compare with the *ab initio* DFT calculations, we consider interactions in a mean-field Hartree approximation in which the interaction contribution to the single-particle Hamiltonian is

$$\hat{V}^{(H)} = \sum_{\boldsymbol{k},a,\sigma} \epsilon_{a\sigma}^{(H)} c_{\boldsymbol{k},a\sigma}^{\dagger} c_{\boldsymbol{k},a\sigma} \tag{3.16}$$

where a and σ denote layer and sublattice degrees of freedom. Here,

$$\epsilon_{a\sigma}^{(H)} = \sum_{a',\sigma'} \tilde{V}_{a\sigma,a'\sigma'} n_{a'\sigma'}, \tag{3.17}$$

where $n_{a\sigma} = \frac{2}{\Omega} \sum_{\boldsymbol{k}} \left\langle c_{\boldsymbol{k},a\sigma}^{\dagger} c_{\boldsymbol{k},a\sigma} \right\rangle$ including spin degeneracy and

$$\tilde{V}_{a\sigma,a'\sigma'} = \sum_{\boldsymbol{G}} \tilde{V}_{a\sigma,a'\sigma'}(\boldsymbol{G}), \tag{3.18}$$

with $\boldsymbol{G}$ a triangular lattice reciprocal-lattice vector.

As explained in the Introduction, interlayer tunneling in graphene leads to high-energy bands which favor the $\tilde{A}$-B sites and low-energy bands that favor the A-$\tilde{B}$ sites. Since the low-energy bands respond most strongly to the external potential, we can expect that the charge transfer occurs more strongly on the A-$\tilde{B}$ sites, and that the screening potential should be larger on these sites. Instead of a single-interlayer Hartree screening potential, two Hartree potentials for low and high bands must be calculated separately:

$$\begin{aligned} \epsilon_l^{(H)} &= \epsilon_{\tilde{B}}^{(H)} - \epsilon_A^{(H)}, \\ \epsilon_h^{(H)} &= \epsilon_{\tilde{A}}^{(H)} - \epsilon_B^{(H)}. \end{aligned} \tag{3.19}$$

When only the $\boldsymbol{G} = 0$ term is retained in the reciprocal-lattice vector sum,

$$\epsilon_l^{(H0)} = \epsilon_h^{(H0)} = 2\pi e^2 d\,(n_{\tilde{A}} + n_{\tilde{B}} - n_A - n_B), \tag{3.20}$$

and Eq. (3.3) is recovered. It turns out that the sum over reciprocal-lattice vectors can be truncated with good accuracy at the first shell. Noting that $e^{-|\boldsymbol{G}|d} \ll 1$, we find for the crystalline inhomogeneity corrections

$$\begin{aligned} \epsilon_l^{(H1)} &\approx 2\pi e^2 d\,\alpha(\boldsymbol{G})(6\Delta n_l - 3\Delta n_h), \\ \epsilon_h^{(H1)} &\approx 2\pi e^2 d\,\alpha(\boldsymbol{G})(6\Delta n_h - 3\Delta n_l), \end{aligned} \tag{3.21}$$

where $\Delta n_l = n_{\tilde{B}} - n_A$, $\Delta n_h = n_{\tilde{A}} - n_B$, and $\alpha(\boldsymbol{G}) = e^{-|\boldsymbol{G}|^2 r_0^2}/|\boldsymbol{G}|d \approx 0.0136$. Thus, the inhomogeneity effect results in more screening as expected, but as indicated by the black dashed line in Fig. 3.8, it is not able to account for the largest part of the discrepancy between DFT and model results.

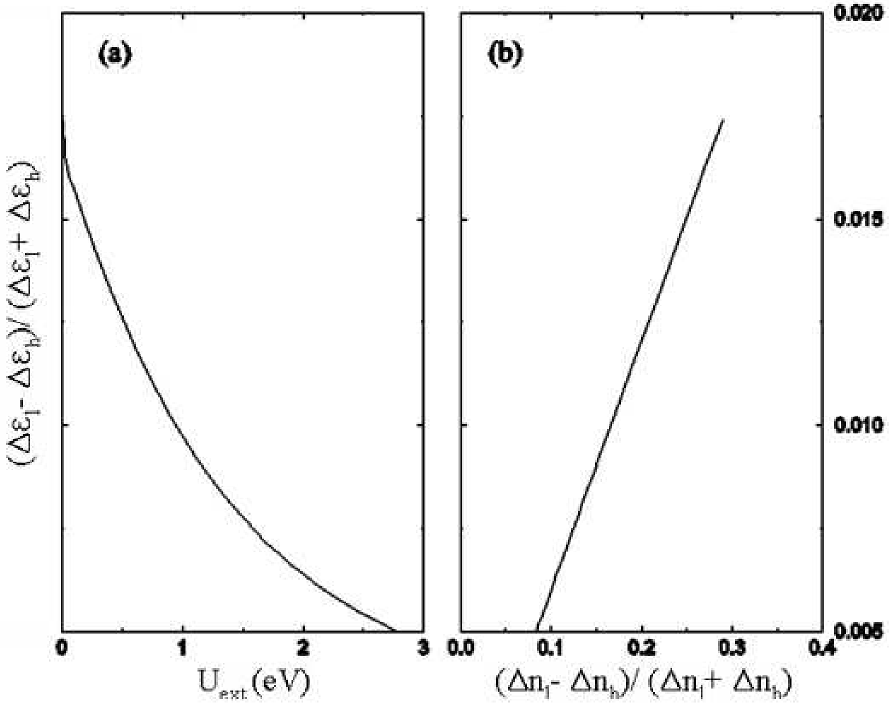

Figure 3.9: Splitting of Hartree potentials $\big(\epsilon_l^{(H)} - \epsilon_h^{(H)}\big)/\big(\epsilon_l^{(H)} + \epsilon_h^{(H)}\big)$ as a function of (a) the external electric potential U_{ext} and (b) the corresponding density inhomogeneity $\big(\Delta n_l - \Delta n_h\big)/\big(\Delta n_l + \Delta n_h\big)$ in the lattice Hartree potential model.

As the external electric potential is decreased, the difference between low-energy and high-energy site occupancies is increased. The difference in Hartree potentials rises correspondingly, as illustrated in Fig. 3.9(a). From Eq. (3.21), we can estimate the relation between the splitting of the Hartree potentials and the density inhomogeneity:

$$\frac{\epsilon_l^{(H)} - \epsilon_h^{(H)}}{\epsilon_l^{(H)} + \epsilon_h^{(H)}} \approx \frac{9}{2}\alpha(\boldsymbol{G})\frac{\Delta n_l - \Delta n_h}{\Delta n_l + \Delta n_h}, \tag{3.22}$$

where the coefficient $\frac{9}{2}\alpha(\boldsymbol{G})$ is given by $\sim$0.0612 [Fig. 3.9(b)].

3.4 Discussion

Our DFT calculations of external potential induced gaps in the electronic structure of graphene bilayers confirm the simple picture provided by phenomenological tight-binding models. The *ab initio* calculations include a number of effects not contained in the model calculations. For example, the occupied σ orbitals within each graphene plane, which are neglected in the π-orbital tight-binding model, will be slightly polarized by the external electric field and contribute to screening. In the DFT calculations, not only Hartree potentials but also exchange-correlation potentials will be altered by an external electric field and influence the screening process. Since the exchange potential is attractive, its contribution to the total potential will lower energies in a layer more as the density is increased. The exchange potential therefore makes a negative contribution to the screening ratio. The quantitative discrepancies between the DFT and phenomenological model reflect the combination of these and other additional effects contained in the DFT calculations, and strong sensitivity to intralayer and interlayer tunneling amplitudes which may not be evaluated with perfect accuracy by DFT. We also note that the low-energy eigenstates in bilayer graphene are coherent combinations of amplitudes on both layers, which implies that interlayer exchange interactions will be substantial. This kind of effect is absent in the exchange-correlation potentials commonly used in DFT. Indeed, it is entirely possible that DFT calculations do not predict accurate values for the screening ratio. We believe that there is strong motivation for capacitive studies of the interlayer screening properties of graphene bilayers using an experimental arrangement similar to that in Fig. 3.2.

In summary, we have used *ab initio* density functional theory calculations to study the gate-voltage tunable gap in the electronic structure of bilayer graphene. The electric-field dependence of the on-site energy difference and the interlayer tunneling amplitude were extracted from the DFT calculation results by fitting to tight-binding model expressions for high-symmetry point graphene bilayer band eigenvalues. The screening effect seen in the DFT calculations can be explained by a tight-binding model self-consistent Hartree method including crystalline inhomogeneity corrections, although the DFT screening is stronger especially for weak external potentials.

Chapter 4

Electronic Structure of Graphene Multilayers

So far, we studied electronic structure of graphene monolayers and bilayers. In this chapter, we study the electronic structure of multilayer graphene using a π-orbital continuum model with nearest-neighbor intralayer and interlayer tunneling. Using degenerate state perturbation theory, we show that the low-energy electronic structure of arbitrarily stacked graphene multilayers consists of chiral pseudospin doublets with a conserved chirality sum. [1]

4.1 Introduction

In this chapter, we study the electronic structure of arbitrarily stacked multilayer graphene using a π-orbital continuum model with only near-neighbor interactions, analyzing its low-energy spectrum using degenerate state perturbation theory. Here we focus solely on aligned multilayer graphene without rotational stacking faults [36]. Interestingly, we find that the low-energy effective theory of multilayer graphene is always described by a set of chiral

---

[1] The contents of this chapter are based on the articles: Hongki Min and A. H. MacDonald, *Chiral decomposition in the electronic structure of graphene multilayers*, Phys. Rev. B **77**, 155416 (2008); Hongki Min and A. H. MacDonald, *Electronic structure of multilayer graphene*, proceedings of YKIS2007 (arXiv:0806.2792).

pseudospin doublets with a conserved chirality sum. We discuss implications of this finding for the quantum Hall effect in multilayer graphene.

4.2 π-orbital continuum model

We consider the π-orbital continuum model for N-layer graphene Hamiltonian which describes bands near the hexagonal corners of the triangular lattice Brillouin zone, the K and K' points:

$$\mathcal{H} = \sum_{\boldsymbol{p}} \Psi_{\boldsymbol{p}}^{\dagger} H(\boldsymbol{p}) \Psi_{\boldsymbol{p}} \tag{4.1}$$

where $\Psi_{\boldsymbol{p}} = (c_{1,\alpha,\boldsymbol{p}}, c_{1,\beta,\boldsymbol{p}}, \cdots, c_{N,\alpha,\boldsymbol{p}}, c_{N,\beta,\boldsymbol{p}})$ and $c_{l,\mu,\boldsymbol{p}}$ is an electron annihilation operator for layer $l = 1, \cdots, N$, sublattice $\mu = \alpha, \beta$ and momentum $\boldsymbol{p}$ measured from K or K' point.

The simplest model for a multilayer graphene system allows only nearest-neighbor intralayer hopping t and the nearest-neighbor interlayer hopping $t_{\perp}$. The in-plane Fermi velocity v is related with t by $\frac{\hbar v}{a} = \frac{\sqrt{3}}{2} t$, where $a = 2.46$ Å is a lattice constant of monolayer graphene. Although this model is not fully realistic, some aspects of the electronic structure can be understood by fully analyzing the properties of this simplified model first and then considering corrections.

4.2.1 Stacking diagrams

When one graphene layer is placed on another, it is energetically favorable [37] for the atoms of either α or β sublattices to be displaced along

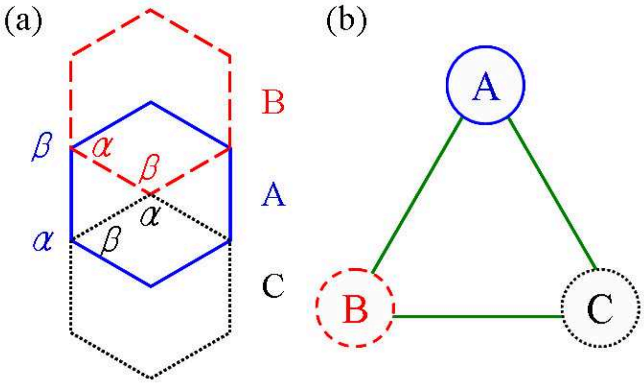

Figure 4.1: (a) Energetically favored stacking arrangements for graphene sheets. The honeycomb lattice of a single sheet has two triangular sublattices, labeled by α and β. Given a starting graphene sheet, the honeycomb lattice for the next layer is usually positioned by displacing either α or β sublattice carbon atoms along a honeycomb edge. There are therefore in three distinct two-dimensional (2D) sheets, labeled by A, B, and C. Representative α and β sublattice positions in A, B, and C layers are identified in this illustration. It is also possible to transform between layer types by rotating by $\pm 60°$ about a carbon atom on one of the two sublattices. (b) Each added layer cycles around this stacking triangle in either the right-handed or the left-handed sense. Reversals of the sense of this rotation tend to increase the number of low-energy pseudospin doublets N_D. In graphite, Bernal (AB) stacking corresponds to a reversal at every step and orthorhombic (ABC) stacking corresponds to no reversals.

the honeycomb edges, as illustrated in Fig. 4.1. This stacking rule implies the three distinct but equivalent projections (labeled A, B, and C) of the three-dimensional structure's honeycomb-lattice layers onto the $\hat{x}$-$\hat{y}$ plane and 2^{N-2} distinct N-layer stack sequences. When a B layer is placed on an A layer, a C layer on a B layer, or an A layer on a C layer, the α sites of the upper layer are above the β sites of the lower layer and therefore linked by the nearest interlayer neighbor π-orbital hopping amplitude $t_\perp$. For the corresponding anticyclic stacking choices (A on B, B on C, or C on A), it is the β sites of the upper layer and the α sites of the lower layer that are linked. All distinct $N = 3$, $N = 4$, and $N = 5$ layer stacks are illustrated in Fig. 4.2, in which we have arbitrarily labeled the first two layers starting from the bottom as A and B.

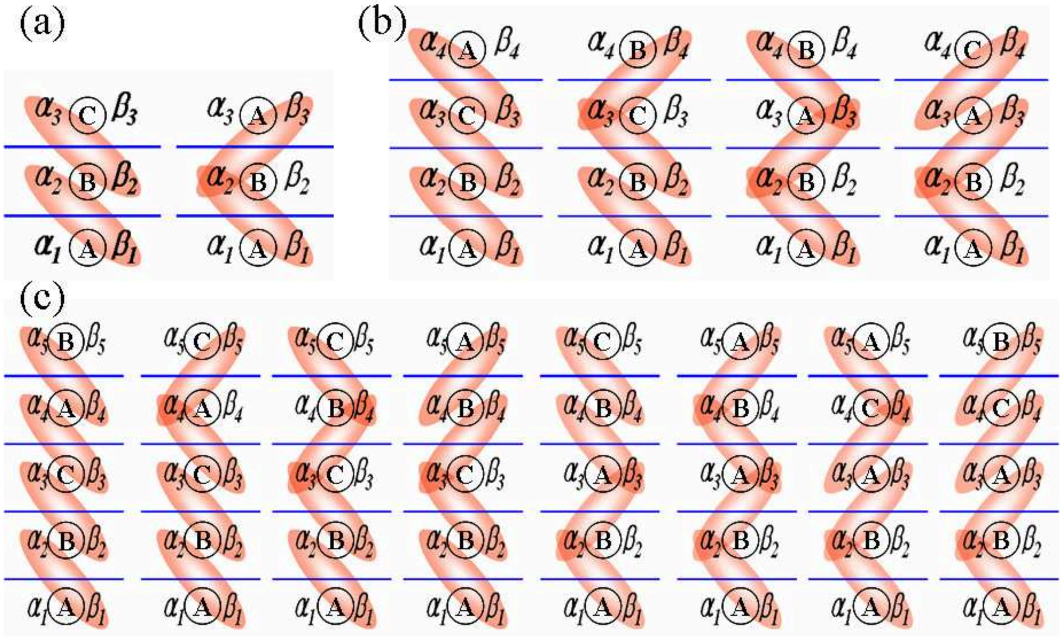

Figure 4.2: Stacking sequences and linkage diagrams for $N = 3, 4, 5$ layer stacks. The low-energy band and Landau level structures of a graphene stacks with nearest-neighbor hopping are readily read off these diagrams as explained in the text. Shaded ovals link α and β nearest interlayer neighbors.

4.2.2 Energy band structure

Before analyzing energy spectrum of multilayer graphene, let's consider the Hamiltonian of a one-band tight-binding model for a chain of length N with near-neighbor hopping parameter $t_\perp$:

$$H = \left(\begin{array}{ccccc} 0 & t_\perp & 0 & 0 & \\ t_\perp & 0 & t_\perp & 0 & \\ 0 & t_\perp & 0 & t_\perp & \cdots \\ 0 & 0 & t_\perp & 0 & \\ & & \cdots & & \end{array} \right). \tag{4.2}$$

This Hamiltonian is important for analyzing the role of interlayer hopping as we explain below.

Let $\boldsymbol{a} = (a_1, ..., a_N)$ be an eigenvector with an eigenvalue ε. Then the eigenvalue problem reduces to the following difference equation

$$\varepsilon a_n = t_\perp (a_{n-1} + a_{n+1}), \tag{4.3}$$

with the boundary condition $a_0 = a_{N+1} = 0$. Assuming $a_n \sim e^{in\theta}$, it can be shown that [38]

$$\begin{aligned} \varepsilon_r &= 2\, t_\perp \cos\theta_r, \qquad (4.4) \\ \boldsymbol{a}_r &= \sqrt{\frac{2}{N+1}} (\sin\theta_r, \sin 2\theta_r, \cdots, \sin M\theta_r), \end{aligned}$$

where $r = 1, 2, \ldots, N$ is the chain eigenvalue index and $\theta_r = r\pi/(N+1)$. Note that odd N chains have a zero-energy eigenstate with an eigenvector that has nonzero amplitudes, constant in magnitude and alternating in sign, on the sublattice of the chain ends.

Next, let's consider AA stacking. Although AA stacking is not energetically favorable, it is still interesting to consider this arrangement for pedagogical purposes. In the case of AA stacking, the Hamiltonian at K is given by

$$H_{\mathrm{AA}}(\boldsymbol{p}) = \left(\begin{array}{cccccccc} 0 & v\pi^\dagger & t_\perp & 0 & 0 & 0 & & \\ v\pi & 0 & 0 & t_\perp & 0 & 0 & & \\ t_\perp & 0 & 0 & v\pi^\dagger & t_\perp & 0 & & \\ 0 & t_\perp & v\pi & 0 & 0 & t_\perp & \cdots & \\ 0 & 0 & t_\perp & 0 & 0 & v\pi^\dagger & & \\ 0 & 0 & 0 & t_\perp & v\pi & 0 & & \\ & & & \cdots & & & & \end{array} \right), \tag{4.5}$$

where $\pi = p_x + ip_y$.

As we now explain, the electronic structure of AA stacked N-layer graphene can be thought of as consisting of separate 1D chains for each wavevector in the 2D triangular lattice Brillouin zone of a single graphene layer. For an eigenvector $(a_1, b_1, \cdots, a_N, b_N)$ with an eigenvalue ε and fixed 2D momentum, the difference equations in this case are

$$\begin{aligned} \varepsilon a_n &= t_\perp(a_{n-1} + a_{n+1}) + v\pi^\dagger b_n, \qquad (4.6) \\ \varepsilon b_n &= t_\perp(b_{n-1} + b_{n+1}) + v\pi a_n, \end{aligned}$$

with the boundary condition $a_0 = a_{N+1} = b_0 = b_{N+1} = 0$.

Let $c_n = a_n + b_n e^{-i\phi}$ and $d_n = a_n - b_n e^{-i\phi}$ where $\phi = \tan^{-1}(p_y/p_x)$, then

$$\begin{aligned} (\varepsilon - v|\boldsymbol{p}|)c_n &= t_\perp(c_{n-1} + c_{n+1}), \qquad (4.7) \\ (\varepsilon + v|\boldsymbol{p}|)d_n &= t_\perp(d_{n-1} + d_{n+1}), \end{aligned}$$

with the same boundary condition $c_0 = c_{N+1} = d_0 = d_{N+1} = 0$. Thus the energy spectrum is given by

$$\varepsilon^{\pm}_{r,\boldsymbol{p}} = \pm v|\boldsymbol{p}| + 2t_{\perp} \cos\left(\frac{r\pi}{N+1}\right), \tag{4.8}$$

where $r = 1, 2, \cdots, N$. Note that for odd N, the $r = (N+1)/2$ mode provides two zero-energy states at $\boldsymbol{p} = 0$.

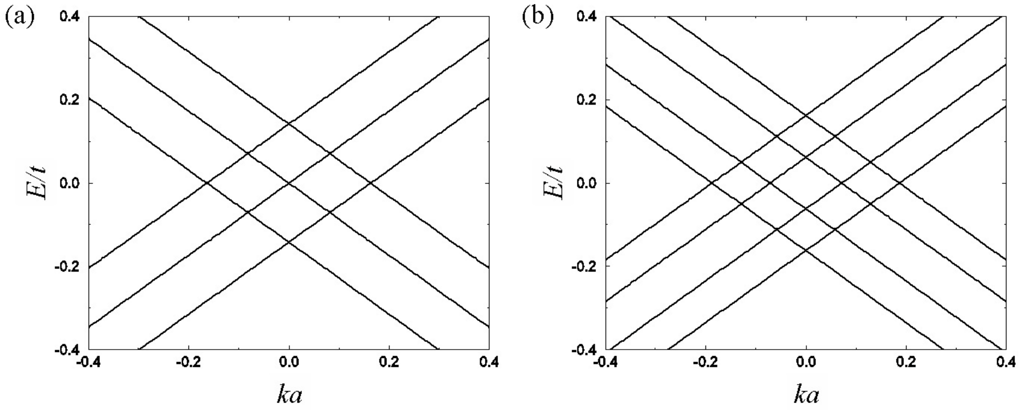

Figure 4.3: Band structure near the K point for (a) trilayer and (b) tetralayer graphene with AA stacking for nearest intralayer neighbor hopping $t = 3$ eV and nearest interlayer neighbor hopping $t_{\perp} = 0.1t$.

Figure 4.3 shows the band structure of AA stacked trilayer and tetralayer graphene near the K point. Because of the hybridization between α-α and β-β sublattices in each layer, zero-energy states occur at momenta that are remote from the K and K' points. In the following we turn our attention to stacks in which adjacent graphene layers have a relative rotation of 60 degrees. As we show, in this case the zero-energy states always occur precisely at the Brillouin-zone corners.

In the case of AB stacking, the Hamiltonian at K has the following form,

$$H_{\mathrm{AB}}(\boldsymbol{p}) = \begin{pmatrix} 0 & v\pi^\dagger & 0 & 0 & 0 & 0 & \\ v\pi & 0 & t_\perp & 0 & 0 & 0 & \\ 0 & t_\perp & 0 & v\pi^\dagger & 0 & t_\perp & \\ 0 & 0 & v\pi & 0 & 0 & 0 & \cdots \\ 0 & 0 & 0 & 0 & 0 & v\pi^\dagger & \\ 0 & 0 & t_\perp & 0 & v\pi & 0 & \\ & & & \cdots & & & \end{pmatrix}. \tag{4.9}$$

We will see that the subtle difference in the Hamiltonian compared to the AA case changes the electronic structure in a qualitative way. To obtain the energy spectrum of AB stacked N-layer graphene, let's consider corresponding difference equations [39]:

$$\begin{aligned} \varepsilon a_{2n-1} &= (v\pi^\dagger)b_{2n-1}, \qquad (4.10)\\ \varepsilon b_{2n-1} &= t_\perp(a_{2n-2} + a_{2n}) + (v\pi)a_{2n-1}, \\ \varepsilon a_{2n} &= t_\perp(b_{2n-1} + b_{2n+1}) + (v\pi^\dagger)b_{2n}, \\ \varepsilon b_{2n} &= (v\pi)a_{2n}, \end{aligned}$$

with the boundary condition $a_0 = a_{N+1} = b_0 = b_{N+1} = 0$.

Let $c_{2n-1} = b_{2n-1}$ and $c_{2n} = a_{2n}$, then the difference equations reduce to

$$(\varepsilon - v^2|\boldsymbol{p}|^2/\varepsilon)c_n = t_\perp(c_{n-1} + c_{n+1}), \tag{4.11}$$

with the boundary condition $c_0 = c_{N+1} = 0$. Then the energy spectrum is given by

$$\varepsilon - v^2|\boldsymbol{p}|^2/\varepsilon = 2t_\perp \cos\left(\frac{r\pi}{N+1}\right), \tag{4.12}$$

where $r = 1, 2, \cdots, N$. Thus

$$\varepsilon^{\pm}_{r,\boldsymbol{p}} = t_{\perp} \cos\left(\frac{r\pi}{N+1}\right) \pm \sqrt{v^2|\boldsymbol{p}|^2 + t_{\perp}^2 \cos^2\left(\frac{r\pi}{N+1}\right)}. \tag{4.13}$$

Note that relativistic energy spectrum for a particle with the momentum $\boldsymbol{p}$ and mass m is given by

$$\varepsilon_{\boldsymbol{p}} = \sqrt{|\boldsymbol{p}|^2 c^2 + m^2 c^4}. \tag{4.14}$$

Thus we can identify $m_r v^2 = \left|t_{\perp} \cos\left(\frac{r\pi}{N+1}\right)\right|$ as the effective mass for mode r.

For a massive mode with mass m_r, the low-energy spectrum is given by

$$\varepsilon_{r,\boldsymbol{p}} \approx \begin{cases} +\frac{\boldsymbol{p}^2}{2m_r} & \text{if } t_{\perp} \cos\left(\frac{r\pi}{N+1}\right) < 0, \\ -\frac{\boldsymbol{p}^2}{2m_r} & \text{if } t_{\perp} \cos\left(\frac{r\pi}{N+1}\right) > 0. \end{cases} \tag{4.15}$$

For odd N, the mode with $r = (N+1)/2$ is massless and its energy is given by

$$\varepsilon^{\pm}_{\boldsymbol{p}} \approx \pm v|\boldsymbol{p}|. \tag{4.16}$$

For even N, all N modes are massive at low energies. Therefore, the low-energy spectrum with odd number of layers is a combination of one massless Dirac mode and $N-1$ massive Dirac modes, whereas the low-energy spectrum with even number of layers is composed of only massive Dirac modes.

Figure 4.4 shows the band structure of AB stacked trilayer and tetralayer graphene near the K point. As discussed earlier, the trilayer has one massless mode and two massive modes, while the tetralayer has all massive modes at low energies. Note that at $\boldsymbol{p} = 0$, each massless mode gives two zero energies

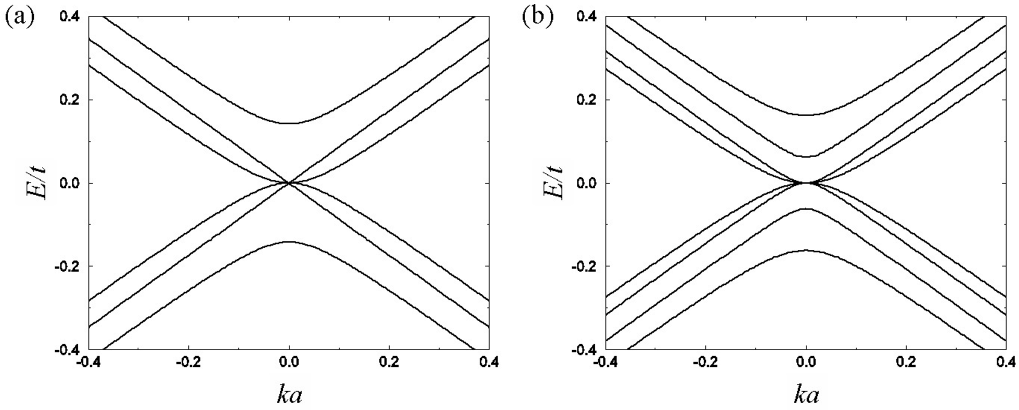

Figure 4.4: Band structure near the K point for (a) trilayer and (b) tetralayer graphene with AB stacking for nearest intralayer neighbor hopping $t = 3$ eV and nearest interlayer neighbor hopping $t_\perp = 0.1t$.

while each massive mode gives one zero energy. Therefore, for odd N, there are $2 + (N - 1) = N + 1$ zero-energy states while for even N, there are N zero-energy states.

In the case of ABC stacking, the Hamiltonian at K is given by

$$H_{\mathrm{ABC}}(\boldsymbol{p}) = \begin{pmatrix} 0 & v\pi^\dagger & 0 & 0 & 0 & 0 & \\ v\pi & 0 & t_\perp & 0 & 0 & 0 & \\ 0 & t_\perp & 0 & v\pi^\dagger & 0 & 0 & \\ 0 & 0 & v\pi & 0 & t_\perp & 0 & \cdots \\ 0 & 0 & 0 & t_\perp & 0 & v\pi^\dagger & \\ 0 & 0 & 0 & 0 & v\pi & 0 & \\ & & & \cdots & & & \end{pmatrix}. \tag{4.17}$$

Unfortunately for ABC stacking, there do not exist low-order difference equations with a simple boundary condition. Instead we can easily derive a low-energy effective Hamiltonian. Surprisingly, it turns out that ABC stacked N-layer graphene is described by N-chiral 2D electron system. (More detailed discussion for the effective theory of arbitrarily stacked graphene will be presented in Sec. 4.3.)

It is important to recognize that in ABC stacking, there is vertical hopping between all the lower layer β sites and all the upper layer α sites. For $\pi = 0$ each α-β pair forms a symmetric-antisymmetric doublet with energies $\pm t_\perp$, leaving the bottom α_1 and top β_N sites as the only low-energy states. This behavior is readily understood from the stacking diagrams, in Fig. 4.2. It is possible to construct a 2 × 2 π-dependent low-energy effective Hamiltonian for the low-energy part of the spectrum using perturbation theory. The same procedure can then be extended to arbitrary stacking sequences.

The simplest example is bilayer graphene [30]. Low and high energy subspaces are identified by finding the spectrum at $\pi = 0$ and identifying all the zero-energy eigenstates. The intralayer tunneling term, which is proportional to π, couples low and high energy states. Using degenerate state perturbation theory, the effective Hamiltonian in the low energy space is given to leading (2nd) order in π by

$$H_2^{eff}(\boldsymbol{p}) = -\left(\begin{array}{cc} 0 & \frac{(\pi^\dagger)^2}{2m} \\ \frac{(\pi)^2}{2m} & 0 \end{array} \right) = -t_\perp \left(\begin{array}{cc} 0 & (\nu^\dagger)^2 \\ (\nu)^2 & 0 \end{array} \right), \tag{4.18}$$

where we have used a (α_1, β_2) basis, $m = t_\perp / 2v^2$ and $\nu = v\pi / t_\perp$. In the same way we find that the effective Hamiltonian of ABC stacked N-layer graphene is given by

$$H_N^{eff}(\boldsymbol{p}) = -t_\perp \left(\begin{array}{cc} 0 & (\nu^\dagger)^N \\ (\nu)^N & 0 \end{array} \right), \tag{4.19}$$

using a (α_1, β_N) basis. The leading correction appears at order N in π because the unperturbed high-energy states are localized on a (β_i, α_{i+1}) pair and the perturbation is intralayer tunneling. Note that we have for mathematical convenience chosen a gauge in which the single-layer Hamiltonian is

$$H_1^{eff}(\boldsymbol{p}) = -\begin{pmatrix} 0 & v\pi^\dagger \\ v\pi & 0 \end{pmatrix}. \tag{4.20}$$

We can prove Eq. (4.19) by the mathematical induction method. Imagine that we add one more layer on top of N-layer graphene with ABC stacking. Then the combined Hamiltonian is given by

$$H_{N+1}^{eff}(\boldsymbol{p}) = -t_\perp \begin{pmatrix} 0 & (\nu^\dagger)^N & 0 & 0 \\ (\nu)^N & 0 & -1 & 0 \\ 0 & -1 & 0 & \nu^\dagger \\ 0 & 0 & \nu & 0 \end{pmatrix}, \tag{4.21}$$

using a $(\alpha_1, \beta_N, \alpha_{N+1}, \beta_{N+1})$ basis.

Let P be a low-energy subspace spanned by (α_1, β_{N+1}) and Q be a high-energy subspace spanned by (α_{N+1}, β_N). Note that the effective Hamiltonian can be derived using the degenerate state perturbation theory [40],

$$H_{eff} \approx H_{PP} - H_{PQ}\frac{1}{H_{QQ}}H_{QP}. \tag{4.22}$$

Here the projected Hamiltonian matrices to P and Q subspace are given by

$$H_{QQ}(\boldsymbol{p}) = t_\perp \begin{pmatrix} 0 & 1 \\ 1 & 0 \end{pmatrix}, \; H_{PQ}(\boldsymbol{p}) = -t_\perp \begin{pmatrix} 0 & (\nu^\dagger)^N \\ \nu & 0 \end{pmatrix}, \tag{4.23}$$

and $H_{PP}(\boldsymbol{p}) = 0$. Thus we can easily show that,

$$H_{N+1}^{eff}(\boldsymbol{p}) \approx -t_\perp \begin{pmatrix} 0 & (\nu^\dagger)^{N+1} \\ (\nu)^{N+1} & 0 \end{pmatrix}, \tag{4.24}$$

which proves Eq. (4.19). The corresponding energy spectrum in Eq. (4.19) is given by

$$\varepsilon^{\pm}_{eff,\boldsymbol{p}} = \pm t_{\perp} \left(\frac{v|\boldsymbol{p}|}{t_{\perp}} \right)^{N} . \tag{4.25}$$

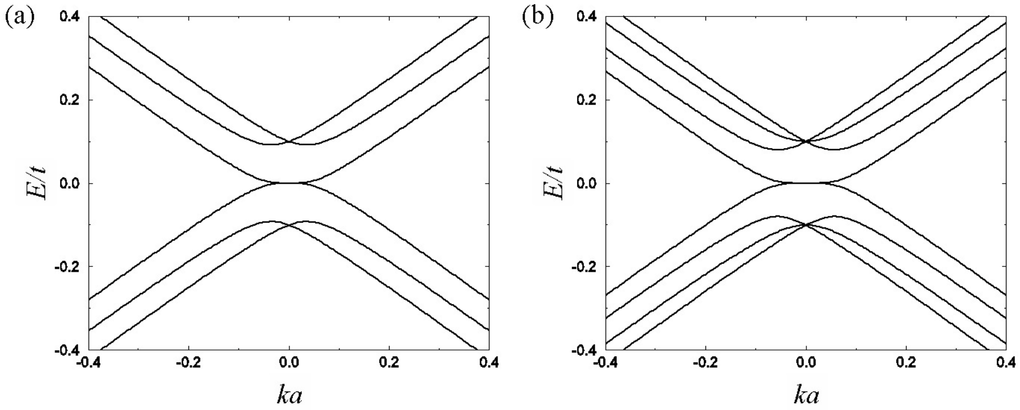

Figure 4.5: Band structure near the K point for (a) trilayer and (b) tetralayer graphene with ABC stacking for nearest intralayer neighbor hopping $t = 3$ eV and nearest interlayer neighbor hopping $t_{\perp} = 0.1t$.

Figure 4.5 shows the band structure of ABC stacked trilayer and tetralayer graphene near the K point. Note that at $\boldsymbol{p} = 0$, there are only two zero energy states no matter how thick the stack is.

So far, we have considered periodic stacking sequences such as AA, AB and ABC stackings. It is easy to generalize the previous discussion to construct the Hamiltonian for an arbitrarily stacked multilayer graphene system. Figure 4.6 shows the band structure of ABCB stacked tetralayer graphene and ABBC stacked tetralayer graphene near the K point. For the ABCB stacked tetralayer graphene, the low-energy spectrum looks like a superposition of a

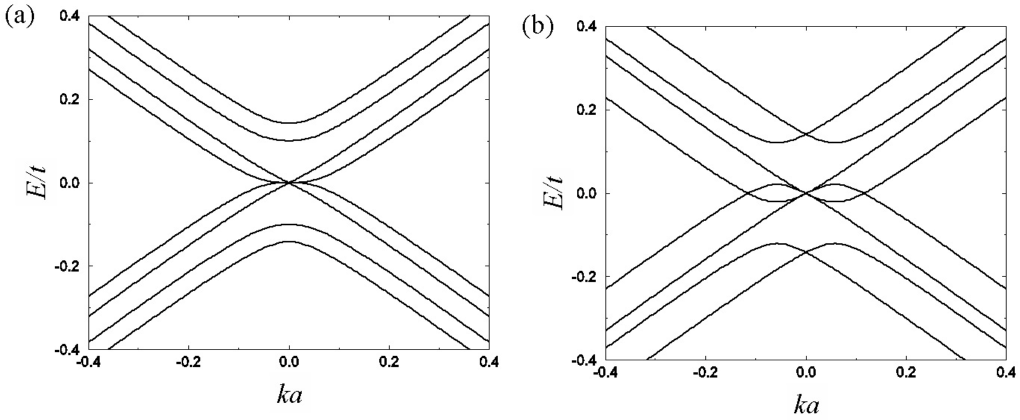

Figure 4.6: Band structure near the K point for tetralayer graphene with (a) ABCB stacking and (b) ABBC stacking for nearest intralayer neighbor hopping $t = 3$ eV and nearest interlayer neighbor hopping $t_{\perp} = 0.1t$.

linear dispersion and a cubic one. For the ABBA stacked tetralayer graphene, zero energies appear not only at the Dirac point but also away from it. A more detailed low-energy spectrum analysis will be presented in Sec. 4.3.

4.2.3 Landau level spectrum

In the presence of a magnetic field $\boldsymbol{B} = B\hat{z}$, a Hamiltonian is modified by $\boldsymbol{p} \to \boldsymbol{p} + \frac{e}{c}\boldsymbol{A}$, where $\boldsymbol{A}$ is the vector potential with $\boldsymbol{B} = \nabla \times \boldsymbol{A}$. The quantum Hamiltonian is most easily diagonalized by introducing raising and lowering operators, $a = l\pi^{\dagger}/\sqrt{2}\hbar$ and $a^{\dagger} = l\pi/\sqrt{2}\hbar$ substitution, where $l = \sqrt{\hbar c/e|B|}$, and noting that $[a, a^{\dagger}] = 1$. We can then expand the wavefunction amplitude on each sublattice of each layer in terms of parabolic band Landau level states $|n\rangle$ which are eigenstates of the $a^{\dagger}a$. For many Hamiltonians, including those studied here, the Hamiltonian can be block diagonalized by fixing the parabolic band Landau-level offset between different sublattices and between different layers. This procedure is familiar from theories of Landau-level structure in other multiband $\boldsymbol{k} \cdot \boldsymbol{p}$ theories.

In the case of AA stacking, let's choose the n-th Landau level basis at K as $(\alpha_{1,n-1}, \beta_{1,n}, \cdots, \alpha_{N,n-1}, \beta_{N,n})$. Then Eq. (4.5) reduces to

$$H_{\mathrm{AA}}(n) = \begin{pmatrix} 0 & \varepsilon_n & t_\perp & 0 & 0 & 0 & \\ \varepsilon_n & 0 & 0 & t_\perp & 0 & 0 & \\ t_\perp & 0 & 0 & \varepsilon_n & t_\perp & 0 & \\ 0 & t_\perp & \varepsilon_n & 0 & 0 & t_\perp & \cdots \\ 0 & 0 & t_\perp & 0 & 0 & \varepsilon_n & \\ 0 & 0 & 0 & t_\perp & \varepsilon_n & 0 & \\ & & & \cdots & & & \end{pmatrix}, \tag{4.26}$$

where $\varepsilon_n = \sqrt{2n}\hbar v/l$. Note that 2D Landau level states with a negative index do not exist so the corresponding basis states and matrix elements are understood as being absent in the matrix block. Thus $H_{\mathrm{AA}}(n=0)$ is a $N \times N$ matrix, while $H_{\mathrm{AA}}(n>0)$ is a $2N \times 2N$ matrix.

By diagonalizing Eq. (4.26) using the difference equation method, we can obtain the exact Landau level spectrum. For $n > 0$, Landau levels are given by

$$\varepsilon_{r,n}^{\pm} = \pm\varepsilon_n + 2t_\perp \cos\left(\frac{r\pi}{N+1}\right), \tag{4.27}$$

where $r = 1, 2, \cdots, N$. Note that for $n = 0$, Landau levels are given by $\varepsilon_{r,0} = 2t_\perp \cos\left(\frac{r\pi}{N+1}\right)$. Thus for odd N, there exists one (B-independent) zero-energy Landau level at $r = (N+1)/2$.

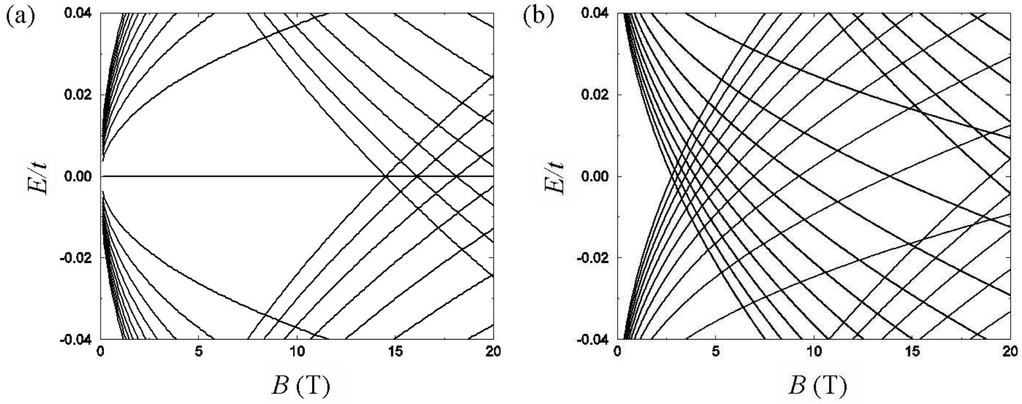

Figure 4.7: Landau levels of (a) trilayer and (b) tetralayer graphene with AA stacking for nearest intralayer neighbor hopping $t = 3$ eV and nearest interlayer neighbor hopping $t_\perp = 0.1t$. Landau levels were shown up to $n = 10$.

Figure 4.7 shows the Landau levels of AA stacked trilayer and tetralayer graphene as a function of magnetic fields. For the trilayer, there is one zero-energy Landau level, while for the tetralayer, there is no zero-energy Landau level. Note that there are Landau levels crossing the zero-energy line in AA stacking.

In the case of AB stacking, a proper choice of the n-th Landau level basis at K is $(\alpha_{1,n-1}, \beta_{1,n}, \alpha_{2,n}, \beta_{2,n+1}, \alpha_{3,n-1}, \beta_{3,n}, \alpha_{4,n}, \beta_{4,n+1}, \cdots)$ such that all the interlayer hopping terms are contained in the n-th Landau level Hamiltonian.

Then Eq. (4.9) reduces to

$$H_{\mathrm{AB}}(n) = \begin{pmatrix} 0 & \varepsilon_n & 0 & 0 & 0 & 0 & \\ \varepsilon_n & 0 & t_\perp & 0 & 0 & 0 & \\ 0 & t_\perp & 0 & \varepsilon_{n+1} & 0 & t_\perp & \\ 0 & 0 & \varepsilon_{n+1} & 0 & 0 & 0 & \cdots \\ 0 & 0 & 0 & 0 & 0 & \varepsilon_n & \\ 0 & 0 & t_\perp & 0 & \varepsilon_n & 0 & \\ & & & \cdots & & & \end{pmatrix}, \tag{4.28}$$

where $\varepsilon_n = \sqrt{2n}\hbar v/l$. As discussed earlier, special care should be given for states with a negative index.

For the Hamiltonian in Eq. (4.28), there do not exist corresponding difference equations with a proper boundary condition, thus cannot be diagonalized analytically. From Eq. (4.15), however, we can find the low-energy Landau levels for massive mode with mass m_r as

$$\varepsilon_{r,n} \approx \begin{cases} +\hbar\omega_r\sqrt{n(n+1)} & \text{if } t_\perp \cos\left(\frac{r\pi}{N+1}\right) < 0, \\ -\hbar\omega_r\sqrt{n(n+1)} & \text{if } t_\perp \cos\left(\frac{r\pi}{N+1}\right) > 0, \end{cases} \tag{4.29}$$

where $\omega_r = e|B|/m_r c$ and $r = 1, 2, \cdots, N$, which is proportional to B. These equations apply at small B, just as the $B = 0$ limiting low-energy dispersions applied at small momentum π. For the massless mode, from Eq. (4.16) Landau levels are given by

$$\varepsilon_n^\pm = \pm\varepsilon_n, \tag{4.30}$$

which is proportional to $B^{1/2}$.

Figure 4.8 shows the Landau levels of AB stacked trilayer and tetralayer graphene as a function of magnetic fields. Note that the linear B dependence expected for massive modes applies over a more limited field range when the

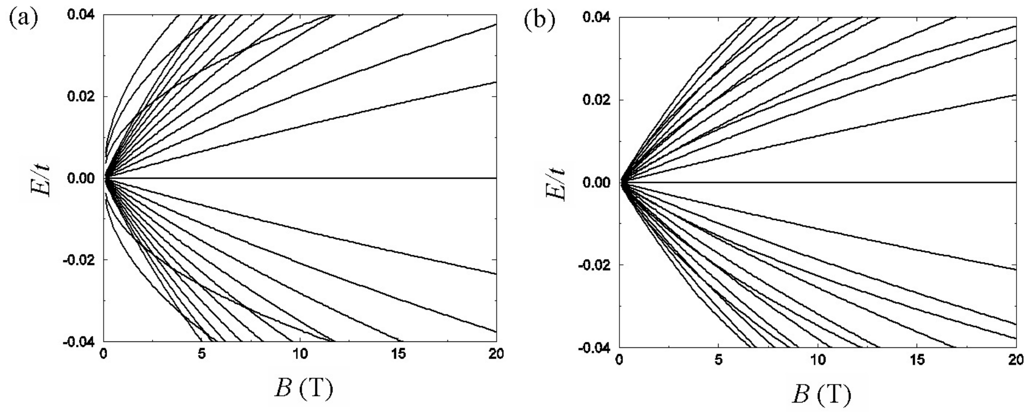

Figure 4.8: Landau levels of (a) trilayer and (b) tetralayer graphene with AB stacking for nearest intralayer neighbor hopping $t = 3$ eV and nearest interlayer neighbor hopping $t_\perp = 0.1t$. Landau levels up to $n = 10$ are shown.

mass is small. For the trilayer, Landau levels are composed of massless Dirac spectra ($\propto B^{1/2}$) and massive Dirac spectra ($\propto B$), while for the tetralayer, Landau levels are all massive Dirac spectra. This is consistent with the band structure analysis shown in Fig. 4.4.

Note that the massive modes in Eq. (4.29) have two zero-energy Landau levels for $n = -1$ and 0, whereas the massless mode in Eq. (4.30) has one for $n = 0$. There are therefore N zero-energy Landau levels in both even and odd N AB stacks. This property can also be understood directly from the Hamiltonian in Eq. (4.28), by eliminating negative n basis states and rearranging rows to block diagonalize the matrix.

In the case of ABC stacking, a proper choice of the n-th Landau level basis at K is $(\alpha_{1,n-1}, \beta_{1,n}, \alpha_{2,n}, \beta_{2,n+1}, \alpha_{3,n+1}, \beta_{3,n+2}, \cdots)$ such that all the interlayer hopping terms are contained in the n-th Landau level Hamiltonian. Then Eq. (4.17) reduces to

$$H_{\mathrm{ABC}}(n) = \begin{pmatrix} 0 & \varepsilon_n & 0 & 0 & 0 & 0 & \\ \varepsilon_n & 0 & t_\perp & 0 & 0 & 0 & \\ 0 & t_\perp & 0 & \varepsilon_{n+1} & 0 & 0 & \\ 0 & 0 & \varepsilon_{n+1} & 0 & t_\perp & 0 & \cdots \\ 0 & 0 & 0 & t_\perp & 0 & \varepsilon_{n+2} & \\ 0 & 0 & 0 & 0 & \varepsilon_{n+2} & 0 & \\ & & & \cdots & & & \end{pmatrix}, \qquad (4.31)$$

where $\varepsilon_n = \sqrt{2n}\hbar v/l$.

The low-energy spectrum can be obtained from the effective Hamiltonian in Eq. (4.17). For $n > 0$, Landau levels are given by

$$\varepsilon_n^{\pm} = \pm\hbar\omega_N\sqrt{n(n+1)\cdots(n+N-1)}, \qquad (4.32)$$

where $\hbar\omega_N = t_\perp(\sqrt{2}\hbar v/t_\perp l)^N \propto B^{N/2}$, while for $n = -N+1, -N+2, \cdots, 0$ they are zero. Note that there are N zero-energy Landau levels for ABC stacked N-layer graphene.

Figure 4.9 shows the Landau levels of ABC stacked trilayer and tetralayer graphene as a function of magnetic fields. For the trilayer, Landau levels are proportional to $B^{3/2}$, while for the tetralayer, Landau levels are proportional to B^2.

It is straightforward to generalize the previous discussion to construct the Hamiltonian in Landau level basis for an arbitrarily stacked multilayer graphene system. As discussed earlier, special care should be given for states with a negative index. Figure 4.10 shows Landau levels of ABCB stacked

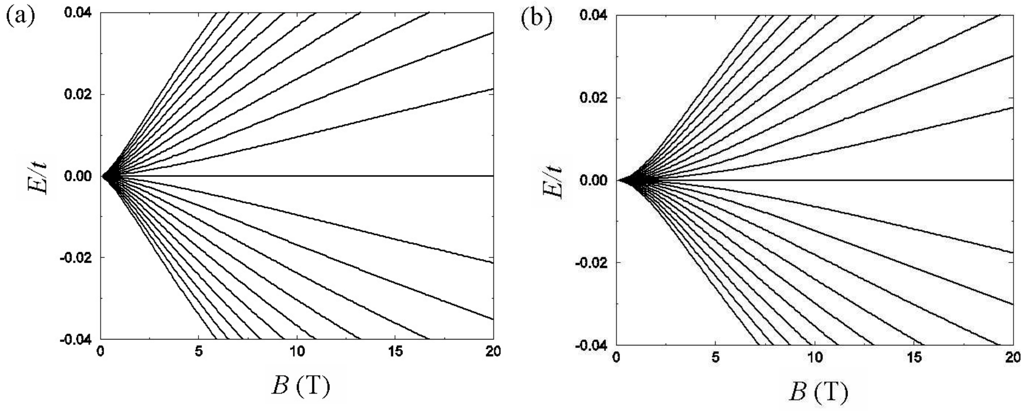

Figure 4.9: Landau levels of (a) trilayer and (b) tetralayer graphene with ABC stacking for nearest intralayer neighbor hopping $t = 3$ eV and nearest interlayer neighbor hopping $t_\perp = 0.1t$. Landau levels up to $n = 10$ are shown.

tetralayer graphene and ABBC stacked tetralayer graphene. For the ABCB stacked tetralayer graphene, the Landau levels look like a superposition of $B^{1/2}$ and $B^{3/2}$ levels, which is consistent with Fig. 4.6.(a). For the ABBA stacked tetralayer graphene, there are Landau levels crossing the zero-energy line, which is consistent with Fig. 4.6.(b). Detailed low-energy Landau-level spectrum analysis will be presented in Sec. 4.3.

4.2.4 Quantum Hall conductivity

Applying the Kubo formula to a disorder-free systems, we find that the conductivity tensor with an external magnetic field along z is given by

$$\sigma_{ij}(\omega) = -\frac{e^2}{2\pi\hbar l_B^2} \sum_n f_n \Omega_{ij}^n(\omega), \tag{4.33}$$

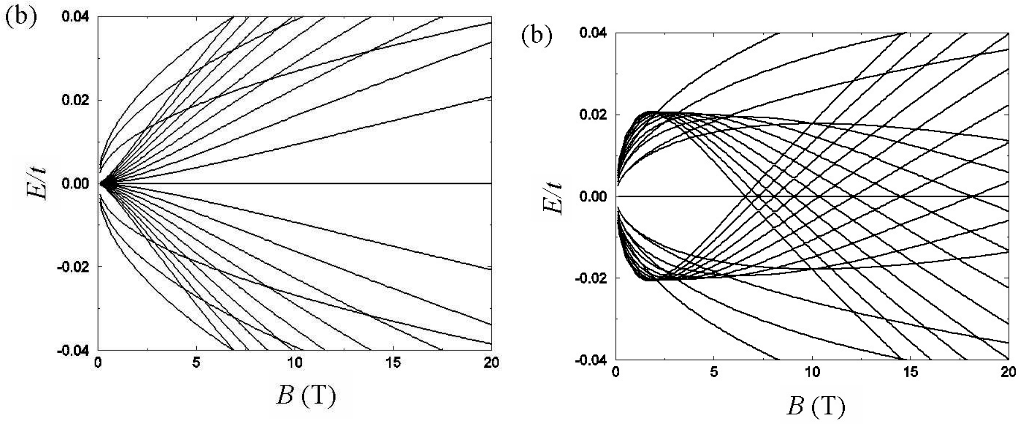

Figure 4.10: Landau levels of tetralayer graphene with (a) ABCB stacking and (b) ABBC stacking for nearest intralayer neighbor hopping $t = 3$ eV and nearest interlayer neighbor hopping $t_\perp = 0.1t$. Landau levels up to $n = 10$ are shown.

where f_n is Fermi factor of n-th energy state, $i, j = x, y$ and [2]

$$\Omega^n_{ij}(\omega) = i \sum_{m \neq n} \left[\frac{\langle n| \hbar v_i |m\rangle \langle m| \hbar v_j |n\rangle}{(\varepsilon_n - \varepsilon_m)(\varepsilon_n - \varepsilon_m + \hbar\omega + i\eta)} - \frac{\langle m| \hbar v_i |n\rangle \langle n| \hbar v_j |m\rangle}{(\varepsilon_n - \varepsilon_m)(\varepsilon_n - \varepsilon_m - \hbar\omega - i\eta)} \right]. \tag{4.34}$$

Here v_i is a velocity operator obtained by taking a derivative of the Hamiltonian $H(\boldsymbol{p})$ with respect to p_i. Note that in case of multilayer graphene, the velocity operator is constant, i.e. it does not depend on the Landau level index.

The appropriate quantized Hall conductivity is obtained by evaluating $\sigma_H = \sigma_{xy}(0)$. Detailed analysis of the quantum Hall conductivity will be presented in Sec. 4.4.

---

[2] Note that $\Omega^n_{ij}(\omega)$ was defined such that it reduces to the Berry curvature for $\omega = 0$.

4.3 Chiral decomposition of energy spectrum

In this section, we demonstrate an unanticipated low-energy property of graphene multilayers, which follows from an interplay between interlayer tunneling and the chiral properties of low-energy quasiparticles in an isolated graphene sheet. Our conclusions apply in the strongest form to models with only nearest-neighbor interlayer tunneling, but are valid over a broad field range as we explain below. We find that the low-energy band structure of any graphene multilayer consists of a set of independent pseudospin doublets. Within each doublet, the bands are described by a pseudospin Hamiltonian of the form

$$H_J(\boldsymbol{k}) \propto k^J \, [\cos(J\phi_{\boldsymbol{k}})\, \tau^x \pm \sin(J\phi_{\boldsymbol{k}})\, \tau^y\,], \tag{4.35}$$

where τ^α is a Pauli matrix acting on the doublet pseudospin, $\boldsymbol{k}$ is an envelope function momentum measured from either the K or K' corner of the honeycomb lattice's Brillouin-zone [1, 2], $k = |\boldsymbol{k}|$, and $\phi_{\boldsymbol{k}}$ is the orientation of $\boldsymbol{k}$. The $\pm$ sign in Eq. (4.35) assumes the opposite signs in graphene's K and K' valleys. Following the earlier work on graphene bilayers [30], we refer to J as the chirality index of a doublet. In the presence of a perpendicular magnetic field B, $H_J(\boldsymbol{k})$ yields J Landau levels at $E = 0$ and $E \neq 0$ levels with $|E| \propto B^{J/2}$. Taking the twofold spin and valley degeneracies into account, the number of independent zero-energy band eigenstates at the Dirac point ($\boldsymbol{k} = 0$) is therefore $8N_D$, where N_D is the number of pseudospin doublets.

We find that, although N_D depends on the details of the stacking sequence,

$$\sum_{i=1}^{N_D} J_i \ = N \tag{4.36}$$

in an N-layer stack. It follows from Eq. (4.36) that the Hall conductivity of an N-layer stack has strong integer quantum Hall effects with plateau conductivities,

$$\sigma_{xy} \ = \ \pm\frac{4e^2}{h}\left(\frac{N}{2}+n\right), \tag{4.37}$$

where n is a non-negative integer.

4.3.1 Partitioning rules

The low-energy band and the Landau level structure can be read off the stacking diagrams illustrated in Fig. 4.2 by partitioning a stack using the following rules, which are justified in the following section.

(i) Identify the longest nonoverlapping segments within which there are no reversals of stacking sense. When there is ambiguity in the selection of nonoverlapping segments, choose the partitioning which incorporates the largest number of layers. Each segment (including for interior segments the end layers at which reversals take place) defines a J-layer partition of the stack and may be associated with a chirality J doublet.

(ii) Iteratively partition the remaining segments of the stack into smaller J elements, excluding layers contained within previously identified partitions, until all layers are exhausted.

The chirality decompositions which follow from these rules are summarized in Table 4.1. Note that this procedure can result in $J = 1$ doublets associated with separated single layers which remain at the last step in the partitioning process.

In applying these rules, the simplest case is cyclic ABC stacking for which there are no stacking sense reversals and therefore a single $J = N$ partition. In the opposite limit, AB stacking, the stacking sense is reversed in every layer and the rules imply $N/2$ partitions with $J = 2$ for even N, and when N is odd a remaining $J = 1$ partition. Between these two limits, a rich variety of qualitatively distinct low-energy behaviors occur. For example, in the ABCB stacked tetralayer, ABC is identified as a $J = 3$ doublet and the remaining B layer gives a $J = 1$ doublet. The low-energy band structure and the Landau level structure of this stack, as illustrated in Figs. 4.6.(a) and 4.10.(a), have two sets of low-energy bands with $|E| \propto k, k^3$, Landau levels with $|E| \propto B^{1/2}, B^{3/2}$, and four zero-energy Landau levels per spin and valley. All these properties are predicted by the partitioning rules. We have explicitly checked that the rules correctly reproduce the low-energy electronic structure for all stacking sequences up to $N = 7$. Because each layer is a member of one and only one partition, the partitioning rules imply the chirality sum rule in Eq. (4.36).

stacking	chirality	stacking	chirality
ABC	3	ABCABC	6
ABA	2+1	ABCABA	5+1
		ABCACA	4+2
ABCA	4	ABCACB	4+2
ABCB	3+1	ABCBCA	3+3
ABAB	2+2	ABCBCB	3+2+1
ABAC	1+3	ABCBAB	3+2+1
		ABCBAC	3+3
ABCAB	5	ABABCA	2+4
ABCAC	4+1	ABABCB	2+3+1
ABCBC	3+2	ABABAB	2+2+2
ABCBA	3+2	ABABAC	2+1+3
ABABC	2+3	ABACAB	2+1+3
ABABA	2+2+1	ABACAC	1+3+2
ABACA	1+3+1	ABACBC	1+4+1
ABACB	1+4	ABACBA	1+5

Table 4.1: Chirality decomposition for $N = 3, 4, 5, 6$ layer stacks.

4.3.2 Degenerate state perturbation theory

We start from the well-known $J = 1$ massless Dirac equation [1, 2] $\boldsymbol{k} \cdot \boldsymbol{p}$ model for isolated sheets,

$$H_{MD}(\boldsymbol{p}) = -\begin{pmatrix} 0 & v\pi^\dagger \\ v\pi & 0 \end{pmatrix}, \tag{4.38}$$

where $\pi = p_x + ip_y$ and v is the quasiparticle velocity. In the presence of an external magnetic field, π and $\pi^\dagger$ are proportional to the Landau level raising and lowering operators, so that Eq. (4.38) implies the presence of one macroscopically degenerate Landau level at the Dirac point for each spin and valley, and therefore, to the $N = 1$ quantum Hall effect [16, 17] of Eq. (4.37).

An N-layer stack has a two-dimensional band structure with $2N$ atoms per unit cell. The Hamiltonian can be written as

$$H = H_{\perp} + H_{\parallel}, \tag{4.39}$$

where $H_{\perp}$ accounts for interlayer tunneling and $H_{\parallel}$ for intralayer tunneling. $H_{\parallel}$ is the direct product of massless Dirac model Hamiltonians H_{MD} for the sublattice pseudospin degrees of freedom of each layer. We construct a low-energy Hamiltonian by first identifying the zero-energy eigenstates of $H_{\perp}$ and then treating $H_{\parallel}$ as a perturbation.

Referring to Fig. 4.2, we see that $H_{\perp}$ is the direct product of a set of finite-length 1D tight-binding chains, as shown in Eq. (4.4), and a null matrix with dimension equal to the number of isolated sites. The set of zero-energy eigenstates of $H_{\perp}$ consists of the states localized on isolated sites and the single zero-energy eigenstates of each odd-length chain.

The low-energy effective Hamiltonian is evaluated by applying leading order degenerate state perturbation theory to the zero-energy subspace. The matrix element of the effective Hamiltonian between degenerate zero-energy states r and r' is given by [40]

$$\langle \Psi_r | H | \Psi_{r'} \rangle = \langle \Psi_r | \, H_{\parallel} \left[\hat{Q}(-H_{\perp}^{-1}) \hat{Q} H_{\parallel} \right]^{n-1} | \Psi_{r'} \rangle \, , \tag{4.40}$$

where n is the smallest positive integer for which the matrix element is nonzero, and $\hat{Q} = 1 - \hat{P}$, $\hat{P}$ is a projection operator onto the zero-energy subspace. To understand the structure of this Hamiltonian, it is helpful to start with some simple examples.

For ABC stacked N-layer graphene, the zero-energy states are the two isolated site states in bottom and top layers, α_1 and β_N. $N-1$ sets of two-site chains form high-energy states. Because $H_\parallel$ is diagonal in layer index and $H_\perp$ (and hence $H_\perp^{-1}$) can change the layer index by one unit, the lowest order at which α_1 and β_N are coupled is $n = N$.

According to Eq. (4.4), the wavefunction of each two-site chain is given by

$$|\Phi_{\sigma_r}\rangle = \frac{1}{\sqrt{2}}\big(|\beta_r\rangle + \sigma_r \, |\alpha_{r+1}\rangle \big), \tag{4.41}$$

with the energy $\epsilon_r = t_\perp \sigma_r$, where $\sigma_r = \pm 1$ and $r = 1, 2, \cdots, N-1$. From Eq. (4.40),

$$\begin{aligned} \langle \alpha_1 | H | \beta_N \rangle &= \langle \alpha_1 | \, H_\parallel \left[\hat{Q}(-H_\perp^{-1})\hat{Q} H_\parallel \right]^{N-1} |\beta_N\rangle \\ &= \sum_{\{\sigma_r\}} \frac{\big\langle \alpha_1 | H_\parallel | \Phi_{\sigma_1} \big\rangle \cdots \big\langle \Phi_{\sigma_{N-1}} | H_\parallel | \beta_N \big\rangle}{(-\varepsilon_1)\cdots(-\varepsilon_{N-1})} \\ &= -t_\perp \sum_{\{\sigma_r\}} \frac{(-\sigma_1/2)\cdots(-\sigma_{N-1}/2)}{(-\sigma_1)\cdots(-\sigma_{N-1})} (\nu^\dagger)^N \\ &= -t_\perp (\nu^\dagger)^N \sum_{\sigma_1, \cdots, \sigma_{N-1}} \frac{1}{2^{N-1}} \\ &= -t_\perp (\nu^\dagger)^N, \end{aligned} \tag{4.42}$$

where $\nu = v\pi / t_\perp$. Here $\langle \alpha_1 | V | \Phi_{\sigma_1} \rangle = -(1/\sqrt{2}) t_\perp \nu^\dagger$, $\big\langle \Phi_{\sigma_{N-1}} | V | \beta_N \big\rangle = -(\sigma_{N-1}/\sqrt{2}) t_\perp \nu^\dagger$ and $\big\langle \Phi_{\sigma_r} | V | \Phi_{\sigma_{r+1}} \big\rangle = -(\sigma_r/2) t_\perp \nu^\dagger$ were used. Thus, the effective Hamiltonian of N-layer graphene with ABC stacking has a single $J = N$ doublet given by

$$H_N^{eff} = -t_\perp \begin{pmatrix} 0 & (\nu^\dagger)^N \\ (\nu)^N & 0 \end{pmatrix}. \tag{4.43}$$

For AB stacked N-layer graphene, the high-energy Hilbert space consists of a single N-site 1D chain, excluding its zero-energy eigenstate when N is odd. There is an isolated site in each layer which is connected to both its neighbors at order $n = 2$ forming an isolated site chain. When N is even, this chain is diagonalized by $N/2$, $J = 2$ doublets formed between α-sublattice and β-sublattice chain states [39, 41–43]. When N is odd, the zero-energy chain state is mapped to an equal-magnitude oscillating-sign linear combination of isolated site states by intralayer tunneling at order $n = 1$, yielding a $J = 1$ doublet. The $(N - 1)/2$, $J = 2$ doublets are then formed between α-sublattice and β-sublattice isolated site chain states in the orthogonal portion of the isolated state subspace.

Let's consider the low-energy spectrum of AB stacking in more detail. From Eq. (4.4) energy spectra and wavefunctions of the single N-site chain are given by

$$\begin{aligned} \varepsilon_r &= 2t_\perp \cos\theta_r, \qquad (4.44) \\ |\Phi_r\rangle &= \sqrt{\frac{2}{N+1}}\big(\sin\theta_r\,|\beta_1\rangle + \sin 2\theta_r\,|\alpha_2\rangle + \sin 3\theta_r\,|\beta_3\rangle + \sin 4\theta_r\,|\alpha_4\rangle\cdots\big), \end{aligned}$$

where $\theta_r = \frac{r\pi}{N+1}$ and $r = 1, 2, \cdots, N$.

First, let's consider the case with even N. Then the low-energy states come from the isolated sites or equivalently their superpositions. Let's define

$$|\Psi_r\rangle = \sqrt{\frac{2}{N+1}}\big(\sin\theta_r e^{-i\phi}\,|\alpha_1\rangle + \sin 2\theta_r e^{i\phi}\,|\beta_2\rangle + \sin 3\theta_r e^{-i\phi}\,|\alpha_3\rangle + \sin 4\theta_r e^{i\phi}\,|\beta_4\rangle\cdots\big) \qquad (4.45)$$

such that

$$\langle \Psi_r | V | \Phi_s \rangle = -\delta_{r,s} |\nu|, \tag{4.46}$$

where $e^{i\phi} = \nu/|\nu|$. Then the matrix elements between the low-energy states are given by the second order perturbation theory:

$$\langle \Psi_r | H | \Psi_{r'} \rangle = \sum_{s=1}^{N} \frac{\langle \Psi_r | V | \Phi_s \rangle \langle \Phi_s | V | \Psi_{r'} \rangle}{(-\varepsilon_s)} = -\delta_{r,r'} (t_\perp^2 / \varepsilon_r) |\nu|^2. \tag{4.47}$$

Note that $\varepsilon_r = -\varepsilon_{N+1-r}$ and these two modes form a 2-chiral system with energies $\pm|\varepsilon_r|$. The chirality can be manifested clearly if we define

$$\begin{aligned} |\tilde{\alpha}_r\rangle &= \frac{e^{i\phi}}{\sqrt{2}} \left(|\Psi_r\rangle + |\Psi_{N+1-r}\rangle \right), \\ \left|\tilde{\beta}_r\right\rangle &= \frac{e^{-i\phi}}{\sqrt{2}} \left(|\Psi_r\rangle - |\Psi_{N+1-r}\rangle \right). \end{aligned} \tag{4.48}$$

Then the Hamiltonian of the 2-chiral system for $r = 1, 2, \cdots, N/2$ is given by

$$H_r = -\frac{t_\perp^2}{\varepsilon_r} \begin{pmatrix} 0 & (\nu^\dagger)^2 \\ (\nu)^2 & 0 \end{pmatrix} = -\begin{pmatrix} 0 & \frac{(\pi^\dagger)^2}{2m_r} \\ \frac{(\pi)^2}{2m_r} & 0 \end{pmatrix} \tag{4.49}$$

in a $(\tilde{\alpha}_r, \tilde{\beta}_r)$ basis with $m_r v^2 = t_\perp \cos\left(\frac{r\pi}{N+1}\right)$. Thus the system is described by a combination of massive Dirac modes with different masses.

For odd N, there is a zero-energy state in the N-site chain at $r = (N+1)/2$ in Eq. (4.44). Thus in addition to the massive modes, there exists one massless Dirac mode,

$$\left\langle \Psi_{\frac{N+1}{2}} | V | \Phi_{\frac{N+1}{2}} \right\rangle = -|\nu|. \tag{4.50}$$

Thus the system is described by one massless Dirac mode and a combination of massive Dirac modes with different masses.

A more complex and more typical example is realized by placing a single reversed layer on top of ABC stacked N-layer graphene with $N > 2$. Note that the last chain has three sites, thus it has a zero-energy state β_N^- defined by

$$\left|\beta_N^-\right\rangle = \frac{1}{\sqrt{2}}\left(\left|\beta_{N-1}\right\rangle - \left|\beta_{N+1}\right\rangle\right), \tag{4.51}$$

and two high-energy states defined by

$$\left|\Phi_{\sigma_{N-1}}\right\rangle = \frac{1}{\sqrt{2}}\left(\left|\beta_{N-1}\right\rangle + \frac{\sigma_{N-1}}{\sqrt{2}}\left|\alpha_N\right\rangle + \left|\beta_{N+1}\right\rangle\right), \tag{4.52}$$

where $\sigma_{N-1} = \pm 1$. Then the first-order perturbation theory gives

$$\left\langle \alpha_{N+1}|H|\beta_N^-\right\rangle = \frac{t_\perp}{\sqrt{2}}\nu\dagger, \tag{4.53}$$

suggesting the existence of the massless Dirac mode with *reduced* velocity.

Similarly as Eq. (4.42), we obtain

$$H_{N+1}^{eff} = -t_\perp \begin{pmatrix} 0 & \frac{\nu^\dagger}{\sqrt{2}} & 0 & \frac{(\nu^\dagger)^2}{2} \\ \frac{\nu}{\sqrt{2}} & 0 & -\frac{(\nu)^{N-1}}{\sqrt{2}} & 0 \\ 0 & -\frac{(\nu^\dagger)^{N-1}}{\sqrt{2}} & 0 & \frac{(\nu^\dagger)^N}{2} \\ \frac{\nu^2}{2} & 0 & \frac{(\nu)^N}{2} & 0 \end{pmatrix}, \tag{4.54}$$

using a $(\alpha_{N+1}, \beta_{N+1}^-, \alpha_1, \beta_N)$ basis. The first 2×2 block in Eq. (4.54) gives a $J = 1$ doublet with a reduced velocity. Note that the matrix in Eq. (4.54) is not block diagonal thus we cannot simply say that the second 2×2 matrix block is a N-chiral system. The $J = N$ doublet in this instance includes both the (α_1, β_N) subspace contribution and an equal contribution due to perturbative coupling to the $(\alpha_{N+1}, \beta_{N+1}^-)$ subspace. Using a similar perturbation theory shown in Eq. (4.22), we can obtain higher order correction by integrating out the massless Dirac mode which forms a higher energy state. Then the final Hamiltonian is reduced to

$$H_{N+1}^{eff} \approx H_1 \otimes H_N, \tag{4.55}$$

where

$$H_1 = -t_\perp \begin{pmatrix} 0 & \nu^\dagger/\sqrt{2} \\ \nu/\sqrt{2} & 0 \end{pmatrix}, \quad H_N = -t_\perp \begin{pmatrix} 0 & (\nu^\dagger)^N \\ (\nu)^N & 0 \end{pmatrix}. \tag{4.56}$$

This means that the combined system can be described by a combination of one 1-chiral system with reduced velocity and one N-chiral system. Note that stacking a layer with an opposite handedness partitions a system into systems with different chiralities.

The relationship between the electronic structure of a general stack and the partitioning procedure explained above can be understood as follows.

(i) First, note that a partition with chirality J has isolated sites in its terminal layers that are coupled at order J in perturbation theory. In the case of $J = 1$ partition, the chain opposite to the single isolated site always has an odd length and provides the zero-energy partner; isolated site to chain coupling therefore always occurs at first order.

(ii) Next, consider the perturbation theory, truncating at successively higher orders. When truncated at first order, the $J = 1$ partitions are isolated by higher J blocks within which the Hamiltonian vanishes. Each $J = 1$

partition therefore yields a separate massless Dirac equation with velocities [3] that can be smaller than the graphene sheet Dirac velocity. When the perturbation theory is truncated at second order, the Hamiltonian becomes nonzero within the $J = 2$ partitions. The eigenenergies within the $J = 1$ partitions are parametrically larger, and the Hamiltonian within the $J > 2$ partitions is still zero. To leading order therefore, the $J = 2$ partitions are separated, and their isolated states are coupled at the second order in perturbation theory so that each provides a $J = 2$ doublet such as that of an isolated bilayer. If two or more $J = 2$ partitions are adjacent, then their Hamiltonians do not separate. In this case, there is a chain of second order couplings between isolated states, such as those of an even-length AB stack, but the end result is still $J = 2$ doublet for each $J = 2$ partition.

(iii) The identification between partitions and chiral doublets can be established by continuing this consideration up to the highest values of J which occur for a particular stack.

(iv) Then, the effective Hamiltonian of any N-layer graphene is as follows:

$$H_N^{eff} \approx H_{J_1} \otimes H_{J_2} \otimes \cdots \otimes H_{J_{N_D}}, \tag{4.57}$$

---

[3] The velocity of the $J = 1$ doublets is determined by the strength of the coupling between the odd-length chain zero-energy state and isolated states on the sublattice opposite to the chain ends. For a chain of length $2N-1$, the chain's zero-energy state has nonzero amplitude on the N odd-index sites. The velocity is reduced from the single sheet velocity by a factor of $\sqrt{M/N}$, where M is the number of isolated sites opposite to the N odd-index sites. In a similar manner, higher J doublet Hamiltonians are sometimes altered by a multiplicative factor by perturbative coupling to smaller J doublets as in the single reversed layer example.

with the sum rule in Eq. (4.36). Note that N_D is half the sum of the number of isolated sites and the number of odd-length chains.

4.4 Discussion

4.4.1 Effects of remote hopping

The minimal model we have used to derive these results is approximately valid in the broad intermediate magnetic field B range between ~ 10 and ~ 100 T, over which the intralayer hopping energy in field ($\sim \hbar v/\ell$ where $\ell = \sqrt{\hbar c/e|B|} \sim 25\,\mathrm{nm}/[B(\mathrm{T})]^{1/2}$ is the magnetic length) is larger than the distant neighbor interlayer hopping amplitudes that we have neglected ($\gamma_2 \sim -20$ meV), but still smaller than $t_\perp$. For example, if we consider $\alpha_1 \to \alpha_3$ hopping process in ABA stacked trilayer in Fig. 4.2, the valid range of magnetic field for the minimal model is given by

$$|\gamma_2| < \frac{(\hbar v/l)^2}{t_\perp} < t_\perp. \tag{4.58}$$

When γ_2 does not play an important role (in $N = 2$ stacks, for example), the lower limit of the validity range is parametrically smaller. The minimum field in bilayers has been estimated to be ~ 1 T [30], by comparing intralayer hopping with the $\gamma_3 \sim 0.3$ eV interlayer hopping amplitude,

$$\hbar v_3/l < \frac{(\hbar v/l)^2}{t_\perp} < t_\perp, \tag{4.59}$$

where $v_3 = (\sqrt{3}/2)a\gamma_3/\hbar$ and a is a lattice constant of graphene.

Figure 4.11 and Figure 4.12 show the Landau level spectrum at the K valley as a function of γ_3 for an AB stacked bilayer, and as a function of

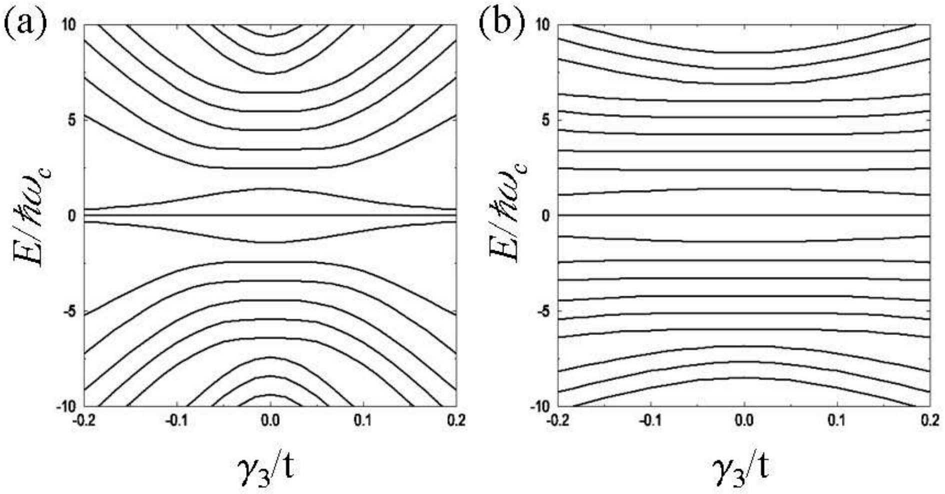

Figure 4.11: Landau level spectrum near the K valley as a function of γ_3 for an AB stacked bilayer for (a) $B = 0.1$ T and (b) $B = 1$ T. Here $t = 3$ eV, $t_\perp = 0.1t$, and $\omega_c = eB/mc$, with $m = t_\perp/2v^2$, were used.

γ_2 for an ABA stacked trilayer, respectively. In the case of the bilayer, the dependence of the Landau levels on γ_3 is weak for B larger than 1 T, whereas in the case of the trilayer, the Landau level spectrum still strongly depends on γ_2 for $B = 1$ T, but the dependence becomes weak for B above 10 T, confirming the above argument.

4.4.2 Quantum Hall effect

In Fig. 4.13, we plot the noninteracting Hall conductivity as a function of Fermi energy for the four distinct four-layer stacks. When electron-electron interactions are included at an electrostatic mean-field (Hartree) level and the neutralizing ionized dopants (responsible for the Fermi energy shift away from

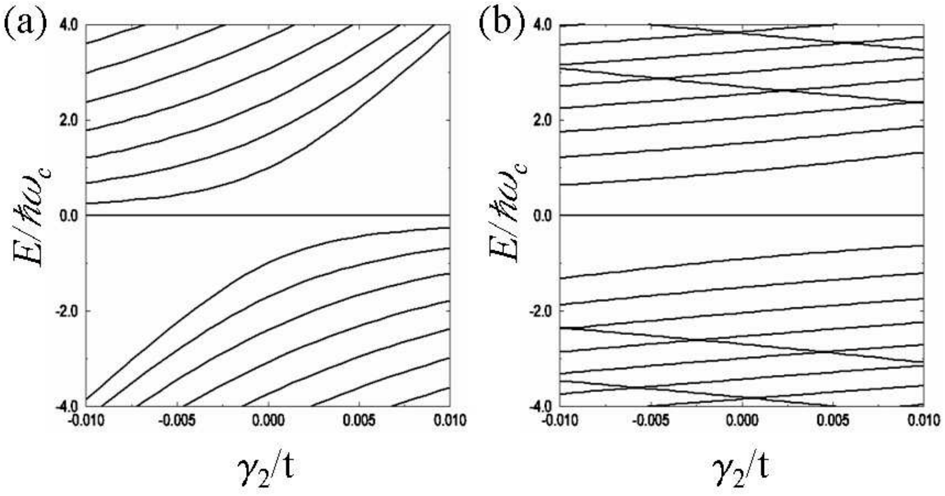

Figure 4.12: Landau level spectrum near the K valley as a function of γ_2 for an ABA stacked trilayer for (a) $B = 1$ T and (b) $B = 10$ T. Here $t = 3$ eV, $t_\perp = 0.1t$, and $\omega_c = eB/mc$, with $m = t_\perp/2v^2$, were used. Note that for this case the Landau level structures near K and K' valleys are not identical.

the Dirac point) are assumed to be equally distributed among the layers, the Landau levels with $E \neq 0$ are shifted by electrostatic potential differences between the layers. There is, however, no influence of electrostatics on the $E = 0$ levels. This property follows from the perfect particle-hole symmetry of the models we employ, which implies a uniform charge distribution among the layers at the neutrality point. Remote (γ_2 2nd neighbor) interlayer hopping *does* shift the $E = 0$ Landau level in the ABAB stacked tetralayer and weakly lifts the degeneracy responsible for the large jump between the $\pm(4e^2/h)N/2$ Hall plateaus. This example demonstrates a tendency toward the grouping of N spin and valley degenerate Landau levels very close to $E = 0$ in general N-layer stacks even when remote neighbor hopping is included. Small gaps between

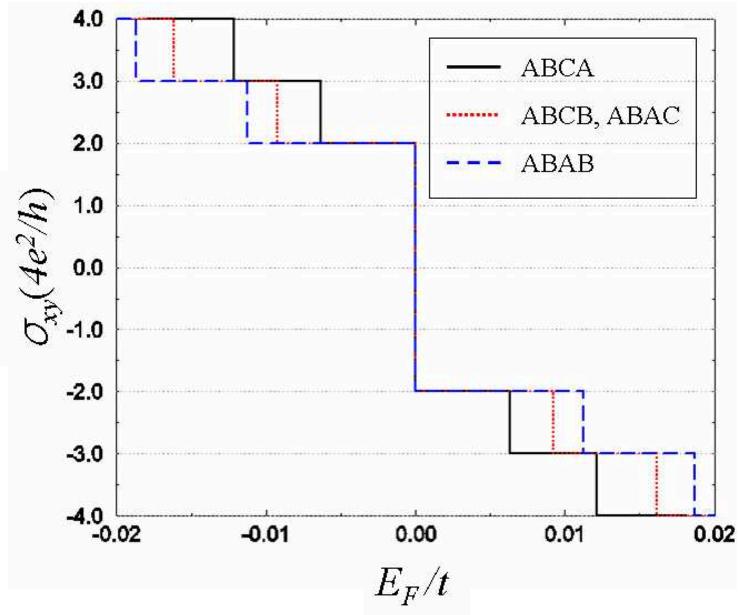

Figure 4.13: Noninteracting system Hall conductivity as a function of the Fermi energy for all inequivalent four-layer graphene stacks when $B = 10$ T, $t = 3$ eV, and $t_{\perp} = 0.1t$. The dependence of the Hall conductivity on Fermi energy is simply related to the dependence of the Hall conductivity on total electron density. The Hall conductivity calculations shown in this figure assume neutralizing ionized donors spread equally between the four layers.

these Landau levels are unlikely to lead to Hall plateaus unless disorder is very weak. When disorder is weak, on the other hand, electron-electron interaction effects beyond Hartree level are likely to be important and lead to strong quantum Hall effects at many filling factors, often ones associated with broken symmetries of different types. [44–49]. The property that the Hall conductivity will tend to jump by four units on crossing the Dirac point for arbitrarily stacked tetralayer graphene is the most obvious experimental manifestation of the chirality sum rule discussed in this chapter. In practice charged multilayers ($E_F \neq 0$) would normally be prepared by placing the system on one side of an electrode and gating. Even though gating will redistribute charge and shift electric potentials differently in different layers, the Landau level bunching we discussed should still be clearly reflected in quantum Hall effect measurements.

4.4.3 Effects of the same stacking inside

The analysis presented so far is based on the assumption that stacking one layer directly on top of its neighbor, AA stacking, is not allowed. When interior AA stacking does occur, we can still apply a similar diagram analysis and identify the zero-energy states at the Dirac point. In this case, however, zero-energy states can appear not only at the Dirac points but also at other points in momentum space. The degenerate state perturbation theory at the Dirac point discussed so far therefore can not completely capture the low-energy states.

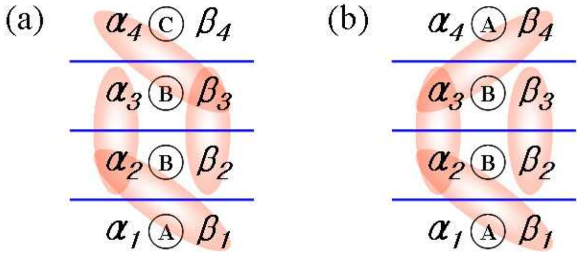

Figure 4.14: Stacking diagrams for tetralayer graphene with (a) ABBC stacking and (b) ABBA stacking. Shaded ovals link nearest interlayer neighbors.

As an example, let's consider ABBC stacked tetralayer graphene, as illustrated in Fig. 4.14.(a). Here, in addition to α_1 and β_4, there are two zero-energy states at each three-site-chain defined by

$$
\begin{aligned}
\left|\tilde{\beta}_1\right\rangle &= \frac{1}{\sqrt{2}}\left(|\beta_1\rangle - |\alpha_3\rangle\right), \\
|\tilde{\alpha}_4\rangle &= \frac{1}{\sqrt{2}}\left(|\alpha_4\rangle - |\beta_2\rangle\right).
\end{aligned}
\tag{4.60}
$$

Thus the matrix elements between low-energy states are given by

$$
\left\langle\alpha_1|H|\tilde{\beta}_1\right\rangle = \langle\tilde{\alpha}_4|H|\beta_4\rangle = -\frac{t_\perp}{\sqrt{2}}\nu^\dagger. \tag{4.61}
$$

Therefore the system can be described by two massless Dirac modes with reduced velocity, as shown in Figs. 4.6.(b) and 4.10.(b).

Another example is ABBA stacked tetralayer graphene, as illustrated in Fig. 4.14.(b). In this case, there are two zero-energy states at α_1 and α_4. The high-energy states Φ_r are given by Eq. (4.4) with $N = 4$, thus we get

$$
\langle\alpha_1|H|\alpha_4\rangle = \sum_{r=1}^{4} \frac{\langle\alpha_1|V|\Phi_r\rangle\langle\Phi_r|V|\alpha_4\rangle}{(-\epsilon_r)} = -ct_\perp|\nu|^2 \tag{4.62}
$$

where $c = \frac{1}{5}\sum_r \sin\left(\frac{r\pi}{5}\right)\sin\left(\frac{4r\pi}{5}\right)/\cos\left(\frac{r\pi}{5}\right) = -1$. Here the low-energy state is composed of one *non-chiral* massive mode. Note that because of the non-chirality, there are no zero-energy Landau levels.

4.4.4 Summary

We have shown that N-layer graphene at intermediate and strong magnetic fields has a strong tendency towards the appearance of N spin and orbitally degenerate Landau levels very close to $E = 0$. This property should lead to strong quantum Hall effects at $\pm(4e^2/h)N/2$ in many N-layer stacks.

The origin of this behavior is the following *chirality sum rule*: i) The low-energy bands of multilayer graphene can be decomposed into N_D doublets with chirality J_i. ii) Although N_D depends on the stacking sequence, $\sum_{i=1}^{N_D} J_i = N$ in an N-layer stack.

The chirality sum rule applies precisely only to idealized models with only nearest-neighbor intralayer and interlayer tunneling. It nevertheless suggests the likelihood of interesting interaction physics and broken symmetry ground states in many neutral or weakly doped multilayer graphene samples.

Chapter 5

Pseudospin Magnetism in Graphene

In this chapter, we predict that neutral graphene bilayers are pseudospin magnets in which the charge density-contribution from each valley and spin spontaneously shifts to one of the two layers. The band structure of this system is characterized by a momentum-space vortex which is responsible for unusual competition between kinetic and interaction energies leading to symmetry breaking in the vortex core. We discuss the possibility of realizing a pseudospin version of ferromagnetic metal spintronics in graphene bilayers based on hysteresis associated with this broken symmetry. [1]

5.1 Introduction

The ground state of an interacting electron system flows from subtle compromises between band and interaction energy minimization. Because of the Pauli blocking effects which underlie Fermi liquid theory however, the consequences of interactions are normally only quantitative [50] unless symmetries are broken. In this chapter we argue that band energy minimization is

---

[1] The contents of this chapter are based on the article: Hongki Min, Giovanni Borghi, Marco Polini, and A. H. MacDonald, *Pseudospin magnetism in graphene*, Phys. Rev. B **77**, 041407(R) (2008).

exceptionally frustrating to interactions in graphene bilayers, and predict that broken symmetry states in which charge shifts spontaneously from one layer to the other occur as a consequence.

Graphene bilayers with Bernal stacking have one low-energy site per unit cell in each layer. When the layer degree of freedom is described as a pseudospin, the continuum limit of the π-orbital band Hamiltonian corresponds [27, 30] to a pseudospin field $\boldsymbol{B}_{\text{band}} = [\hbar^2 k^2/(2m)]\,(\cos(2\phi_{\boldsymbol{k}}), \sin(2\phi_{\boldsymbol{k}}), 0)$, where $\phi_{\boldsymbol{k}} = \arctan{(k_y/k_x)}$, $m = \gamma_1/(2v_{\text{F}}^2)$, γ_1 is the interlayer tunneling amplitude, and v is the electron velocity at the Fermi energy in an isolated neutral graphene sheet. When interactions are neglected the ground state of a neutral bilayer has a full valence band of pseudospinors aligned at each $\boldsymbol{k}$ with this pseudospin field, forming the momentum-space vortex. The vortex exacts a large interaction energy penalty because of its rapid pseudospin-orientation variation. We propose that, like its real-space counterpart [2], the momentum-space vortex sidesteps this energy cost by forming a vortex core in which the pseudospin orientation is out of plane in either the $\hat{z}$ or $-\hat{z}$ direction, as illustrated in Fig. 5.1. The momentum-space vortex state is nonuniform in momentum space, but in real space transfers charge uniformly between layers. This chapter starts by describing a technical calculation that supports and elaborates on our prediction and then discusses anticipated properties of this state.

---

[2] See for example [51] and work cited therein.

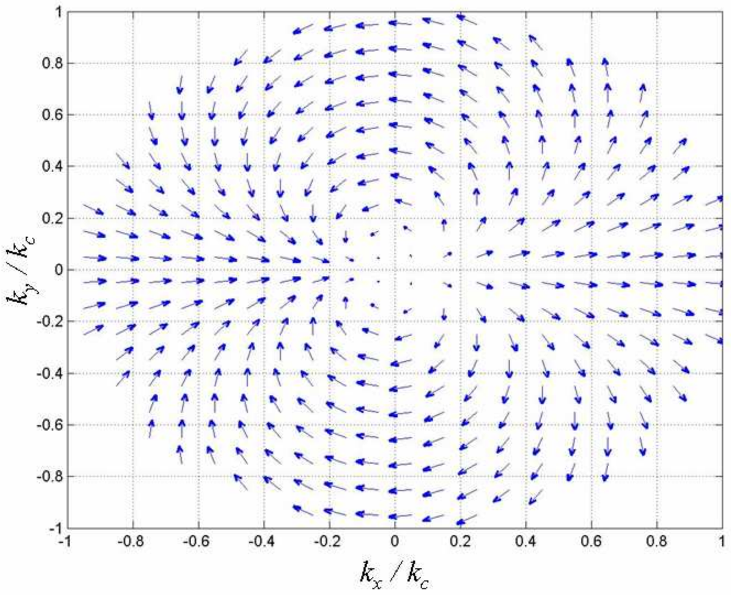

Figure 5.1: Pseudospin orientation in a graphene bilayer broken symmetry state. In this figure the arrows represent both the magnitude and the direction of the $\hat{x}$-$\hat{y}$ projection of the pseudospin orientation $\hat{n}$ as obtained from a mean-field-theory calculation for a neutral, unbiased bilayer with coupling constant $\alpha = 1$. The arrows are shorter in the core of the momentum space vortex because the pseudospins in the core have rotated spontaneously toward the $\hat{z}$ or $-\hat{z}$ direction.

5.2 Chiral two-dimensional electron system Hartree-Fock Theory

It is instructive to consider a class of chiral two-dimensional electron system (C2DES) models which includes the continuum limits of single-layer and bilayer graphene sheets as special cases. These C2DES models have band

Hamiltonians,

$$\hat{\mathcal{H}}_{\rm band} = -\sum_{\boldsymbol{k},\sigma',\sigma} \hat{c}^{\dagger}_{\boldsymbol{k},\sigma'} \left\{ \varepsilon_0(k_{\rm c}) \left(\frac{k}{k_{\rm c}}\right)^J \left[\cos(J\phi_{\boldsymbol{k}})\,\tau^x_{\sigma',\sigma} + \sin(J\phi_{\boldsymbol{k}})\,\tau^y_{\sigma',\sigma}\right] + \frac{V_{\rm g}}{2}\,\tau^z_{\sigma',\sigma} \right\} \hat{c}_{\boldsymbol{k},\sigma}\,, \tag{5.1}$$

where σ, σ' are pseudospin labels, J is the chirality index, τ^a is a Pauli matrix, $k_{\rm c}$ is the model's ultraviolet momentum cutoff, $\varepsilon_0(k_{\rm c})$ is the energy scale of the band Hamiltonian, and a sum over valley and spin components is implicit. In Eq. (5.1), $V_{\rm g}$ is an external potential term which couples to the pseudospin magnet order parameter and corresponds in the case of bilayer graphene to an external potential difference between the layers. For single-layer graphene $J = 1$ and $\varepsilon_0(k_{\rm c}) = \hbar v k_{\rm c}$, while for bilayer graphene $J = 2$ and $\varepsilon_0(k_{\rm c}) = \hbar^2 k_{\rm c}^2/(2m)$. The dimensionless coupling constant of these C2DESs, which measures the interaction strength, can be defined as $\alpha = (e^2 k_{\rm c}/\epsilon)/\varepsilon_0(k_{\rm c})$ where ϵ is the effective dielectric function due to screening external to the π electron system. In the case of a single graphene layer $\alpha_{\rm mono} = e^2/(\epsilon v \hbar)$, while in the bilayer case, $\alpha_{\rm bi} = 2e^2/(\epsilon v_{\rm c} \hbar)$, where $v_{\rm c} = \hbar k_{\rm c}/m$. If we choose [52] $\hbar k_{\rm c} = \sqrt{2m\gamma_1}$ for the bilayers, we have $\alpha_{\rm bi} = \alpha_{\rm mono}$. Typically $\epsilon \sim 2.5$ which implies a dimensionless coupling constant $\alpha \sim 1$. We use $\varepsilon_0(k_{\rm c})$ and $k_{\rm c}^{-1}$ as energy and length units in the rest of this chapter.

The C2DES Hartree-Fock Hamiltonian can be written (in dimensionless units) in the following physically transparent form:

$$\hat{\mathcal{H}}_{\rm HF} = -\sum_{\boldsymbol{k},i,\sigma',\sigma} \hat{c}^{\dagger}_{\boldsymbol{k},i,\sigma'} \mathcal{B}^{(i)}_{\sigma',\sigma}(\boldsymbol{k}) \hat{c}_{\boldsymbol{k},i,\sigma}\,, \tag{5.2}$$

where $\mathcal{B}^{(i)}_{\sigma',\sigma} = B^{(i)}_0(\boldsymbol{k})\delta_{\sigma',\sigma} + \boldsymbol{B}^{(i)}(\boldsymbol{k}) \cdot \boldsymbol{\tau}_{\sigma',\sigma}$,

$$B^{(i)}_0(\boldsymbol{k}) = \alpha \int_{|\boldsymbol{k}'|<1} \frac{d^2\boldsymbol{k}'}{2\pi} \frac{1}{|\boldsymbol{k}-\boldsymbol{k}'|} \frac{f^{(i)}_{\text{sum}}(\boldsymbol{k}')}{2} \,, \tag{5.3}$$

and the pseudospin field $\boldsymbol{B}^{(i)}(\boldsymbol{k})$ has band and interaction contributions,

$$B^{(i)}_x(\boldsymbol{k}) = k^J \cos(J\phi_{\boldsymbol{k}}) + \alpha \int_{|\boldsymbol{k}'|<1} \frac{d^2\boldsymbol{k}'}{2\pi} \frac{e^{-|\boldsymbol{k}-\boldsymbol{k}'|\bar{d}}}{|\boldsymbol{k}-\boldsymbol{k}'|} \frac{f^{(i)}_{\text{diff}}(\boldsymbol{k}')}{2} \, n^{(i)}_x(\boldsymbol{k}') \,, \tag{5.4}$$

$$B^{(i)}_y(\boldsymbol{k}) = k^J \sin(J\phi_{\boldsymbol{k}}) + \alpha \int_{|\boldsymbol{k}'|<1} \frac{d^2\boldsymbol{k}'}{2\pi} \frac{e^{-|\boldsymbol{k}-\boldsymbol{k}'|\bar{d}}}{|\boldsymbol{k}-\boldsymbol{k}'|} \frac{f^{(i)}_{\text{diff}}(\boldsymbol{k}')}{2} \, n^{(i)}_y(\boldsymbol{k}') \,, \tag{5.5}$$

$$B^{(i)}_z(\boldsymbol{k}) = \frac{\bar{V}_g}{2} + \alpha \sum_j \int_{|\boldsymbol{k}'|<1} \frac{d^2\boldsymbol{k}'}{2\pi} \left(\frac{1}{|\boldsymbol{k}-\boldsymbol{k}'|} \delta_{i,j} - \bar{d} \right) \frac{f^{(j)}_{\text{diff}}(\boldsymbol{k}')}{2} \, n^{(j)}_z(\boldsymbol{k}') \,. \tag{5.6}$$

Here i, j label the four valley and spin components of graphene's $J = 1$ and $J = 2$ C2DESs, $\boldsymbol{n}^{(i)}(\boldsymbol{k})$ is the direction of $\boldsymbol{B}^{(i)}(\boldsymbol{k})$, $f^{(i)}_{\text{sum}}(\boldsymbol{k}')$ $[f^{(i)}_{\text{diff}}(\boldsymbol{k}')]$ is the sum of (difference between) low- and high-energy occupation numbers, $\bar{V}_{\text{g}} = V_{\text{g}}/\varepsilon_0(k_{\text{c}})$ is the gate potential in units of $\varepsilon_0(k_{\text{c}})$, $\bar{d} = k_c d$ is the distance between layers in units of k_c^{-1} in the bilayer case, and $\bar{d} = 0$ in the monolayer case. The term proportional to $\bar{d}$ on the right-hand side of Eq. (5.6) is the Hartree potential which opposes charge transfer between layers in the bilayer case. See Appendix C for a brief overview of the Hartree-Fock theory and detailed derivations.

Local minima of the Hartree-Fock energy functional solve Eqs. (5.4)-(5.6) self-consistently. Our focus here is on the broken symmetry momentum-space vortex solutions in which pseudospins near $\boldsymbol{k} = 0$ tilt away from their band Hamiltonian $\hat{x}$-$\hat{y}$ plane orientations toward the $\pm\hat{z}$ direction, *i.e.*, $\boldsymbol{n}^{(i)}(\boldsymbol{k}) =$

$(n_\perp^{(i)}(k)\cos(J\phi_{\boldsymbol{k}}), n_\perp^{(i)}(k)\sin(J\phi_{\boldsymbol{k}}), n_z^{(i)}(k))$ with $[n_\perp^{(i)}(k)]^2+[n_z^{(i)}(k)]^2=1$. Pseudospin polarization in the $\hat{z}$-direction corresponds to charge transfer between layers. This *ansatz* yields effective magnetic fields whose $\hat{x}$-$\hat{y}$ plane projections are parallel to the band Hamiltonian effective field. We find that $\boldsymbol{B}^{(i)}(\boldsymbol{k}) = (B_\perp^{(i)}(k)\cos(J\phi_{\boldsymbol{k}}), B_\perp^{(i)}(k)\sin(J\phi_{\boldsymbol{k}}), B_z^{(i)}(k))$ with

$$B_\perp^{(i)}(k) = k^J + \alpha \int_0^1 dk' F_\perp(k,k')\, f_{\text{diff}}^{(i)}(k')\, n_\perp^{(i)}(k'), \tag{5.7}$$

$$B_z^{(i)}(k) = \frac{\bar{V}_g}{2} + \alpha \sum_j \int_0^1 dk' \left(F_z(k,k')\delta_{i,j} - \frac{1}{2}k'\bar{d}\right) f_{\text{diff}}^{(j)}(k')\, n_z^{(j)}(k')\,, \tag{5.8}$$

where the exchange kernels in Eqs. (5.7) and (5.8) are given by

$$\begin{aligned} F_\perp(k,k') &= k' \int_0^\pi \frac{d\phi}{2\pi}\, \frac{e^{-q\bar{d}}}{q} \cos(J\phi), \\ F_z(k,k') &= k' \int_0^\pi \frac{d\phi}{2\pi}\, \frac{1}{q}, \end{aligned} \tag{5.9}$$

with $q = q(k,k',\phi) \equiv \sqrt{k^2 + k'^2 - 2kk'\cos(\phi)}$. The pseudospin-chirality induced frustration is represented by the factor $\cos(J\phi)$ in the first line of Eq. (5.9) which makes $F_\perp$ much smaller than F_z, as illustrated in Fig. 5.2.

5.3 Pseudospin magnet phase diagram

We test the stability of the "normal" state $[n_z^{(i)}(k) \equiv 0$ at $V_{\mathrm{g}} = 0]$ solution of the Hartree-Fock equations by linearizing the self-consistency condition; $n_z^{(i)} = B_z^{(i)} n_\perp^{(i)} / B_\perp^{(i)} \to B_z^{(i)}/B_\perp^{(i)}|_{n_z^{(i)} \equiv 0}$. This gives a k-space integral equation

$$n_z^{(i)}(k) = \sum_j \int_0^1 dk'\, M_{i,j}(k,k')\, n_z^{(j)}(k'), \tag{5.10}$$

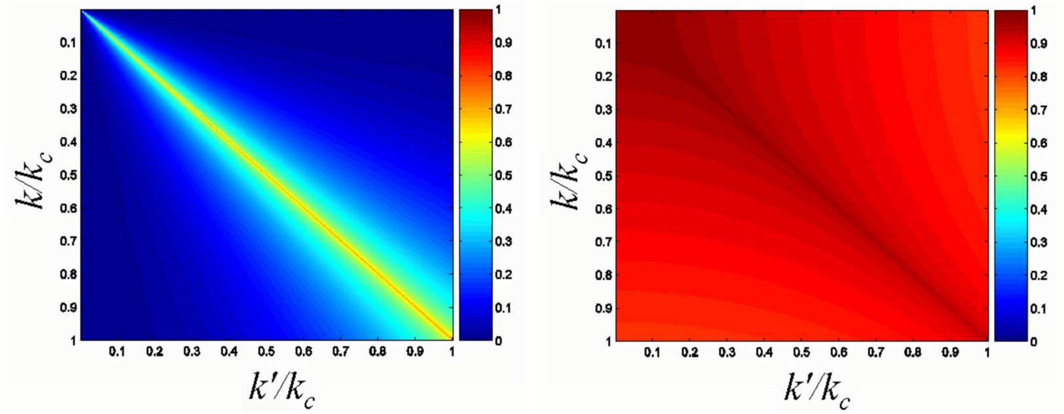

Figure 5.2: Ratio of exchange kernels, $F_\perp(k,k')/F_z(k,k')$ of the bilayer chiral (left) and non-chiral (right) model with $k_c d = 0.2$. Here the non-chiral model means no $\cos(J\phi)$ term in $F_\perp(k,k')$ in Eq. (5.9).

where

$$M_{i,j}(k,k') = \frac{\alpha[F_z(k,k')\delta_{i,j} - k'\bar{d}/2]\ f^{(j)}_{\text{diff}}(k')}{k^J + \alpha \displaystyle\int_0^1 dk'' F_\perp(k,k'')\ f^{(i)}_{\text{diff}}(k'')}\,. \tag{5.11}$$

The normal state is stable when the largest eigenvalue of the linear integral operator M in the right-hand side of Eq. (5.10) is smaller than 1. Eigenvalues larger than 1 are possible only because $F_\perp$ is smaller than F_z, *i.e.*, because of pseudospin chirality. Phase diagrams for $J = 2$ and $J = 1$ are plotted in Fig. 5.3. The pseudospin magnet is more stable for larger coupling constant because it is driven by interactions, for larger J because the typical value of the band energy term proportional to k^J decreases with J, and for smaller doping because $f^{(i)}_{\text{diff}}(k)$ is then nonzero in a larger region of k-space. The eigenvectors of M specify the instability channel. The component-index structure of M implies that the eigenvalues occur in groups of four, three of which [labeled *antiferromagnetic* (AF) in Fig. 5.3] correspond in bilayers to states with no net charge transfer, *i.e.*, $\sum_j n_z^{(j)}(k) \equiv 0$. The *ferromagnetic* (F) instability in which all components are polarized in the same sense is opposed by the Hartree potential and delayed to larger coupling constant. For both AF and F instabilities, $n_z(k)$ is peaked at small k where the $\hat{x}$-$\hat{y}$ pseudospin-plane exchange energies are most strongly frustrated by chirality, and the kinetic energy term which opposes pseudospin magnetism is weakest.

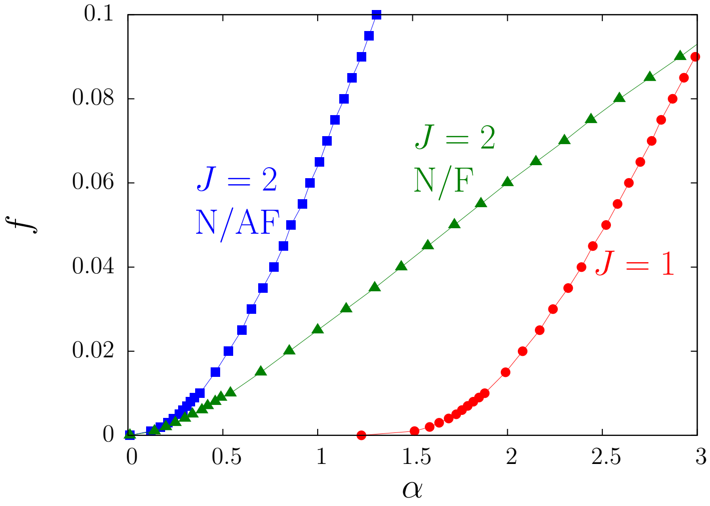

Figure 5.3: Phase diagram of C2DES's with $J = 2$ and $J = 1$. For the $J = 2$ bilayer case we have taken $\bar{d} = 0.2$. Pseudospin magnetism occurs at strong coupling α and weak doping f. ($1 + f = n_\uparrow + n_\downarrow$ where the pseudospin density $n_\sigma = \sum_{\boldsymbol{k},i} \langle \hat{c}^\dagger_{\boldsymbol{k},i,\sigma} \hat{c}_{\boldsymbol{k},i,\sigma} \rangle / \mathcal{N}$ and $\mathcal{N} = \sum_{\boldsymbol{k},i} 1$.) In the $J = 2$ bilayer case, the Hartree potential favors smaller total polarization so that the initial normal (N) state instability (blue separatrix) is to antiferromagnetic (AF) states in which the pseudospin polarizations of different valley and spin components cancel. At larger α, the normal state is unstable (green separatrix) to ferromagnetic (F) pseudospin states. In the $J = 1$ monolayer case $\bar{d} = 0$ so the phase boundaries (red separatrix) of F and AF broken-symmetry states coincide.

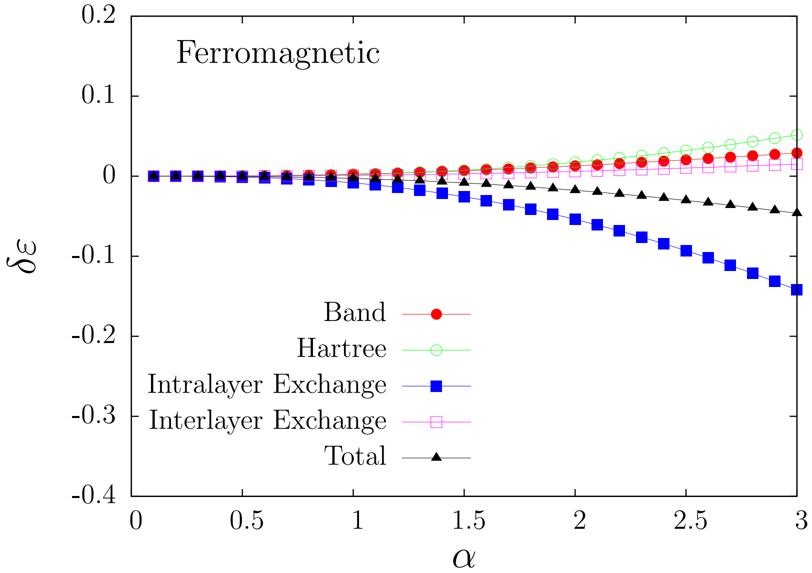

Figure 5.4: Condensation energy per electron $\delta\varepsilon$ [in units of $\varepsilon_0(k_\mathrm{c})$] as a function of α for an undoped ($f = 0$) $J = 2$ C2DES for both ferro state.

The physics that drives pseudospin magnetism in graphene bilayers is illustrated in Fig. 5.4 and Fig. 5.5 which partitions the condensation energy into band, Hartree, intralayer exchange, and interlayer exchange contributions. Spontaneous layer polarization lowers the intralayer interaction energy at a cost in all other components. The overall energy change is negative, and the broken symmetry state occurs, because the interlayer exchange energy of the normal state is weakened by the band-Hamiltonian induced frustration explained earlier. The cost in interlayer exchange energy of pseudospin rotation is therefore much smaller than the gain in intralayer exchange energy and the overall energy is reduced. The energy gain is considerably larger for AF

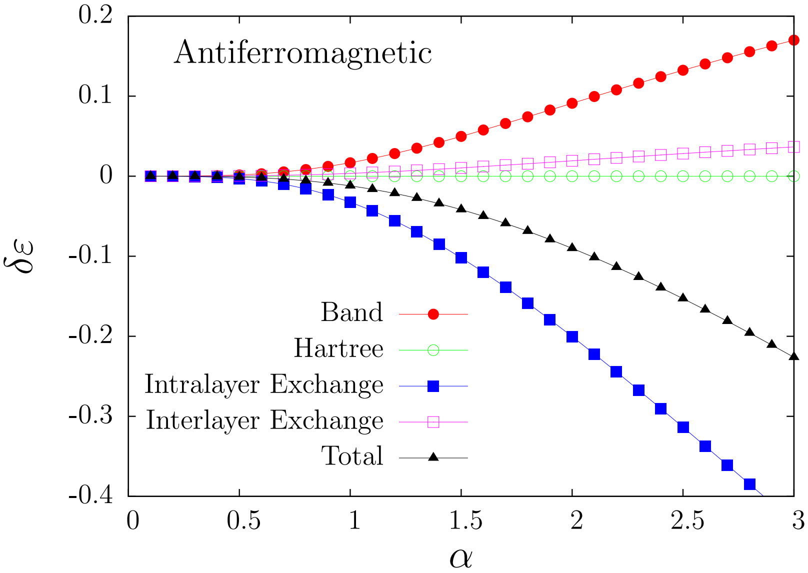

Figure 5.5: Condensation energy per electron $\delta\varepsilon$ [in units of $\varepsilon_0(k_c)$] as a function of α for an undoped $(f = 0)$ $J = 2$ C2DES for antiferro state.

broken symmetry states.

In Fig. 5.6 we illustrate typical results for the pseudospin (layer) polarization $\zeta = (n_\uparrow - n_\downarrow)/(n_\uparrow + n_\downarrow)$ of a graphene bilayer as a function of gate voltage $\bar{V}_g$. The AF ground state at $\bar{V}_g = 0$, which has $[Z_2 \times SU(4)]/[SU(2) \times SU(2)]$ broken symmetry because of the freedom to choose any two spin or pseudospin components for (say) positive polarization, is gradually polarized by the gate voltage, but eventually becomes unstable in favor of polarizing more layers in the sense preferred by the gate voltage. At sufficiently strong gate voltages, the F ground state in which all layers are polarized in the same sense becomes the ground state. As the gate voltage is varied local minima of the

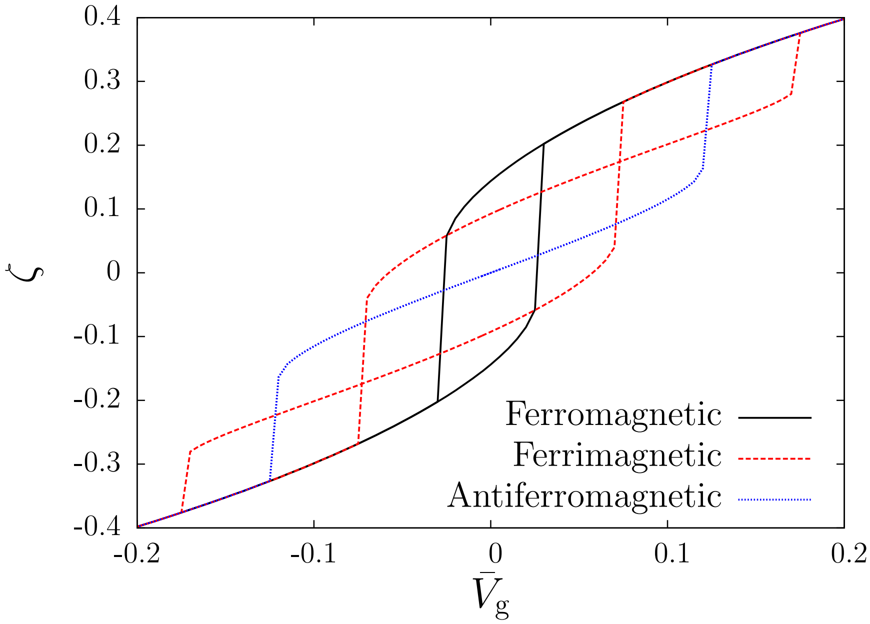

Figure 5.6: Metastable configurations of the pseudospin ferromagnet as a function of bias voltage V_{g} [in units of $\varepsilon_0(k_{\mathrm{c}})$] with $\alpha = 1$ and $f = 0$. We find self-consistent solutions of the gap equations (5.7)-(5.8) in which the pseudospin polarization has the same sense in all four components (ferromagnetic), in three of the four components (ferrimagnetic), or in half of the four components (antiferromagnetic).

Hartree-Fock energy functional become saddle points which are in the basin of attraction of another local minima. In this way, the self-consistent solutions exhibit hysteretic behavior.

5.4 Discussion

The proposals made here are based on approximate calculations and must ultimately be confirmed by experiment. Indeed, it is well known that

Hartree-Fock theory (HFT) often overestimates the tendency toward broken symmetry states. For example HFT predicts that a non-chiral 2DES is a (real-spin) ferromagnet at moderate coupling strengths, whereas experiments and accurate quantum Monte Carlo calculations suggest that ferromagnetism occurs only at a quite large value of the coupling constant [50]. Nilsson *et al.* [53] have recently claimed that a similar ferromagnetic instability occurs in weakly-doped graphene bilayers, presumably only at a much stronger coupling constant than implied by HFT. We believe that the momentum-space vortex instability identified here, which is unique to the peculiar band-structure of bilayer graphene, is qualitatively more robust than the real-spin ferromagnetic instability. This should be especially true in neutral bilayers since the momentum-space vortex instability occurs at a coupling constant ($\alpha \to 0$) for which correlation corrections to HFT are weak. This is not a strong-coupling instability like ferromagnetism, but much more akin to the very robust attractive-interaction weak-coupling instability which leads to superconductivity. The condensation energy per electron associated with the formation of a momentum-space vortex core is $\sim e^2 k_{\mathrm{c}}/\epsilon$, much larger than the $\sim e^2 k_{\mathrm{F}}/\epsilon$ condensation energy for the spin-polarized state. Because this broken symmetry state is most robust for uniform neutral bilayers, the smooth but strong disorder potentials responsible for inhomogeneity [54] in nearly neutral graphene sheets may need to be limited to allow this physics to emerge.

Finally, we note that graphene multilayers are described by a set of chiral system, and ABC stacked N-layer graphene has the largest chirality

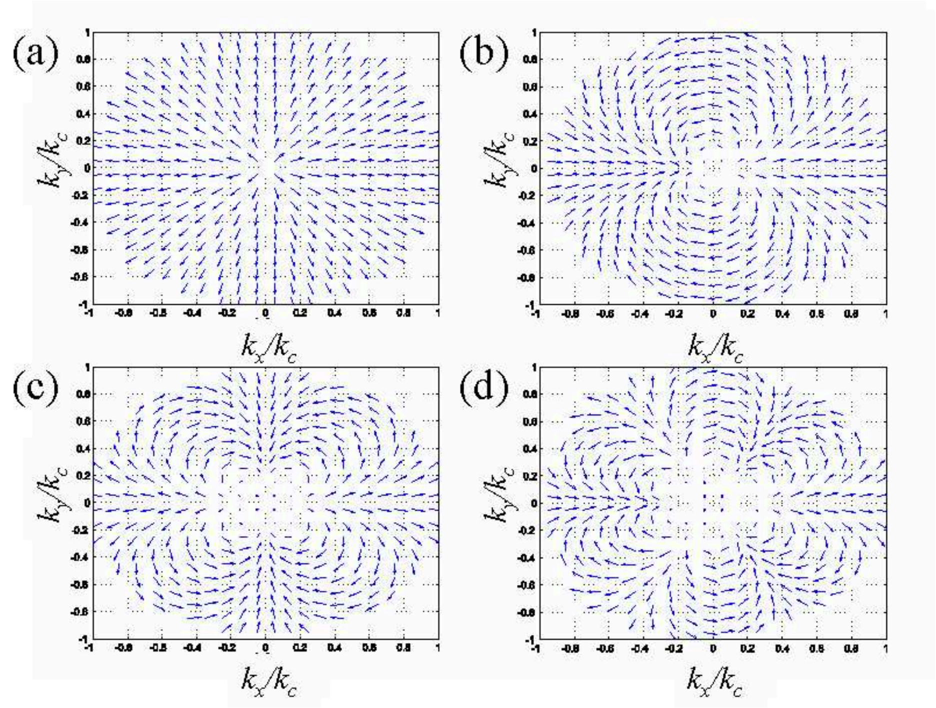

Figure 5.7: In-plane projected pseudospin orientation of (a) $J = 1$, (b) $J = 2$, (c) $J = 3$ and (d) $J = 4$ chiral two-dimensional electron systems for $V_{\rm g} = 0$, $\alpha = 1$ and $f = 0$. For $J > 1$, the arrows are shorter near the core of the momentum space vortex because the pseudospins near the core have rotated spontaneously toward $\hat{z}$ or $-\hat{z}$ direction indicating the pseudospin magnetic state.

N for the given number of layers, as discussed in Section 4.3. Figure 5.7 shows the momentum-space vortex structures for $J = 1, 2, 3, 4$ C2DESs, which correspond to $N = 1, 2, 3, 4$ ABC-stacked graphene multilayers. Thus ABC stacked graphene multilayers are the most likely candidate for the pseudospin magnetism.

Chapter 6

Exciton Condensation in Graphene Bilayers

In this chapter, we discuss about a possibility of exciton condensation in graphene bilayers. Because graphene is an atomically two-dimensional gapless semiconductor with nearly identical conduction and valence bands, graphene-based bilayers are attractive candidates for high-temperature electron-hole pair condensation. We present estimates which suggest that the Kosterlitz-Thouless temperatures of these two-dimensional counterflow superfluids can approach room temperature. [1]

6.1 Introduction

Electron-hole pair (exciton) condensates were first proposed [55, 56] as possible ordered states of solids more than forty years ago but have proved difficult to realize experimentally. Progress has been made recently with the discovery [57, 58] of equilibrium exciton condensation below $T \sim 1$K in the quantum Hall regime, the identification [59] of spontaneous coherence effects in cold optically excited exciton gases, and studies of dynamic condensation

---

[1] The contents of this chapter are based on the article: Hongki Min, Rafi Bistritzer, Jung-Jung Su, and A. H. MacDonald, *Room-temperature superfluidity in graphene bilayers?*, arXiv:0802.3462.

[60–62] of polaritons in non-resonantly pumped optical microcavities. In the weak-coupling limit, exciton condensation is a consequence of the Cooper instability [56] of solids with occupied conduction band states and empty valence band states inside identical Fermi surfaces. Bilayer exciton condensates are counterflow superfluids with unusual electrical properties [58, 63–67] which have so far been studied experimentally mainly in the quantum Hall regime. In this chapter, we point out that superfluidity is likely to persist to remarkably high temperatures in graphene based bilayers. Graphene is a particularly attractive candidate for room temperature bilayer exciton condensation because it is atomically two-dimensional, because it is a gapless semiconductor, and because its two-dimensional massless Dirac band structure implies nearly perfect particle-hole symmetry and stiff phase order.

We consider a system with two graphene layers embedded in a dielectric media and gated above and below as illustrated schematically in Fig. 6.1. Each layer has two Dirac-cone bands centered at inequivalent points in its Brillouin-zone. The top and bottom gates can be used to control the electric fields E_{ext} both above and below the bilayer. When the two fields are equal, the bilayer is neutral but charge is transferred from one layer to the other. The Fermi level lies in the graphene conduction band of one layer (the n-type layer) and in the valence band of the other layer (the p-type layer). The particle-hole symmetry of the Dirac equation ensures perfect nesting [2] between the electron

---

[2] The nesting condition requires only that the Fermi surfaces be identical in area and shape and not that the two layers have aligned honeycomb lattices and hence aligned Brillouin-

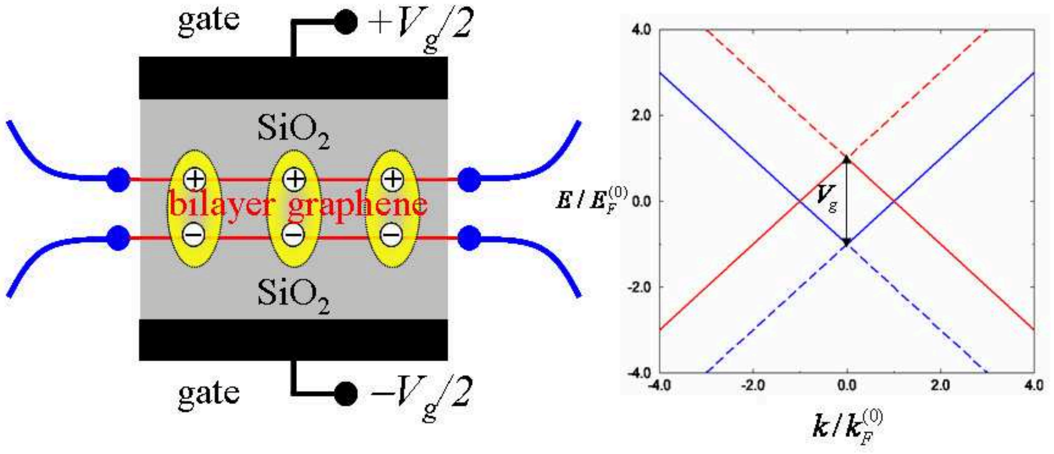

Figure 6.1: Left: Schematic illustration of a graphene bilayer exciton condensate channel in which two single-layer graphene sheets are separated by a dielectric (SiO_2 in this illustration) barrier. We predict that electron and hole carriers induced by external gates will form a high-temperature exciton condensate. Right: The two band model in which the two remote bands indicated by dashed lines are neglected.

Fermi spheres in the n-type layer and its hole counterparts in the opposite layer, thereby driving the Cooper instability. The condensed state establishes spontaneous long-range coherence between the two graphene layers.

Our main interest here is in providing an estimate of the maximum possible Kosterlitz-Thouless (KT) temperature T_{KT} of these two-dimensional

---

zones. Global wavevector mismatches can be removed by gauge transformations. When weak inter-valley electron-electron scattering processes are included, only simultaneous momentum shifts of both valleys in a layer are allowed. In this case, relative rotations of the two layers will have a small influence on details of the paired state. Relative rotations will also help to reduce the amplitude of bare interlayer tunneling process which weaken transport anomalies as discussed in Ref. [67]. For misaligned layers, bare tunneling could possibly be weak enough to produce interesting transport anomalies even for vertical transport between epilayers similar to those discussed in Ref. [36].

counterflow superfluids [58]. We use a two band model [3] in which the occupied valence band of the n-type layer and the empty conduction band of the p-type layer are neglected. Our T_{KT} estimate is constructed from mean-field (Hartree-Fock) theory calculations [4] of the temperature dependent phase stiffness of the ordered state.

Our main result is the normal to superfluid phase boundary depicted in Fig. 6.2. The KT temperature is plotted as a function of the separation between the layers d and the electric field E_{ext} outside the bilayer. We estimate that superfluidity can survive at room temperature under favorable experimental conditions. The non-monotonic dependence of T_{KT} on d at fixed E_{ext} follows from a competition between the increasing carrier density and the decreasing strength of interlayer electron-hole interactions with increasing d. At small d the phase stiffness is limited by the carrier concentration, which increases with d. At large d, the KT temperature is limited by the same fermion-entropy effects which are responsible for the Bardeen-Cooper-Schrieffer (BCS) critical temperature of weak-coupling superconductors.

---

[3] In separate calculations not described here, we found that coherence between the two remote bands has little effect for $k_{\mathrm{F}}d > 1$ and that will act to raise the KT temperature for $k_{\mathrm{F}}d < 1$.

[4] In parabolic band systems, this procedure provides a good estimate of the critical temperature in both the weak-coupling BCS and the strong-coupling BEC limits. Note however that because graphene is a gapless semiconductor, it does not have a simple BEC strong-coupling limit.

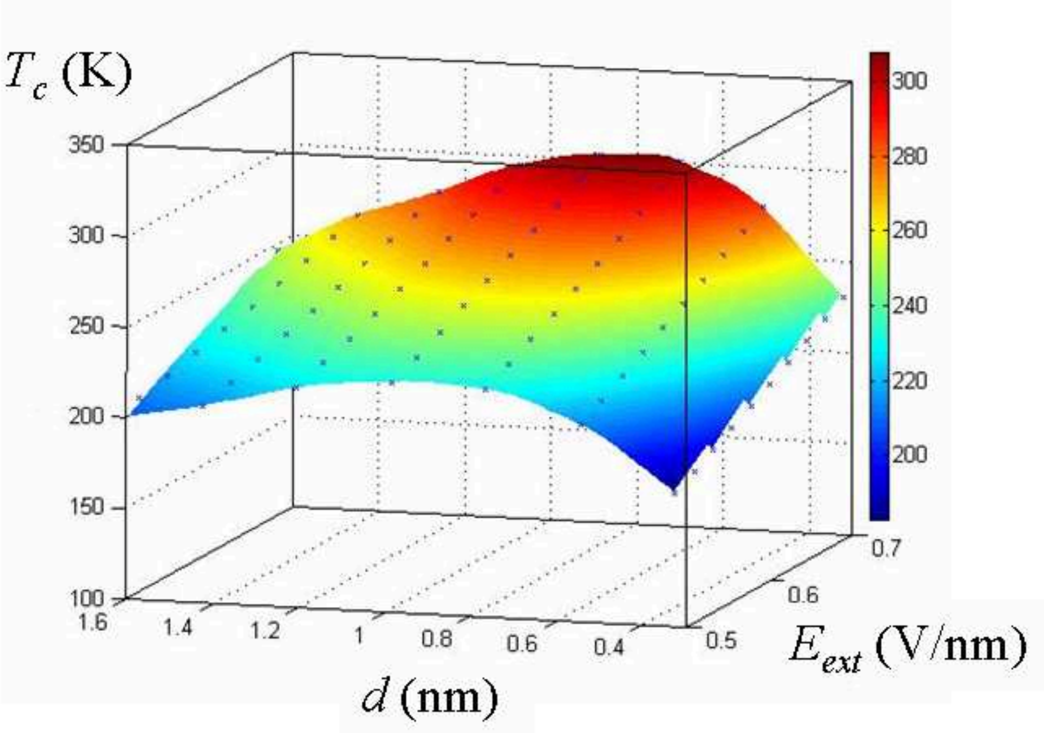

Figure 6.2: Normal to superfluid phase diagram showing the dependence of the critical temperature T_c in Kelvin on the distance between layers d in nm and external bias electric field E_{ext} in V/nm.

6.2 Two-band mean-field theory

In the band eigenstate representation our band-Hamiltonian is

$$\mathcal{H}_{\rm band} = -\sum_{\boldsymbol{k},\sigma',\sigma} c^{\dagger}_{\boldsymbol{k},\sigma'}\varepsilon_k \tau^z_{\sigma'\sigma} c_{\boldsymbol{k},\sigma}, \tag{6.1}$$

where $\varepsilon_k = V_g/2 - \hbar v k$, v is the band quasiparticle velocity, $\boldsymbol{\tau}$ is a Pauli matrix vector which acts on the *which layer* pseudospin, and $V_g = eE_{ext}d$ is the gate induced potential difference between the two layers.

Spontaneous interlayer coherence is induced by interlayer Coulomb interactions. In the mean-field description the interlayer interaction reorganizes the low-energy fermionic degrees of freedom into quasiparticles which are phase coherent linear-combinations of the single-layer states. The mean-field theory Hamiltonian can be written in the following form [68]:

$$\mathcal{H}_{\mathrm{MF}} = -\sum_{\boldsymbol{k},\sigma',\sigma} c^{\dagger}_{\boldsymbol{k},\sigma'} \left[\Delta^0_{\boldsymbol{k}} \delta_{\sigma',\sigma} + \boldsymbol{\Delta}_{\boldsymbol{k}} \cdot \boldsymbol{\tau}_{\sigma',\sigma}\right] c_{\boldsymbol{k},\sigma}. \tag{6.2}$$

Because of the model's particle-hole symmetry Δ^0 vanishes. The pseudospin effective field $\boldsymbol{\Delta}_{\boldsymbol{k}}$ in Eq. (6.2) solves the following self-consistent equation:

$$\begin{aligned} \Delta^z_{\boldsymbol{k}} &= \varepsilon_k + \frac{1}{A}\sum_{\boldsymbol{k'}} \left[V^{(\mathrm{S})}_{\boldsymbol{k},\boldsymbol{p}} - \frac{2\pi e^2}{\epsilon} g d\right] \frac{1}{2}\left[1 + f_{diff}(\Delta_{\boldsymbol{k'}}) n_z(\boldsymbol{\Delta}_{\boldsymbol{k'}})\right], \\ \boldsymbol{\Delta}^{\perp}_{\boldsymbol{k}} &= \frac{1}{A}\sum_{\boldsymbol{k'}} V^{(\mathrm{D})}_{\boldsymbol{k},\boldsymbol{k'}} \frac{1}{2} f_{diff}(\Delta_{\boldsymbol{k'}}) \boldsymbol{n}^{\perp}(\boldsymbol{\Delta}_{\boldsymbol{k'}}), \end{aligned} \tag{6.3}$$

where A is the area of a graphene layer, $\boldsymbol{\Delta}^{\perp}_{\boldsymbol{k}} = (\Delta^x_{\boldsymbol{k}}, \Delta^y_{\boldsymbol{k}})$, $\boldsymbol{n}$ is a unit vector parallel to $\boldsymbol{\Delta}_{\boldsymbol{k}}$, $g = 4$ accounts for the spin and valley degeneracy, and $f_{diff}(x) = \tanh(x/2k_{\mathrm{B}}T)$ is the difference between the occupation numbers of the negative energy and positive energy quasiparticles. The Coulomb matrix element of the intralayer interactions in the eigenstate basis is

$$V^{(\mathrm{S})}_{\boldsymbol{k},\boldsymbol{k'}} = \frac{1}{\epsilon}\frac{2\pi e^2}{|\boldsymbol{k}-\boldsymbol{k}'|}\frac{1+\cos(\phi_{\boldsymbol{k}} - \phi_{\boldsymbol{k'}})}{2} \tag{6.4}$$

where ϵ is the dielectric constant characterizing the embedding media, and $\phi_{\boldsymbol{k}} = \tan^{-1}(k_y/k_x)$. The corresponding matrix element of the interlayer interaction is $V^{(\mathrm{D})}_{\boldsymbol{k},\boldsymbol{k'}} = V^{(\mathrm{S})}_{\boldsymbol{k},\boldsymbol{k'}} \exp(-|\boldsymbol{k} - \boldsymbol{k'}|d)$. All energies are measured relative to the Dirac-point chemical potential of the balanced bilayer. [5] Note that each spin and valley pairs independently and that electron-hole condensation is indifferent to spin-valley space rotation in either layer.

The interaction strength in a graphene monolayer is usually characterized by the dimensionless effective fine structure constant,

$$\alpha = \frac{e^2 k_{\mathrm{F}}^{(0)}/\epsilon}{\hbar v k_{\mathrm{F}}^{(0)}} = \frac{1}{\epsilon} \cdot \frac{e^2}{\hbar v}. \tag{6.5}$$

This constant naturally appears in Eq. (6.3) if energies and momentum are expressed in units of $\hbar v k_{\mathrm{F}}^{(0)}$ and $k_{\mathrm{F}}^{(0)}$ respectively. Here $\hbar v k_{\mathrm{F}}^{(0)} = V_g/2$ is the band Hamiltonian Fermi momentum. The strength of the interlayer interaction is determined by α and by $k_{\mathrm{F}}^{(0)} d$.

Interestingly, the self-consistent equations (6.3) admit solutions with non-zero chirality J of the gap function $\mathbf{\Delta}^{\perp}$: $\mathbf{\Delta}_{\boldsymbol{k}}^{\perp} = \Delta_{k}^{\perp}\left(\cos(J\phi_{\boldsymbol{k}}), \sin(J\phi_{\boldsymbol{k}})\right)$. However, the critical temperature of a state with non-zero chirality is higher than that of the corresponding T_c of the zero chirality ground state so these solutions are unlikely to be physically relevant. We focus on the $J = 0$ solutions hereafter.

In the normal state, there is no interlayer coherence so $\mathbf{\Delta}^{\perp}$ vanishes. The intralayer Hartree-Fock potential then follows from self-consistent solution for Δ^{z}. The main effects of electron-electron interactions in this case are to increase the bare quasi-particle velocity [69] and to screen the external

---

[5] The unit contribution to the right-most square-bracket factor in Eq. (6.3) for $\Delta_{\boldsymbol{k}}^{z}$ is due to exchange interactions with the full valence band of the n-type layer.

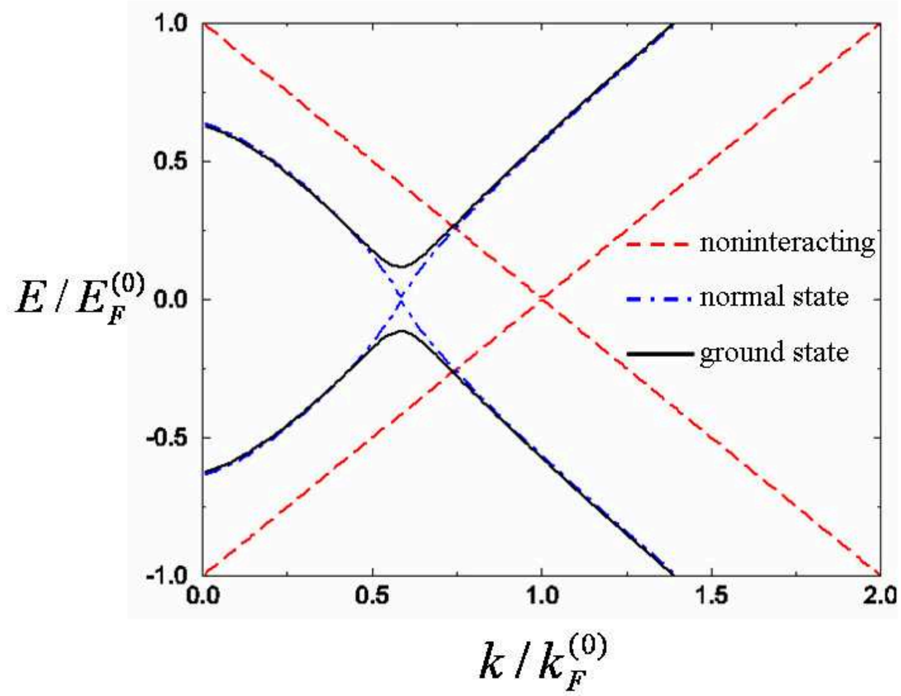

Figure 6.3: Mean-field theory energy bands for $\alpha = 1$, $T = 0$ and $k_{\mathrm{F}}^{(0)} d = 1$. ($E_{\mathrm{F}}^{(0)} = \hbar v k_{\mathrm{F}}^{(0)} = V_g/2$.) Note that $k_{\mathrm{F}} < k_{\mathrm{F}}^{(0)}$ because E_{ext} is screened.

bias voltage. Screening reduces the amount of charge transfer and therefore reduces the normal state Fermi momentum. As illustrated in Fig. 6.3 the energy bands change qualitatively in the condensed state because interlayer interactions induce coherence between the two layers and open an energy gap.

6.3 Linearized gap equation

The mean-field theory phase boundary between the normal phase and superfluid phase is obtained by solving the linearized gap equation

$$\boldsymbol{n}^{\perp}(\boldsymbol{\Delta}_{\boldsymbol{k}}) = \frac{1}{A}\sum_{\boldsymbol{k'}} M_{\boldsymbol{k},\boldsymbol{k'}}\ \boldsymbol{n}^{\perp}(\boldsymbol{\Delta}_{\boldsymbol{k'}}) \tag{6.6}$$

obtained by linearizing Eq. (6.3) with respect to $\boldsymbol{\Delta}^{\perp}$. The kernel

$$M_{\boldsymbol{k},\boldsymbol{k'}} = \frac{V^{(\mathrm{D})}_{\boldsymbol{k},\boldsymbol{k'}}}{\Delta^{z}_{\boldsymbol{k}}} \frac{f_d(\Delta^{z}_{\boldsymbol{k'}})}{2} \tag{6.7}$$

of the linearized gap equation is obtained by solving the self-consistent equation for Δ^z in the normal phase. The normal phase is stable provided that all the eigenvalues of M are smaller than one. By numerically evaluating M for various interlayer distances and external fields, we find the mean-field phase diagram $T_c^{\mathrm{MF}}(d, E_{ext})$, as illustrated in Fig. 6.4.

6.4 Phase stiffness

In two-dimensional superfluids the critical temperature is often substantially overestimated by mean-field theory and is ultimately limited by entropically driven vortex and antivortex proliferation at the KT temperature

$$k_{\mathrm{B}} T_{\mathrm{KT}} = \frac{\pi}{2}\rho_s(T_{\mathrm{KT}}). \tag{6.8}$$

We estimate T_{KT} by using mean-field theory to calculate the phase stiffness (superfluid density) $\rho_s(T)$. In parabolic band systems, this procedure yields reasonable estimates of T_{KT} in both BCS and BEC limits.

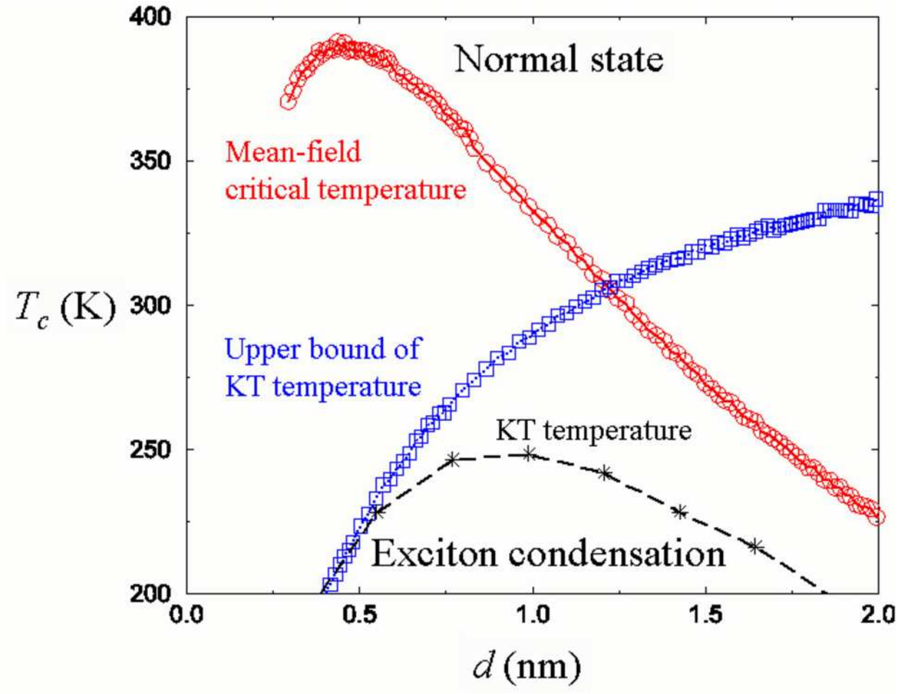

Figure 6.4: Mean-field critical temperature (red solid line with circles), upper bound of KT temperature (blue dotted line with squares), KT temperature temperature (black dashed line with stars) in Kelvin as a function of interlayer separation d in nm for an external bias electric field $E_{ext} = 0.5$ V/nm.

The phase stiffness is most easily calculated by evaluating the counterflow current $\boldsymbol{j_Q} = (e/\hbar)\rho_s \boldsymbol{Q}$ at small exciton momentum $\boldsymbol{Q}$. Put formally, we evaluate the expectation value of the counterflow current operator

$$j^{\mathrm{D}}_{\boldsymbol{Q}} = -\frac{ev}{A}\sum_{\boldsymbol{k}\sigma} \cos\phi_{\boldsymbol{k}} \langle c^{\dagger}_{\boldsymbol{k},\sigma} c_{\boldsymbol{k},\sigma}\rangle \tag{6.9}$$

with the density matrix defined by the mean-field Hamiltonian

$$\mathcal{H}_{\mathrm{MF}} = \mathcal{H}_{\mathrm{band}} + \sum_{\boldsymbol{k}} \left(\Delta^{\perp}_{\boldsymbol{kQ}} c^{\dagger}_{\boldsymbol{k+Q/2},\uparrow} c_{\boldsymbol{k-Q/2},\downarrow} + h.c. \right), \tag{6.10}$$

where $\Delta^{\perp}_{\boldsymbol{k}\boldsymbol{Q}}$ is the finite momenta pairing potential.

Placing $\boldsymbol{Q}$ along $\hat{\boldsymbol{x}}$, we find that $\Delta^0_{\boldsymbol{k}} \rightarrow \frac{1}{2}\hbar Q v \cos\phi_k$ and that

$$j^{\mathrm{D}}_{\boldsymbol{Q}} = \frac{evQ}{4\pi} \int dk \left[\hbar v k \frac{\partial f(\Delta_k)}{\partial \Delta_k} - \frac{1}{2} f_d\left(\Delta_k\right) \hat{n}_z\left(\Delta_k\right) \right], \tag{6.11}$$

where $\Delta^z_k = \epsilon_k$. This expression for $j^{\mathrm{D}}_{\boldsymbol{Q}}$ has an ultraviolet divergence and fails to vanish in the normal state ($\Delta^{\perp} \rightarrow 0$). Both properties are pathologies of the Dirac model. When the two Fermi circles are shifted in opposite directions at finite Q, they are asymmetric with respect to the momentum-space origin. As a consequence, an ultraviolet cutoff at some momentum magnitude yields a finite counterflow current. This current would vanish if the same calculation was performed using a microscopic model with integrations over the full Brillouin-zone. As long as $\Delta^{\perp}$ is small compared to graphene's π-band width, a condition that is very easily satisfied, the anomalous ultraviolet contribution to $\rho_s(T)$ is identical in the normal and in the condensed states. It follows that the physical counterflow current is related to the Dirac model counterflow current (j^{D}) by $j_{\boldsymbol{Q}} = j^{\mathrm{D}}_{\boldsymbol{Q}}(\Delta) - j^{\mathrm{D}}_{\boldsymbol{Q}}(\Delta^{\perp} = 0)$. Following this prescription, we conclude that the last term in Eq. (6.11) can be neglected and find that

$$\rho_s(T) \approx \frac{v^2\hbar^2}{16\pi k_{\mathrm{B}} T} \int k dk \left[\mathrm{sech}^2\left(\frac{\varepsilon_k}{2k_{\mathrm{B}}T}\right) - \mathrm{sech}^2\left(\frac{\Delta_k}{2k_{\mathrm{B}}T}\right) \right]. \tag{6.12}$$

Note that the zero temperature phase stiffness,

$$\rho_s(T=0) \approx \frac{E_F}{4\pi}, \tag{6.13}$$

is purely a normal state property just as in BCS theory. Indeed an identical result is obtained in the BCS theory of a parabolic band system when ρ_s is expressed in terms of the Fermi energy.

An alternative approach for estimating $\rho_s(T)$ which also accounts for the intralayer interactions is to evaluate the density matrix in Eq. (6.9) using the self-consistent mean-field equations with finite pairing momentum. As explained above, the physical counterflow current is obtained by subtracting $j^{\mathrm{D}}_{\boldsymbol{Q}}(\Delta^{\perp} = 0)$ from $j^{\mathrm{D}}_{\boldsymbol{Q}}$. Figure 6.4 shows a phase diagram obtained from the linearized gap equation and the KT temperature for an external bias electric field $E_{ext} = 0.5$ V/nm. The KT temperatures which follow from this procedure and Eq. (6.8) are depicted in Fig. 6.2. Since $\rho_s(T)$ is a decreasing function of d, it follows from Eqs.(6.8,6.13) that $k_{\mathrm{B}}T_{\mathrm{KT}} \leq E_{\mathrm{F}}/8$. In our calculations, we find that this inequality approaches an equality when $k_{\mathrm{F}}d$ is small. Consequently, the increase in T_{KT} with d at small d in Fig. 6.2 simply follows the increase in $E_{\mathrm{F}} \sim eE_{ext}d/2$.

6.5 Discussion

The high transition temperatures we predict deserve comment. They are larger than those of typical superconductors because condensation is driven by Coulomb interactions over the full band width, rather than by phonon-mediated interactions between quasiparticles in a narrow shell around the Fermi surface. In this sense exciton condensation is more akin to ferromagnetism, which is also driven by Coulomb interactions and can survive to very high temperatures. The temperatures at which exciton condensation can be achieved in graphene bilayers are immensely higher than those which might be possible in semiconductor bilayers because more carriers can be induced by external electric fields when the semiconductor has no gap, because the Fermi energy increases more rapidly with carrier density for Dirac bands than for parabolic bands, and because graphene layers are atomically thin - eliminating the layer thickness effects which substantially weaken Coulomb interaction in semiconductor quantum well bilayers. The numerical estimates reported in Fig. 6.2 were obtained using a coupling constant appropriate for a SiO_2 dielectric. The optimal dielectric for high exciton condensation temperatures should have a high dielectric breakdown field and a low dielectric constant, suggesting that a suitable wide-gap material is likely the optimal choice.

Screening and other beyond-mean-field induced-interaction effects are difficult to describe. In the case of weakly interacting atomic gases induced interaction effects can [70] either increase or decrease T_c, depending on the number of fermion flavors g. For the present Coulomb interaction case, a static Thomas-Fermi screening approximation with normal state screening wavevectors reduces interaction strengths very substantially when spin and valley degeneracies ($g = 4$) are included. Mean-field-theory critical temperatures are reduced by a factor of $\sim e^g$ at small d in this approximation and by a larger factor at large d. On the other hand, when the screening wavevectors are evaluated in the condensed state there is little influence on T_{KT} at small $k_F d$ both because the large gap weakens screening and because T_{KT} is proportional to the Fermi energy and not to the interaction strength in this limit. All these lead us to suspect that at low-temperatures there is a first-order phase transition as a function of layer separation d between condensed and electron-hole plasma states, similar to the transitions studied experimentally [71] in quantum Hall exciton condensates and theoretically [72] in parabolic band bilayers.

Because of spin and valley degrees of freedom, the exciton pairing we describe in this work is SU(4) symmetric; crudely speaking the system has four identical superfluids simultaneously. We therefore anticipate interesting consequences of slightly unequal electron and hole densities, similar to anticipated effects associated with the spin degree-of-freedom in normal exciton condensates [73, 74]. Because of this sensitivity, front and back gates which can control the electric fields on opposite sides of the bilayer independently are highly desirable in experimental searches for graphene bilayer exciton condensation.

Our finding that $k_{\mathrm{B}}T_{\mathrm{KT}} \sim 0.1E_F$ in the limit of strong interactions between conduction band electrons and valence band holes is partially supported by experimental studies [75] of fermionic cold atoms in the strong-interaction unitary limit. It implies that T_{KT} should approach room temperature when E_F is larger than ~ 0.3 eV (n larger than $\sim 10^{13}$ cm^{-2}) and d is smaller than ~ 2 nm. Experimental detection of spontaneous coherence through one of its characteristic transport anomalies [58] will be necessary to construct a quantitatively reliable phase diagram.

Chapter 7

Conclusion

The work in this thesis is motivated by the search for new collective ordered states which can be used in future electronic devices. Due to the collective behavior of many electrons, the thermal smearing of switching behavior can be significantly reduced. Switching can, in principle, occur for a change in the driving energy per electron which is $\sim k_BT/N$ where N is the number of electrons involved. In a single-electron device scheme, $N \sim 1$ so a gate voltage should be at least several times larger than the thermal smearing to distinguish between on and off states. In the collective-electron device scheme, however, N is, in principle, infinite thus even a very small gate voltage can be used. In principle, this should make it possible to design logic circuits which consume much less power.

First, let 's consider pseudospin magnetism in graphene systems. If only the fully polarized solutions existed, these results for pseudospin polarization as a function of gate voltage would be very much like the behavior expected for an easy-axis ferromagnet in an external magnetic field along the hard axis, as illustrated in Fig. 7.1. In magnetic memories bistability enables information storage. In magnetic metal spintronics the dependence of

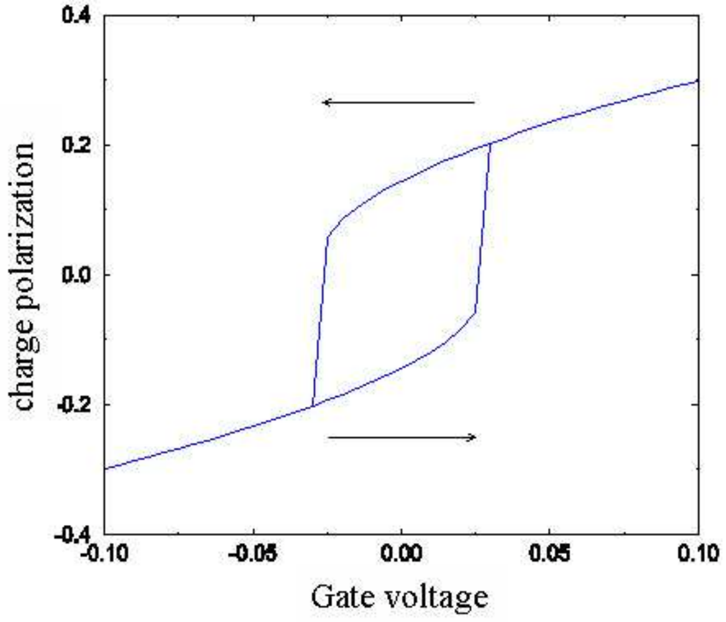

Figure 7.1: Pseudospin (charge) polarization $\zeta = (n_\uparrow - n_\downarrow)/(n_\uparrow + n_\downarrow)$ of a graphene bilayer as a function of gate voltage $\bar{V}_{\rm g}$ [in units of $\varepsilon_0(k_{\rm c})$] assuming fully polarized ferromagnetic states with $\alpha = 1$ and $f = 0$.

the resistance of a circuit containing magnetic elements on the magnetization orientation of those elements gives rise to sudden changes in resistance with field (giant magnetoresistance) which can be used to sense very small magnetic fields. Currents running through such a circuit can also be used to change the magnetic state through spin-transfer torques. Pseudospin ferromagnetism in graphene bilayers could potentially lead to very appealing electrical analogs of both of these effects. Because of the collective behavior of many electrons, the pseudospin ferromagnet can be switched between metastable states with gate voltages that are much smaller than the thermal energy $k_{\rm B}T$, potentially enabling electronics which is very similar to standard complementary metal-oxide-semiconductor but uses much less power. This possibility is analogous to the property that a magnetic element can be switched between magnetic states by Zeeman field changes that are extremely small compared to the thermal energy $k_{\mathrm{B}}T$. Pseudospin-transfer torques, which are expected to occur in electronic bilayer systems [76], can also be used to switch the pseudomagnetic state.

Similarly, excitonic superfluidity in graphene bilayers could be used for a future electronic device. If this graphene bilayer can be engineered to form an electron-hole pair condensate under high enough temperatures, it may be able to extend Moore's law for another decade. This would be possible because the superfluidity in graphene bilayers could enable dissipation-free interconnects and might enable transistors which could be operated with a gate voltage much smaller than the thermal energy $k_B T$ due to the collective behavior of many electrons, and therefore would use much less power.

Appendices

Appendix A

Tight-binding Model

A.1 Basic formulation

A Bloch wavefunction at a wavevector $\boldsymbol{k}$ is given by

$$|\psi_{\boldsymbol{k}}\rangle = \frac{1}{\sqrt{N}} \sum_{\boldsymbol{R}} e^{i\boldsymbol{k}\cdot\boldsymbol{r}} |w_{\boldsymbol{R}}\rangle \tag{A.1}$$

where $|w_{\boldsymbol{R}}\rangle$ is a Wannier function at a lattice point $\boldsymbol{R}$. In a tight-binding method, the Wannier function can be expanded in a small number of localized atomic orbitals:

$$|w_{\boldsymbol{R}}\rangle = \sum_{\boldsymbol{R}_b,\mu} c_{b,\mu} e^{i\boldsymbol{k}\cdot\boldsymbol{R}_b} |\phi_{\boldsymbol{R}_b-\boldsymbol{R},\mu}\rangle \tag{A.2}$$

where $\boldsymbol{R}_b$ is a position of basis atoms and μ is a set of additional quantum numbers such as an angular momentum quantum number.

The energy $E_{\boldsymbol{k}}$ is given by

$$E_{\boldsymbol{k}} = \frac{\langle\psi_{\boldsymbol{k}}| H |\psi_{\boldsymbol{k}}\rangle}{\langle\psi_{\boldsymbol{k}}\,|\psi_{\boldsymbol{k}}\rangle}. \tag{A.3}$$

Using the variational principle, we can obtain the following relation:

$$\sum_{l',\mu'} H_{\boldsymbol{R}_b,\mu;\boldsymbol{R}_{b'},\mu'}(\boldsymbol{k})\; c_{b',\mu'} = E_{\boldsymbol{k}} \sum_{l',\mu'} S_{\boldsymbol{R}_b,\mu;\boldsymbol{R}_{b'},\mu'}(\boldsymbol{k})\; c_{b',\mu'} \tag{A.4}$$

where

$$\begin{aligned} H_{\boldsymbol{R}_b,\mu;\boldsymbol{R}_{b'},\mu'}(\boldsymbol{k}) &= \sum_{\boldsymbol{\delta}} e^{i\boldsymbol{k}\cdot(\boldsymbol{\delta}+\boldsymbol{R}_{b'}-\boldsymbol{R}_b)} \left\langle \phi_{\boldsymbol{R}_b+\boldsymbol{\delta},\mu}\right| H \left|\phi_{\boldsymbol{R}_{b'},\mu'}\right\rangle , \\ S_{\boldsymbol{R}_b,\mu;\boldsymbol{R}_{b'},\mu'}(\boldsymbol{k}) &= \sum_{\boldsymbol{\delta}} e^{i\boldsymbol{k}\cdot(\boldsymbol{\delta}+\boldsymbol{R}_{b'}-\boldsymbol{R}_b)} \left\langle \phi_{\boldsymbol{R}_b+\boldsymbol{\delta},\mu} \middle|\phi_{\boldsymbol{R}_{b'},\mu'}\right\rangle , \end{aligned} \tag{A.5}$$

with $\boldsymbol{\delta}$ moving over lattice points.

Thus, the problem is reduced to the following generalized eigenvalue equation:

$$H(\boldsymbol{k})\,\boldsymbol{c} = E_{\boldsymbol{k}} S(\boldsymbol{k})\,\boldsymbol{c}. \tag{A.6}$$

This problem can be transformed to a usual eigenvalue problem using Löwdin symmetric orthogonalization procedure:

$$\begin{aligned} H' &= S^{-\frac{1}{2}} H S^{-\frac{1}{2}}, \\ \boldsymbol{c}' &= S^{\frac{1}{2}}\boldsymbol{c}. \end{aligned} \tag{A.7}$$

Note that the overlap matrix S is symmetric and positive definite, so it is always possible to decompose S as $S = S^{\frac{1}{2}}S^{\frac{1}{2}}$. Therefore, the generalized eigenvalue problem becomes a usual eigenvalue problem:

$$H'\boldsymbol{c}' = E\boldsymbol{c}'. \tag{A.8}$$

The Hamiltonian matrix elements $t_{\mu,\mu'}(\boldsymbol{\delta}) = \left\langle \phi_{\boldsymbol{R}_b+\boldsymbol{\delta},\mu}\right| H \left|\phi_{\boldsymbol{R}_{b'},\mu'}\right\rangle$ can be divided into one-,two-,and three center terms. The on-site hopping parameter $t_\mu \equiv t_{\mu,\mu}$ for μ orbital involves a one-center integral, whereas nearest neighbor hopping parameter $t_{\mu,\mu'}$ is, in general, a three-center matrix element which depends not only on the direction of two orbitals μ and μ', but also on other atoms surrounding them.

By considering only hopping between two atoms and neglecting effects from other atoms, we can obtain the approximate two-center form, called the Slater-Koster two-center approximation. For example, on-site and two-center matrix elements for s and p orbitals along $\boldsymbol{N} \equiv (n_x, n_y, n_z)$ are given by Tab. 2.1. Note that for angular momentum states $\mu = lm$ and $\mu' = l'm'$,

$$t_{\mu,\mu'}(\boldsymbol{N}) = t_{\mu',\mu}(-\boldsymbol{N}) = (-1)^{l+l'} t_{\mu',\mu}(\boldsymbol{N}). \tag{A.9}$$

This means that $t_{p_x,s} = -t_{s,p_x}$ and $t_{p_x,p_y} = t_{p_y,p_x}$, etc. The overlap matrix can be obtained by similar method.

A.2 Application to graphene

The Hamiltonian matrix at $\boldsymbol{k}$ between sublattices A and B in graphene is given by

$$H_{A,\mu;B,\mu'}(\boldsymbol{k}) = t_{\mu,\mu'}(\boldsymbol{N}_1) e^{i\frac{k_y a}{\sqrt{3}}} + e^{-i\frac{k_y a}{2\sqrt{3}}} \left[t_{\mu,\mu'}(\boldsymbol{N}_2) e^{-i\frac{k_x a}{2}} + t_{\mu,\mu'}(\boldsymbol{N}_3) e^{i\frac{k_x a}{2}} \right], \tag{A.10}$$

where $\boldsymbol{N}_1$,$\boldsymbol{N}_2$ and $\boldsymbol{N}_3$ are three nearest neighbor vectors in graphene given by

$$\boldsymbol{N}_1 = a\Big(0, \frac{1}{\sqrt{3}}\Big),\ \boldsymbol{N}_2 = a\Big(-\frac{1}{2}, -\frac{1}{2\sqrt{3}}\Big),\ \boldsymbol{N}_3 = a\Big(\frac{1}{2}, -\frac{1}{2\sqrt{3}}\Big). \tag{A.11}$$

Then Hamiltonian matrix elements at $\boldsymbol{k}$ are given as follows:

$$\begin{aligned}
H_{A,s;A,s}(\boldsymbol{k}) &= s \qquad\qquad (\text{A.12})\\
H_{A,p_i;A,p_j}(\boldsymbol{k}) &= p\delta_{l,l'}\\
H_{A,s;B,s}(\boldsymbol{k}) &= (ss\sigma)\left[e^{i\frac{k_y a}{\sqrt{3}}} + 2\cos\left(\frac{k_x a}{2}\right)e^{-i\frac{k_y a}{2\sqrt{3}}}\right]\\
H_{A,s;B,p_x}(\boldsymbol{k}) &= i\sqrt{3}(sp\sigma)\sin\left(\frac{k_x a}{2}\right)e^{-i\frac{k_y a}{2\sqrt{3}}}\\
H_{A,s;B,p_y}(\boldsymbol{k}) &= (sp\sigma)\left[e^{i\frac{k_y a}{\sqrt{3}}} - \cos\left(\frac{k_x a}{2}\right)e^{-i\frac{k_y a}{2\sqrt{3}}}\right]\\
H_{A,s;B,p_z}(\boldsymbol{k}) &= 0\\
H_{A,p_x;B,s}(\boldsymbol{k}) &= -H_{A,s;B,p_x}(\boldsymbol{k})\\
H_{A,p_x;B,p_x}(\boldsymbol{k}) &= (pp\pi)e^{i\frac{k_y a}{\sqrt{3}}} + 2\cos\left(\frac{k_x a}{2}\right)e^{-i\frac{k_y a}{2\sqrt{3}}}\left[\frac{3}{4}(pp\sigma) + \frac{1}{4}(pp\pi)\right]\\
H_{A,p_x;B,p_y}(\boldsymbol{k}) &= -i\frac{\sqrt{3}}{2}\sin\left(\frac{k_x a}{2}\right)e^{-i\frac{k_y a}{2\sqrt{3}}}\left[(pp\sigma) - (pp\pi)\right]\\
H_{A,p_x;B,p_z}(\boldsymbol{k}) &= 0\\
H_{A,p_y;B,s}(\boldsymbol{k}) &= -H_{A,s;B,p_y}(\boldsymbol{k})\\
H_{A,p_y;B,p_x}(\boldsymbol{k}) &= H_{A,p_x;B,p_y}(\boldsymbol{k})\\
H_{A,p_y;B,p_y}(\boldsymbol{k}) &= (pp\sigma)e^{i\frac{k_y a}{\sqrt{3}}} + 2\cos\left(\frac{k_x a}{2}\right)e^{-i\frac{k_y a}{2\sqrt{3}}}\left[\frac{1}{4}(pp\sigma) + \frac{3}{4}(pp\pi)\right]\\
H_{A,p_y;B,p_z}(\boldsymbol{k}) &= 0\\
H_{A,p_z;B,s}(\boldsymbol{k}) &= H_{A,s;B,p_z}(\boldsymbol{k})\\
H_{A,p_z;B,p_x}(\boldsymbol{k}) &= H_{A,p_x;B,p_z}(\boldsymbol{k})\\
H_{A,p_z;B,p_y}(\boldsymbol{k}) &= H_{A,p_y;B,p_z}(\boldsymbol{k})\\
H_{A,p_z;B,p_z}(\boldsymbol{k}) &= (pp\pi)\left[e^{i\frac{k_y a}{\sqrt{3}}} + 2\cos\left(\frac{k_x a}{2}\right)e^{-i\frac{k_y a}{2\sqrt{3}}}\right]
\end{aligned}$$

Other elements can be obtained from the fact that a Hamiltonian is hermitian.

Appendix B

Ab initio Electronic Structure Calculation

In this chapter, we briefly summarize density function theory and pseudopotential theory as approximations of electron-electron interactions and electron-ion interactions, respectively. [1]

B.1 Density functional theory

B.1.1 Hohenberg-Kohn theorem

The density functional theory is based on the *Hohenberg-Kohn theorem*, which states that the external potential $v_{ext}(\boldsymbol{x})$ from the nuclei is determined by the ground state density $n_g(\boldsymbol{x})$ that minimizes the total energy. Let's consider a Hamiltonian $H = T + V_{ee} + V_{ext}$ with the expectation value $\langle V_{ext} \rangle = \int d\boldsymbol{x} v_{ext}(\boldsymbol{x}) n_g(\boldsymbol{x})$. Since $n_g(\boldsymbol{x})$ determines the external potential and the number of electrons, it follows that $n_g(\boldsymbol{x})$ determines the Hamiltonian thus all the electronic properties of the system.

From the Hohenberg-Kohn theorem, the total ground state energy is

---

[1] The contents of this chapter are based on Refs. [77, 78].

given by

$$\begin{aligned}E_g &= \min_\Psi \langle\Psi|T+V_{ee}+V_{ext}|\Psi\rangle \\ &= \min_n \left(\min_{\Psi\rightarrow n} \langle\Psi|T+V_{ee}+V_{ext}|\Psi\rangle\right) \\ &\equiv \min_n \left(T[n]+V_{ee}[n]+V_{ext}[n]\right), \qquad (B.1)\end{aligned}$$

where $\min_{\Psi\rightarrow n}$ means a minimization of wavefunctions Ψ with a fixed density n. Therefore, we can define the energy functional as

$$E[n] \equiv T[n]+V_{ee}[n]+V_{ext}[n]. \qquad (B.2)$$

Then the ground state energy is obtained by minimizing $E[n]$.

This is not merely a restatement of the Hohenberg-Kohn theorem but it clarifies the definition of the energy functional whose minimum gives the total ground state energy. Note that $T[n]+V_{ee}[n]$ is universal for any many-electron system whereas the external part $V_{ext}[n]$ is system-specific because it contains information on the nuclei and their position.

B.1.2 Kohn-Sham equations

First, let's consider a non-interacting reference system with an external potential $v_{ext}(\boldsymbol{x})$ in which there is no electron-electron interaction term. For this system, there will be an exact ground-state wavefunction

$$\Psi_s = \frac{1}{\sqrt{N!}}\det[\phi_1...\phi_N], \qquad (B.3)$$

which gives a density $n(\boldsymbol{x})$ given by

$$n(\boldsymbol{x}) = \sum_i |\phi_i(\boldsymbol{x})|^2. \qquad (B.4)$$

Let's define the non-interacting kinetic energy functional $T_s[n]$ by

$$\begin{aligned} T_s[n] &= \langle \Psi_s | -\frac{\hbar^2}{2m}\nabla^2 |\Psi_s\rangle \\ &= \sum_i \langle \phi_i | -\frac{\hbar^2}{2m}\nabla^2 |\phi_i\rangle \, . \end{aligned} \tag{B.5}$$

Then the total energy functional $E[n]$ is of the following form

$$E[n] = T_s[n] + V_{ext}[n]. \tag{B.6}$$

By minimizing $E[n]$ with respect to ϕ_i^*, we can obtain the following one-electron equation,

$$\epsilon_i |\phi_i\rangle = \left(-\frac{\hbar^2}{2m}\nabla^2 + v_{ext}(\boldsymbol{x}) \right) |\phi_i\rangle \, . \tag{B.7}$$

Next, let's consider an interacting system. The Kohn-Sham approach is based on the assumption that similarly as Eq. (B.4), the particle density can be parametrized in terms of a set of single electron orbitals representing a *non-interacting* reference system. Then we can define a non-interacting kinetic energy functional as Eq. (B.5).

By rearranging terms to make the total energy functional $E[n]$ to be a form of Eq. (B.6), we can obtain

$$\begin{aligned} E[n] &= T[n] + V_{ee}[n] + V_{ext}[n] \qquad \text{(B.8)} \\ &= T_s[n] + V_H[n] + V_{ext}[n] + V_{xc}[n], \end{aligned}$$

where $V_H[n] = \frac{1}{2}\int d\boldsymbol{x}d\boldsymbol{x}' \frac{e^2 n(\boldsymbol{x}) n(\boldsymbol{x}')}{|\boldsymbol{x}-\boldsymbol{x}'|}$ is the Hartree energy which corresponds to the classical Coulomb integral, while $V_{xc}[n]$ is *exchange-correlation* energy functional defined by

$$V_{xc}[n] \equiv T[n] - T_s[n] + V_{ee}[n] - V_H[n]. \tag{B.9}$$

Therefore, similarly as Eq. (B.7), we can obtain the following one-electron equation,

$$\epsilon_i \left|\phi_i\right\rangle = \left(-\frac{\hbar^2}{2m}\nabla^2 + v_{eff}(\boldsymbol{x})\right)\left|\phi_i\right\rangle . \tag{B.10}$$

Here the effective potential $v_{eff}(\boldsymbol{x})$ is defined by

$$v_{eff}(\boldsymbol{x}) = v_{ext}(\boldsymbol{x}) + v_H(\boldsymbol{x}) + v_{xc}(\boldsymbol{x}), \tag{B.11}$$

where the Hartree term $v_H(\boldsymbol{x}) = \int d\boldsymbol{x}' \frac{e^2 n(\boldsymbol{x}')}{|\boldsymbol{x}-\boldsymbol{x}'|}$ and the *exchange-correlation potential* $v_{xc}(\boldsymbol{x})$ is formally given by $v_{xc}(\boldsymbol{x}) = \frac{\delta V_{xc}[n]}{\delta n(\boldsymbol{x})}$.

Now the effects of exchange and correlation are incorporated in *local* $v_{xc}(\boldsymbol{x})$ so that the equation becomes a one-electron equation. Eq. (B.10) and Eq. (B.11) are called *Kohn-Sham equations* and they represent a mapping of the interacting many-electron system onto a system of non-interacting electrons moving in an effective potential due to all the other electrons.

Note that the single particle wavefunctions $\left|\phi_i\right\rangle$ are not the wavefunctions of real electrons. They describe mathematical quasiparticles, without a direct physical meaning. Similarly eigenvalues ϵ_i are not energies needed to add or subtract electrons from the interacting many-body systems. Thus Kohn-Sham energy gap is not the true energy gap and the disagreement becomes problematic especially in an insulator.

The Kohn-Sham equations must be solved self-consistently so that the occupied electronic states generate a charge density that produces the electronic potential used to construct the Kohn-Sham equations. Thus, instead of solving a many-body Schrödinger equation, we solve single particle Kohn-Sham equations self-consistently:

$$n^{(1)}(\boldsymbol{x}) \rightarrow v_{eff}^{(1)}(\boldsymbol{x}) \rightarrow n^{(2)}(\boldsymbol{x}) \rightarrow v_{eff}^{(2)}(\boldsymbol{x}) \rightarrow \cdots . \tag{B.12}$$

B.1.3 Exchange-correlation energy

In principle, the Kohn-Sham equations are exact. The problem is that we do not know the exact form of the exchange-correlation energy functional $V_{xc}[n]$. If $V_{xc}[n]$ was known exactly, then taking the functional derivative with respect to the density would produce an exchange-correlation potential $v_{xc}(\boldsymbol{x})$ which includes the effects of exchange and correlation exactly.

The approximate form of the exchange-correlation potential $v_{xc}(\boldsymbol{x})$ can be obtained using *local density approximation* (LDA) where the exchange-correlation potential is assumed locally that of a homogeneous system. In LDA, $v_{xc}(\boldsymbol{x})$ is given by

$$v_{xc}(\boldsymbol{x}) = \frac{\delta V_{xc}}{\delta n} \approx -e^2 \left(\frac{3}{\pi} n(\boldsymbol{x}) \right)^{\frac{1}{3}} . \tag{B.13}$$

We can extend LDA formulation to spin-polarized systems, which is called the *local spin density approximation* (LSDA). In this case, the total energy is a functional of spin up and down electron densities. We can also improve the approximation of the exchange-correlation energy by including the effects of the spatial density variations. The resulting gradient corrections are called the *generalized gradient approximations* (GGA).

B.2 Pseudopotential theory

Density functional theory maps the interacting many-electron system to a non-interacting many-electron system in an effective potential. The remaining one-electron Kohn-Sham equation still poses substantial numerical difficulties. For example, near the atomic region, the kinetic energy of the electrons is large resulting in rapid oscillations of the wavefunction, thus a large number of plane waves are needed to expand the tightly bound core orbitals and to follow the rapid oscillations of the wavefunctions of the valence electrons in the core region.

It is well known that most physical properties of solids are dependent on the valence electrons to a much greater extent than on the core electrons. The *pseudopotential approximation* exploits this by replacing the strong ionic potential by a weaker pseudopotential which acts on the pseudowavefunctions rather that the true wavefunctions.

Let $\left|\psi_{\boldsymbol{k}}^{(v)}\right\rangle$ and $\left|\psi_{\boldsymbol{k}}^{(c)}\right\rangle$ be an exact valence and core wavefunction respectively. Within the core region, the valence wavefunction is oscillatory but outside the core region, it can be approximated as a nearly free electron wavefunction. Therefore the valence wavefunction $\left|\psi_{\boldsymbol{k}}^{(v)}\right\rangle$ can be expressed as

$$\left|\psi_{\boldsymbol{k}}^{(v)}\right\rangle = \left[1 - \sum_{c}\left|\psi_{\boldsymbol{k}}^{(c)}\right\rangle\left\langle\psi_{\boldsymbol{k}}^{(c)}\right|\right]\left|\phi_{\boldsymbol{k}}^{(ps)}\right\rangle, \tag{B.14}$$

where $\left|\phi_{\boldsymbol{k}}^{(ps)}\right\rangle$ is the planewave part of the valence wavefunction and called the *pseudowavefunction.* Note that the valence wavefunction is orthogonal to the core wavefunction, i.e., $\left\langle\psi_{\boldsymbol{k}}^{(c)}\middle|\,\psi_{\boldsymbol{k}}^{(v)}\right\rangle = 0$.

The exact valence wavefunction $\left|\psi_{\boldsymbol{k}}^{(v)}\right\rangle$ satisfies the Schrödinger equation with eigenvalue $\epsilon_{\boldsymbol{k}}^{(v)}$,

$$(H_0 + V)\left|\psi_{\boldsymbol{k}}^{(v)}\right\rangle = \epsilon_{\boldsymbol{k}}^{(v)}\left|\psi_{\boldsymbol{k}}^{(v)}\right\rangle. \tag{B.15}$$

Therefore we can rewrite Eq. (B.15) as an effective Schrödinger equation satisfied by the pseudowavefunction $\left|\phi_{\boldsymbol{k}}^{(ps)}\right\rangle$,

$$\left(H_0 + V^{(ps)}\right)\left|\phi_{\boldsymbol{k}}^{(ps)}\right\rangle = \epsilon_{\boldsymbol{k}}^{(v)}\left|\phi_{\boldsymbol{k}}^{(ps)}\right\rangle, \tag{B.16}$$

where

$$V^{(ps)} = V + \sum_{c}\left(\epsilon_{\boldsymbol{k}}^{(v)} - \epsilon_{\boldsymbol{k}}^{(c)}\right)\left|\psi_{\boldsymbol{k}}^{(c)}\right\rangle\left\langle\psi_{\boldsymbol{k}}^{(c)}\right|. \tag{B.17}$$

Thus the original solid is now replaced by pseudovalence electrons and pseudoion cores.

Note that the *pseudopotential* $V^{(ps)}$ is much less singular than the true potential V because of the cancellation due to the additional term in Eq. (B.17). It is possible that we can treat the pseudopotential as a weak perturbation and do nearly free electron calculations for $\left|\phi_{\boldsymbol{k}}^{(ps)}\right\rangle$. The fact that the pseudopotential is weaker than the true potential is crucial because it makes the solution of the Scrödinger equation much simpler by allowing expansion of the wavefunctions in a relatively small set of plane waves.

There turn out to be many ways other than Eq. (B.17) to define $V^{(ps)}$ such that $H_0 + V^{(ps)}$ has the same valence eigenvalues as the actual crystal Hamiltonian $H_0 + V$ and the corresponding pseudowavefunctions remain orthogonal to the core wavefunctions. With only these physical constraints, an infinite number of pseudopotentials can be generated and determination of auxiliary conditions needed to produce universal and efficient pseudopotentials has been the subject of much active work.

Appendix C

Hartree-Fock Theory

C.1 Many-body operators

C.1.1 One-body operators

A one-body operator $\hat{F}$ in the occupation number representation is given by

$$\hat{F} = \sum_{\lambda',\lambda} \langle \lambda' | F | \lambda \rangle c^{\dagger}_{\lambda'} c_{\lambda}. \tag{C.1}$$

In a homogeneous electron gas for states $\lambda = \{\boldsymbol{k}, \sigma\}$ and $\langle \boldsymbol{x} | \boldsymbol{k}, \sigma \rangle = \frac{1}{\sqrt{V}} e^{i\boldsymbol{k}\cdot\boldsymbol{x}}$, a matrix element of the one-body operator is given by

$$\langle \boldsymbol{k}'\sigma' | F | \boldsymbol{k}\sigma \rangle = \frac{1}{\Omega} F_{\sigma'\sigma}(\boldsymbol{k}' - \boldsymbol{k}), \tag{C.2}$$

where $F_{\sigma',\sigma}(\boldsymbol{q}) = \int d\boldsymbol{x} e^{-i\boldsymbol{q}\cdot\boldsymbol{x}} F_{\sigma',\sigma}(\boldsymbol{x})$ and Ω is a volume of space. Then Eq. (C.1) reduces to

$$\hat{F} = \frac{1}{\Omega} \sum_{\boldsymbol{k}',\boldsymbol{k}} \sum_{\sigma',\sigma} F_{\sigma'\sigma}(\boldsymbol{k}' - \boldsymbol{k}) c^{\dagger}_{\boldsymbol{k}',\sigma'} c_{\boldsymbol{k},\sigma}. \tag{C.3}$$

Note that σ can be a spin or pseudospin degrees freedom such as a top or bottom layer.

In a periodic system, we can use Bloch wavefunctions as a basis set instead of a plane wave basis, [1]

$$\psi_{\boldsymbol{k},\sigma}(\boldsymbol{x}) = \frac{1}{\sqrt{N}} \sum_{\boldsymbol{R}} e^{i\boldsymbol{k}\cdot(\boldsymbol{R}+\boldsymbol{\tau}_\sigma)} \phi_\sigma(\boldsymbol{x} - \boldsymbol{R} - \boldsymbol{\tau}_\sigma), \tag{C.4}$$

where ϕ_σ is an atomiclike orbital, $\boldsymbol{R}$ is a lattice vector, $\boldsymbol{\tau}_\sigma$ is the displacement of the sites in a unit cell with respect to the lattice vector, and N is the number of lattice sites. The matrix element of the one-body operator is given by

$$\langle \boldsymbol{k}'\sigma' | F | \boldsymbol{k}\sigma \rangle = \frac{1}{\Omega} \tilde{F}_{\sigma'\sigma}(\boldsymbol{k}', \boldsymbol{k}), \tag{C.5}$$

where

$$\tilde{F}_{\sigma'\sigma}(\boldsymbol{k}', \boldsymbol{k}) = \sum_{\boldsymbol{G}} F_{\sigma'\sigma}(\boldsymbol{k}' - \boldsymbol{k} + \boldsymbol{G}) S_{\sigma'\sigma}(\boldsymbol{k}', \boldsymbol{k}, \boldsymbol{G}) \tag{C.6}$$

and

$$S_{\sigma'\sigma}(\boldsymbol{k}', \boldsymbol{k}, \boldsymbol{G}) = \sum_{\Delta\boldsymbol{R}} e^{-i\boldsymbol{k}'\cdot\boldsymbol{\tau}_{\sigma'} + i\boldsymbol{k}\cdot(\Delta\boldsymbol{R}+\boldsymbol{\tau}_\sigma)} \int d\boldsymbol{x}\, e^{i(\boldsymbol{k}'-\boldsymbol{k}+\boldsymbol{G})\cdot\boldsymbol{x}} \phi^*_{\sigma'}(\boldsymbol{x}-\boldsymbol{\tau}_{\sigma'}) \phi_\sigma(\boldsymbol{x}-\Delta\boldsymbol{R}-\boldsymbol{\tau}_\sigma). \tag{C.7}$$

Then the one-body operator in Eq. (C.1) reduces to

$$\hat{F} = \frac{1}{\Omega} \sum_{\boldsymbol{k}',\boldsymbol{k}} \sum_{\sigma',\sigma} \tilde{F}_{\sigma'\sigma}(\boldsymbol{k}', \boldsymbol{k}) c^\dagger_{\boldsymbol{k}',\sigma'} c_{\boldsymbol{k},\sigma}. \tag{C.8}$$

As an application, let's consider a Hamiltonian in a periodic system with a reciprocal vector $\boldsymbol{G}$:

$$\hat{H} = \sum_{\boldsymbol{k}} \sum_{\sigma',\sigma} \varepsilon_{\sigma'\sigma}(\boldsymbol{k}) c^\dagger_{\boldsymbol{k},\sigma'} c_{\boldsymbol{k},\sigma}, \tag{C.9}$$

---

[1] Note that here a different gauge was chosen compared to Eq. (3.11) for mathematical convenience resulting in expressions slightly different from those in Sec. 3.

where

$$\begin{aligned}\varepsilon_{\sigma'\sigma}(\boldsymbol{k}) &= \frac{1}{\Omega}\sum_{\boldsymbol{G}} H_{\sigma'\sigma}(\boldsymbol{G}) S_{\sigma'\sigma}(\boldsymbol{k},\boldsymbol{k},\boldsymbol{G}) \\ &= \sum_{\Delta\boldsymbol{R}} e^{i\boldsymbol{k}\cdot(\Delta\boldsymbol{R}+\boldsymbol{\tau}_\sigma-\boldsymbol{\tau}_{\sigma'})} t_{\sigma',\sigma}(\Delta\boldsymbol{R}),\end{aligned} \tag{C.10}$$

and

$$t_{\sigma',\sigma}(\Delta\boldsymbol{R}) = \int d\boldsymbol{x}\,\phi^*_{\sigma'}(\boldsymbol{x}-\boldsymbol{\tau}_{\sigma'}) H_{\sigma'\sigma}(\boldsymbol{x}) \phi_\sigma(\boldsymbol{x}-\Delta\boldsymbol{R}-\boldsymbol{\tau}_\sigma). \tag{C.11}$$

Here a periodicity of $H_{\sigma'\sigma}(\boldsymbol{x}+\boldsymbol{R}) = H_{\sigma'\sigma}(\boldsymbol{x})$ is assumed. Note that $t_{\sigma',\sigma}(\Delta\boldsymbol{R})$ is a matrix element of a tight-binding Hamiltonian.

C.1.2 Two-body operators

A two-body operator $\hat{V}$ in the occupation number representation is given by

$$\begin{aligned}\hat{V} &= \frac{1}{2}\sum_{a\neq b}^{N} V_{ab} \\ &= \frac{1}{2}\sum_{\lambda_1',\lambda_2',\lambda_1,\lambda_2} \big\langle \lambda_1'\lambda_2' \big| V \big| \lambda_1\lambda_2 \big\rangle c^\dagger_{\lambda_1'} c^\dagger_{\lambda_2'} c_{\lambda_2} c_{\lambda_1},\end{aligned} \tag{C.12}$$

where $c^\dagger_\lambda$ and c_λ are creation and annihilation operators for a state λ.

Let's assume that the two-body interaction is both spin and pseudospin independent. In a homogeneous electron gas for states $\lambda = \{\boldsymbol{k}, \sigma\}$,

$$\big\langle \boldsymbol{k}_1'\sigma_1', \boldsymbol{k}_2'\sigma_2' \big| V \big| \boldsymbol{k}_1\sigma_1, \boldsymbol{k}_2\sigma_2 \big\rangle = \frac{1}{\Omega}\delta_{\sigma_1',\sigma_1}\delta_{\sigma_2',\sigma_2}\delta_{\boldsymbol{k}_1'-\boldsymbol{k}_1,\boldsymbol{k}_2-\boldsymbol{k}_2'} V_{\sigma_1,\sigma_2}(\boldsymbol{k}_1'-\boldsymbol{k}_1), \tag{C.13}$$

where $V_{\sigma_1,\sigma_2}(\boldsymbol{q})$ is a Fourier transform of $V_{\sigma_1,\sigma_2}(\boldsymbol{x})$. Thus Eq. (C.12) reduces to

$$\hat{V} = \frac{1}{2\Omega}\sum_{\boldsymbol{k}_1,\boldsymbol{k}_2,\boldsymbol{q}}\sum_{\sigma_1,\sigma_2} V_{\sigma_1,\sigma_2}(\boldsymbol{q}) c^\dagger_{\boldsymbol{k}_1+\boldsymbol{q},\sigma_1} c^\dagger_{\boldsymbol{k}_2-\boldsymbol{q},\sigma_2} c_{\boldsymbol{k}_2,\sigma_2} c_{\boldsymbol{k}_1,\sigma_1}. \tag{C.14}$$

Next, let's consider the two-body operator in a periodic system. To capture the main consequences of crystalline inhomogeneity, we assume that the Bloch states with crystal momentum $\boldsymbol{k}$ can be written as a linear combination of atomic orbitals. If we assume that the overlap of ϕ_σ-orbitals in Eq. (C.4) centered on different sites can be neglected, a matrix element of the two-body operator is given by

$$\begin{aligned} & \big\langle \boldsymbol{k}_1'\sigma', \boldsymbol{k}_2'\sigma' \big| V \big| \boldsymbol{k}_1\sigma_1, \boldsymbol{k}_2\sigma_2 \big\rangle \\ \approx\ & \delta_{\sigma_1',\sigma_1}\delta_{\sigma_2',\sigma_2}\frac{1}{N^2}\sum_{\boldsymbol{R}_1,\boldsymbol{R}_2}\int d\boldsymbol{x}_1 d\boldsymbol{x}_2 V_{\sigma_1,\sigma_2}(\boldsymbol{x}_1-\boldsymbol{x}_2) \\ \times\ & e^{-i(\boldsymbol{k}_1'-\boldsymbol{k}_1)(\boldsymbol{R}_1+\boldsymbol{\tau}_{\sigma_1})-i(\boldsymbol{k}_2'-\boldsymbol{k}_2)(\boldsymbol{R}_2+\boldsymbol{\tau}_{\sigma_2})}\big|\phi_{\sigma_1}(\boldsymbol{x})\big|^2\big|\phi_{\sigma_2}(\boldsymbol{x})\big|^2 \\ =\ & \frac{1}{\Omega}\delta_{\sigma_1',\sigma_1}\delta_{\sigma_2',\sigma_2}\delta_{\boldsymbol{k}_1'-\boldsymbol{k}_1,\boldsymbol{k}_2-\boldsymbol{k}_2'}\tilde{V}_{\sigma_1,\sigma_2}(\boldsymbol{k}_1'-\boldsymbol{k}_1), \end{aligned} \tag{C.15}$$

where

$$\tilde{V}_{\sigma,\sigma'}(\boldsymbol{q}) = \sum_{\boldsymbol{G}} V_{\sigma,\sigma'}(\boldsymbol{q}+\boldsymbol{G}) w_\sigma^*(\boldsymbol{q}+\boldsymbol{G}) w_{\sigma'}(\boldsymbol{q}+\boldsymbol{G}) e^{i\boldsymbol{G}\cdot(\boldsymbol{\tau}_{\sigma_1}-\boldsymbol{\tau}_{\sigma_2})}, \tag{C.16}$$

and $w_\sigma(\boldsymbol{q}) = \int d\boldsymbol{x} e^{-i\boldsymbol{q}\cdot\boldsymbol{x}}\big|\phi_\sigma(\boldsymbol{x})\big|^2$ is an atomic form factor.

Thus the two-body operator in Eq. (C.12) simplifies to

$$\hat{V} = \frac{1}{2\Omega}\sum_{\boldsymbol{k}_1,\boldsymbol{k}_2,\boldsymbol{q}}\sum_{\sigma_1,\sigma_2}\tilde{V}_{\sigma_1,\sigma_2}(\boldsymbol{q}) c^\dagger_{\boldsymbol{k}_1+\boldsymbol{q},\sigma_1} c^\dagger_{\boldsymbol{k}_2-\boldsymbol{q},\sigma_2} c_{\boldsymbol{k}_2,\sigma_2} c_{\boldsymbol{k}_1,\sigma_1}. \tag{C.17}$$

Note that the labels $\boldsymbol{k}_1$,$\boldsymbol{k}_2$ and $\boldsymbol{q}$ are restricted to the Brillouin zone .

C.2 Hartree-Fock theory

C.2.1 Hartree terms

A mean-field Hartree approximation of Eq. (C.12) is given by

$$\hat{V}^{(H)} = \sum_{\lambda} \varepsilon_{\lambda}^{(H)} c_{\lambda}^{\dagger} c_{\lambda} - \left\langle \hat{V}^{(H)} \right\rangle, \tag{C.18}$$

where

$$\begin{aligned} \varepsilon_{\lambda}^{(H)} &= \frac{1}{\Omega} \sum_{\lambda'} \left\langle \lambda\lambda' \middle| V \middle| \lambda\lambda' \right\rangle \rho_{\lambda',\lambda'}, \\ \left\langle \hat{V}^{(H)} \right\rangle &= \frac{1}{2} \sum_{\lambda} \varepsilon_{\lambda}^{(H)} \rho_{\lambda,\lambda}. \end{aligned} \tag{C.19}$$

Here the density matrix is introduced as

$$\rho_{\lambda',\lambda} \equiv \left\langle c_{\lambda}^{\dagger} c_{\lambda'} \right\rangle. \tag{C.20}$$

From now on, let's refer σ as a pseudospin and treat spin-degeneracy as g_s. In a homogeneous gas for states $\lambda = \{\boldsymbol{k}, \sigma\}$,

$$\hat{V}^{(H)} = \sum_{\boldsymbol{k},\sigma} \varepsilon_{\sigma}^{(H)} c_{\boldsymbol{k},\sigma}^{\dagger} c_{\boldsymbol{k},\sigma} - \left\langle \hat{V}^{(H)} \right\rangle, \tag{C.21}$$

where

$$\begin{aligned} \varepsilon_{\sigma}^{(H)} &= \frac{g_s}{\Omega} \sum_{\boldsymbol{k}',\sigma'} V_{\sigma,\sigma'}(0) \rho_{\sigma',\sigma'}(\boldsymbol{k}'), \\ \left\langle \hat{V}^{(H)} \right\rangle &= \frac{g_s}{2} \sum_{\boldsymbol{k},\sigma} \varepsilon_{\sigma}^{(H)} \rho_{\sigma,\sigma}(\boldsymbol{k}). \end{aligned} \tag{C.22}$$

Next, let's consider a periodic system. From Eq. (C.17) and Eq. (C.18), the mean-field Hartree approximation in a lattice is given by

$$\hat{V}^{(H)} = \sum_{\boldsymbol{k},\sigma} \varepsilon_{\sigma}^{(H)} c_{\boldsymbol{k},\sigma}^{\dagger} c_{\boldsymbol{k},\sigma} - \left\langle \hat{V}^{(H)} \right\rangle, \tag{C.23}$$

where

$$\varepsilon_{\sigma}^{(H)} = \frac{g_s}{\Omega} \sum_{\boldsymbol{k}',\sigma'} \tilde{V}_{\sigma,\sigma'}(0)\rho_{\sigma',\sigma'}(\boldsymbol{k}'). \tag{C.24}$$

C.2.2 Fock terms

A mean-field Fock approximation of Eq. (C.12) is given by

$$\hat{V}^{(F)} = \sum_{\lambda',\lambda} \varepsilon_{\lambda'\lambda}^{(F)} c_{\lambda'}^{\dagger} c_{\lambda} - \left\langle \hat{V}^{(F)} \right\rangle, \tag{C.25}$$

where

$$\begin{aligned} \varepsilon_{\lambda'\lambda}^{(F)} &= -\frac{1}{\Omega} \left\langle \lambda'\lambda \middle| V \middle| \lambda\lambda' \right\rangle \rho_{\lambda',\lambda}, \\ \left\langle \hat{V}^{(F)} \right\rangle &= \frac{1}{2} \sum_{\lambda',\lambda} \varepsilon_{\lambda'\lambda}^{(F)} \rho_{\lambda,\lambda'}. \end{aligned} \tag{C.26}$$

Let's consider interactions in a mean-field Fock approximation of Eq. (C.14):

$$\hat{V}^{(F)} = \sum_{\boldsymbol{k},\sigma',\sigma} \varepsilon_{\boldsymbol{k}\sigma'\sigma}^{(F)}(\boldsymbol{k}) c_{\boldsymbol{k},\sigma'}^{\dagger} c_{\boldsymbol{k},\sigma} - \left\langle \hat{V}^{(F)} \right\rangle, \tag{C.27}$$

where

$$\begin{aligned} \varepsilon_{\sigma'\sigma}^{(F)}(\boldsymbol{k}) &= -\frac{1}{\Omega} \sum_{\boldsymbol{k}'} V_{\sigma,\sigma'}(\boldsymbol{k}' - \boldsymbol{k}) \rho_{\sigma',\sigma}(\boldsymbol{k}'), \\ \left\langle \hat{V}^{(F)} \right\rangle &= \frac{g_s}{2} \sum_{\boldsymbol{k},\sigma',\sigma} \varepsilon_{\sigma'\sigma}^{(F)}(\boldsymbol{k}) \rho_{\sigma,\sigma'}(\boldsymbol{k}). \end{aligned} \tag{C.28}$$

Note that the spin-degeneracy factor g_s does not appear in $\varepsilon_{\sigma'\sigma}^{(F)}(\boldsymbol{k})$.

Next, let's consider a periodic system. From Eq. (C.17) and Eq. (C.25), the mean-field Fock approximation in a lattice is given by

$$\hat{V}^{(F)} = \sum_{\boldsymbol{k},\sigma',\sigma} \varepsilon_{\sigma'\sigma}^{(F)}(\boldsymbol{k}) c_{\boldsymbol{k},\sigma'}^{\dagger} c_{\boldsymbol{k},\sigma} - \left\langle \hat{V}^{(H)} \right\rangle, \tag{C.29}$$

where

$$\varepsilon^{(F)}_{\sigma'\sigma}(\boldsymbol{k}) = -\frac{1}{\Omega}\sum_{\boldsymbol{k}'} \tilde{V}_{\sigma,\sigma'}(\boldsymbol{k}'-\boldsymbol{k})\rho_{\sigma',\sigma}(\boldsymbol{k}'). \tag{C.30}$$

Note that the spin-degeneracy factor g_s does not appear in $\varepsilon^{(F)}_{\sigma'\sigma}(\boldsymbol{k})$.

C.2.3 Application to 2D electron gas with pseudospin

As an application, let's consider a 2D bilayer electron gas with a layer separation d and assume that the interaction matrix is given by

$$V_{\sigma\sigma'}(\boldsymbol{q}) = \begin{cases} \frac{2\pi e^2}{q} & (\sigma = \sigma') \\ \frac{2\pi e^2}{q}e^{-qd} & (\sigma \neq \sigma'), \end{cases} \tag{C.31}$$

where σ and σ' refer to layer degrees of freedom.

In general, Hartree-Fock interaction matrix elements can be expressed as

$$\hat{V}^{(HF)} = \sum_{\boldsymbol{k},\sigma} \varepsilon^{(HF)}_{\sigma'\sigma}(\boldsymbol{k}) c^{\dagger}_{\boldsymbol{k},\sigma'} c_{\boldsymbol{k},\sigma} \tag{C.32}$$

where $\varepsilon^{(HF)}_{\sigma'\sigma}(\boldsymbol{k}) = \varepsilon^{(H)}_{\sigma}\delta_{\sigma'\sigma} + \varepsilon^{(F)}_{\sigma'\sigma}(\boldsymbol{k})$. In the two-component pseudospin basis,

$$\boldsymbol{\varepsilon}^{(HF)}(\boldsymbol{k}) = -\big(B^0_{\boldsymbol{k}} + \boldsymbol{B}_{\boldsymbol{k}}\cdot\boldsymbol{\tau}\big), \tag{C.33}$$

where $\boldsymbol{\tau}$ is 2×2 Pauli matrices and

$$\begin{aligned} B^0_{\boldsymbol{k}} &= -\left[\bar{\varepsilon}^{(H)} + \bar{\varepsilon}^{(F)}(\boldsymbol{k})\right], \\ B^x_{\boldsymbol{k}} + iB^y_{\boldsymbol{k}} &= -\varepsilon^{(F)}_{bt}(\boldsymbol{k}), \\ B^z_{\boldsymbol{k}} &= -\frac{1}{2}\left[\Delta\varepsilon^{(H)} + \Delta\varepsilon(\boldsymbol{k})^{(F)}\right]. \end{aligned} \tag{C.34}$$

Here

$$\begin{aligned}
\bar{\varepsilon}^{(H)} &= \frac{1}{2}\left[\varepsilon_t^{(H)} + \varepsilon_b^{(H)}\right], \qquad\qquad \text{(C.35)} \\
\bar{\varepsilon}^{(F)}(\boldsymbol{k}) &= \frac{1}{2}\left[\varepsilon_t^{(F)}(\boldsymbol{k}) + \varepsilon_b^{(F)}(\boldsymbol{k})\right],
\end{aligned}$$

and

$$\begin{aligned}
\Delta\varepsilon^{(H)} &= \varepsilon_t^{(H)} - \varepsilon_b^{(H)} \qquad\qquad \text{(C.36)} \\
&= \frac{g_s}{\Omega}\sum_{\boldsymbol{k}'}\big(V_{t,t}(0) - V_{t,b}(0)\big)\big(\langle c^\dagger_{\boldsymbol{k}',t}c_{\boldsymbol{k}',t}\rangle - \langle c^\dagger_{\boldsymbol{k}',b}c_{\boldsymbol{k}',b}\rangle\big) \\
&= g_s\left(\frac{e^2}{2a_B}\right)\left(\frac{d}{a_B}\right)\left(\frac{S_{\boldsymbol{k}}a_B^2}{\pi}\right)\frac{1}{N_{\boldsymbol{k}}}\sum_{\boldsymbol{k}'}\Big(\langle c^\dagger_{\boldsymbol{k}',t}c_{\boldsymbol{k}',t}\rangle - \langle c^\dagger_{\boldsymbol{k}',b}c_{\boldsymbol{k}',b}\rangle\Big), \\
\Delta\varepsilon^{(F)}(\boldsymbol{k}) &= \varepsilon_t^{(F)}(\boldsymbol{k}) - \varepsilon_b^{(F)}(\boldsymbol{k}) \qquad\qquad \text{(C.37)} \\
&= -\frac{1}{\Omega}\sum_{\boldsymbol{k}'}V_{t,t}(\boldsymbol{k}'-\boldsymbol{k})\Big(\langle c^\dagger_{\boldsymbol{k}',t}c_{\boldsymbol{k}',t}\rangle - \langle c^\dagger_{\boldsymbol{k}',b}c_{\boldsymbol{k}',b}\rangle\Big) \\
&= -\left(\frac{e^2}{2a_B}\right)\left(\frac{S_{\boldsymbol{k}}a_B^2}{\pi}\right)\frac{1}{N_{\boldsymbol{k}}}\sum_{\boldsymbol{k}'}\frac{1}{|\boldsymbol{k}'-\boldsymbol{k}|a_B}\Big(\langle c^\dagger_{\boldsymbol{k}',t}c_{\boldsymbol{k}',t}\rangle - \langle c^\dagger_{\boldsymbol{k}',b}c_{\boldsymbol{k}',b}\rangle\Big), \\
\varepsilon_{bt}^{(F)}(\boldsymbol{k}) &= -\frac{1}{\Omega}\sum_{\boldsymbol{k}'}V_{t,b}(\boldsymbol{k}'-\boldsymbol{k})\langle c^\dagger_{\boldsymbol{k}',t}c_{\boldsymbol{k}',b}\rangle \qquad\qquad \text{(C.38)} \\
&= -\left(\frac{e^2}{2a_B}\right)\left(\frac{S_{\boldsymbol{k}}a_B^2}{\pi}\right)\frac{1}{N_{\boldsymbol{k}}}\sum_{\boldsymbol{k}'}\frac{e^{-|\boldsymbol{k}'-\boldsymbol{k}|d}}{|\boldsymbol{k}'-\boldsymbol{k}|a_B}\langle c^\dagger_{\boldsymbol{k}',t}c_{\boldsymbol{k}',b}\rangle,
\end{aligned}$$

where $S_{\boldsymbol{k}}$ is an area of integration in $\boldsymbol{k}$ space and $N_{\boldsymbol{k}}$ is the number of $\boldsymbol{k}$ points within $S_{\boldsymbol{k}}$. Here $(\Omega/N_{\boldsymbol{k}})S_{\boldsymbol{k}} = (2\pi)^2$ was used, and for a length unit, Bohr radius a_B was used.

Appendix D

Two-component Formalism

D.1 Hamiltonian

Let's consider a general two-component Hamiltonian of the following form:

$$\begin{aligned} H = \boldsymbol{a}\cdot\boldsymbol{\tau} &= \begin{pmatrix} a_3 & a_1 - ia_2 \\ a_1 + ia_2 & -a_3 \end{pmatrix} \\ &= a\begin{pmatrix} \cos\theta & \sin\theta e^{-i\phi} \\ \sin\theta e^{i\phi} & -\cos\theta \end{pmatrix}, \end{aligned} \tag{D.1}$$

where $a = \sqrt{a_1^2 + a_2^2 + a_3^2}$, $\tan\theta = \frac{\sqrt{a_1^2+a_2^2}}{a_3}$ and $\tan\phi = \frac{a_2}{a_1}$.

The Hamiltonian has a simple spectra given by $\epsilon_\pm = a_0 \pm a$ and corresponding eigenfunctions are

$$|+\rangle = \begin{pmatrix} \cos\frac{\theta}{2}e^{-i\phi/2} \\ \sin\frac{\theta}{2}e^{i\phi/2} \end{pmatrix}, |-\rangle = \begin{pmatrix} -\sin\frac{\theta}{2}e^{-i\phi/2} \\ \cos\frac{\theta}{2}e^{i\phi/2} \end{pmatrix}. \tag{D.2}$$

Note that the eigenfunctions are nothing but a rotated spin up and spin down states about the y-axis by θ and subsequently by angle ϕ about the z-axis.

The density matrix of the eigenfunctions are given by

$$\begin{aligned} \boldsymbol{\rho}_+ &= \begin{pmatrix} \frac{1}{2}(1+\cos\theta) & \frac{1}{2}\sin\theta e^{-i\phi} \\ \frac{1}{2}\sin\theta e^{i\phi} & \frac{1}{2}(1-\cos\theta) \end{pmatrix}, \\ \boldsymbol{\rho}_- &= \begin{pmatrix} \frac{1}{2}(1-\cos\theta) & -\frac{1}{2}\sin\theta e^{-i\phi} \\ -\frac{1}{2}\sin\theta e^{i\phi} & \frac{1}{2}(1+\cos\theta) \end{pmatrix}. \end{aligned} \tag{D.3}$$

Pauli matrices in the eigenfunction basis are given by

$$\begin{aligned}
\tau_x &= \begin{pmatrix} \sin\theta\cos\phi & \cos\theta\cos\phi + i\sin\phi \\ \cos\theta\cos\phi - i\sin\phi & -\sin\theta\cos\phi \end{pmatrix}, \qquad (D.4) \\
\tau_y &= \begin{pmatrix} \sin\theta\sin\phi & \cos\theta\sin\phi - i\cos\phi \\ \cos\theta\sin\phi + i\cos\phi & -\sin\theta\sin\phi \end{pmatrix}, \\
\tau_z &= \begin{pmatrix} \cos\theta & -\sin\theta \\ -\sin\theta & -\cos\theta \end{pmatrix}.
\end{aligned}$$

D.2 Green's function

The retarded Green's function is defined by

$$\begin{aligned}
G^R(\epsilon) &= \frac{1}{\epsilon - H + i\eta} \qquad (D.5) \\
&= \frac{\epsilon - a_0 + \boldsymbol{a}\cdot\boldsymbol{\tau}}{\big(\epsilon - \epsilon_+ + i\eta\big)\big(\epsilon - \epsilon_- + i\eta\big)} \\
&\equiv G^R_s(\epsilon) + G^R_t(\epsilon)\boldsymbol{n}\cdot\boldsymbol{\tau}
\end{aligned}$$

where $\boldsymbol{n} = \boldsymbol{a}/a$ and

$$\begin{aligned}
G^R_s(\epsilon) &= \frac{1}{2}\left(\frac{1}{\epsilon - \epsilon_+ + i\eta} + \frac{1}{\epsilon - \epsilon_- + i\eta}\right), \qquad (D.6) \\
G^R_t(\epsilon) &= \frac{1}{2}\left(\frac{1}{\epsilon + \epsilon_+ - i\eta} - \frac{1}{\epsilon - \epsilon_- + i\eta}\right).
\end{aligned}$$

D.3 Berry curvature

Let's assume that the Hamiltonian has the following $\boldsymbol{k}$ dependence:

$$H = a_0(\boldsymbol{k}) + \boldsymbol{a}(\boldsymbol{k})\cdot\boldsymbol{\tau}. \qquad (D.7)$$

The Berry curvature of n-th band along z at $\boldsymbol{k}$ is defined by

$$\begin{aligned}\Omega_{n,z}(\boldsymbol{k}) &= i\left(\left\langle \frac{\partial u_n}{\partial k_x}\middle| \frac{\partial u_n}{\partial k_y}\right\rangle - \left\langle \frac{\partial u_n}{\partial k_y}\middle| \frac{\partial u_n}{\partial k_x}\right\rangle\right) \\ &= -2\sum_{n'\neq n} \frac{Im \left\langle u_n\right| \hbar v_x \left|u_{n'}\right\rangle \left\langle u_{n'}\right| \hbar v_y \left|u_n\right\rangle}{\left(\epsilon_n - \epsilon_{n'}\right)^2},\end{aligned} \tag{D.8}$$

where $\boldsymbol{v} = \frac{\partial H}{\hbar \partial \boldsymbol{k}}$. Using the Pauli matrices in the eigenfunction basis in Eq. (D.4), we obtain

$$\begin{aligned}\Omega_{\pm,z}(\boldsymbol{k}) &= \mp\frac{1}{2a^3}\left[J(a_1,a_2)a_3 + J(a_2,a_3)a_1 + J(a_3,a_1)a_2\right] \\ &= \mp\frac{1}{2a^3}\boldsymbol{a}\cdot\partial_x\boldsymbol{a}\times\partial_y\boldsymbol{a},\end{aligned} \tag{D.9}$$

where $J(\alpha,\beta) = \partial_x\alpha\partial_y\beta - \partial_x\beta\partial_y\alpha$ and $\partial_i \equiv \partial/\partial k_i$.

Similarly, the spin Berry curvature of n-th band along z at $\boldsymbol{k}$ can be defined by

$$\Omega^{spin}_{n,z}(\boldsymbol{k}) = -2\sum_{n'\neq n} \frac{Im \left\langle u_n\right| \hbar v^z_x \left|u_{n'}\right\rangle \left\langle u_{n'}\right| \hbar v_y \left|u_n\right\rangle}{\left(\epsilon_n - \epsilon_{n'}\right)^2}, \tag{D.10}$$

where $v^z_x = \frac{1}{2}\{\sigma_z, v_x\}$. For the Hamiltonian in Eq. (D.7), the spin Berry curvature is given by

$$\Omega^{spin}_{\pm,z}(\boldsymbol{k}) = \pm\frac{\partial_x a_0}{2a^3}\left(a_1\partial_y a_2 - a_2\partial_y a_1\right). \tag{D.11}$$

As an example, let's consider the following Hamiltonian:

$$H = \epsilon^{(0)}_{\boldsymbol{k}} + \alpha\left(\tau_x k_y - \tau_y k_x\right) + \beta\left(\tau_x k_x - \tau_y k_y\right) + B\tau_z \tag{D.12}$$

where $\epsilon^{(0)}_{\boldsymbol{k}} = \frac{\hbar^2\boldsymbol{k}^2}{2m}$. Its energy spectrum is given by $\epsilon_{\boldsymbol{k},\pm} = \epsilon^{(0)}_{\boldsymbol{k}} \pm \Delta_{\boldsymbol{k}}$ where $\Delta_{\boldsymbol{k}} = \sqrt{(\alpha^2+\beta^2)k^2 + 4\alpha\beta k_x k_y + B^2}$.

From Eq. (D.9) and Eq. (D.11),

$$\begin{aligned} \Omega_{\pm,z}(\boldsymbol{k}) &= \mp\frac{B}{2\Delta_{\boldsymbol{k}}^3}\big(\alpha^2-\beta^2\big), \\ \Omega_{\pm,z}^{spin}(\boldsymbol{k}) &= \pm\frac{\hbar^2k_x^2}{2m\Delta_{\boldsymbol{k}}^3}\big(\alpha^2-\beta^2\big). \end{aligned} \tag{D.13}$$

Then corresponding Chern numbers are

$$\begin{aligned} C_- &= \int_{k<k_F}\frac{d^2k}{2\pi}\Omega_{-,z}(\boldsymbol{k}) \approx -\frac{1}{2}, \\ C_-^{spin} &= \int_{k<k_F}\frac{d^2k}{2\pi}\Omega_{-,z}^{spin}(\boldsymbol{k}) \approx \frac{1}{2}, \end{aligned} \tag{D.14}$$

giving the anomalous Hall conductivity $\sigma^{AHE} = -\frac{1}{2}\frac{e^2}{h}$ and spin Hall conductivity $\sigma^{SHE} = \frac{1}{2}\frac{e}{4\pi}$, respectively.

Bibliography

[1] A. K. Geim and K. S. Novoselov. *Nature Mat.*, 6:183, 2007.

[2] A. K. Geim and A. H. MacDonald. *Phys. Today*, 60(8):35, 2007.

[3] Mikhail I. Katsnelson. *Mater. Today*, 10:20, 2007.

[4] K. S. Novoselov, A. K. Geim, S. V. Morozov, D. Jiang, Y. Zhang, S. V. Dubonos, I. V. Grigorieva, and A. A. Firsov. *Science*, 306:666, 2004.

[5] K. S. Novoselov, D. Jiang, F. Schedin, T. J. Booth, V. V. Khotkevich, S. V. Morozov, and A. K. Geim. *Proc. Natl Acad. Sci. USA*, 102:10451, 2005.

[6] Y. Zhang, J. P. Small, M. E. S. Amori, and P. Kim. *Phys. Rev. Lett.*, 94:176803, 2005.

[7] C. Berger, Z. Song, T. Li, X. Li, A. Y. Ogbazghi, R. Feng, Z. Dai, A. N. Marchenkov, E. H. Conrad, P. N. First, and W. A. de Heer. *J. Phys. Chem B*, 108:19912, 2004.

[8] C. L. Kane and E. J. Mele. *Phys. Rev. Lett.*, 95:226801, 2005.

[9] C. L. Kane and E. J. Mele. *Phys. Rev. Lett.*, 95:146802, 2005.

[10] G. W. Semenoff. *Phys. Rev. Lett.*, 53:2449, 1984.

[11] F. D. M. Haldane. *Phys. Rev. Lett.*, 61:2015, 1988.

[12] V. P. Gusynin and S. G. Sharapov. *Phys. Rev. Lett.*, 95:146801, 2005.

[13] N. A. Sinitsyn, J. E. Hill, Hongki Min, Jairo Sinova, and A. H. MacDonald. *Phys. Rev. Lett.*, 97:106804, 2006.

[14] R. Saito, G. Dresselhaus, and M. S. Dresselhaus. *Physical Properties of Carbon Nanotubes.* Imperial College Press, London, 1998.

[15] Mark Wilson. *Phys. Today*, 59(1):21, 2006.

[16] K. S. Novoselov, A. K. Geim, S. V. Morozov, D. Jiang, M. I. Katsnelson, I. V. Grigorieva, S. V. Dubonos, and A. A. Firsov. *Nature*, 438:197, 2005.

[17] Y. Zhang, Y.-W. Tan, H. L. Stormer, and P. Kim. *Nature*, 438:201, 2005.

[18] M. Y. Han, B. Őzyilmaz, Y. Zhang, and P. Kim. *Phys. Rev. Lett.*, 98:206805, 2007.

[19] J. C. Slater and G. F. Koster. *Phys. Rev.*, 94:1498, 1954.

[20] Leonard I. Schiff. *Quantum Mechanics.* McGraw-Hill Company, New York, 1968.

[21] R. Saito, M. Fujita, G. Dresselhaus, and M. S. Dresselhaus. *Phys. Rev. B*, 46:1804, 1992.

[22] W. Kohn and L. Sham. *Phys. Rev.*, 140:A1133, 1965.

[23] P. E. Blőchl. *Phys. Rev. B*, 50:17953, 1994.

[24] J. P. Perdew, K. Burke, and M. Ernzerhof. *Phys. Rev. Lett.*, 77:3865, 1996.

[25] G. Kresse and J. Furthműller. *Phys. Rev. B*, 54:11169, 1996.

[26] J. T. Waber and Don. T. Cromer. *J. Chem. Phys.*, 42:4116, 1965.

[27] K. S. Novoselov, E. McCann, S. V. Morozov, V.I.Fal'ko, M. I. Katsnelson, U. Zeitler, D. Jiang, F. Schedin, and A. K. Geim. *Nat. Phys.*, 2:177, 2006.

[28] Sylvain Latil and Luc Henrard. *Phys. Rev. Lett.*, 97:036803, 2006.

[29] B. Partoens and F. M. Peeters. *Phys. Rev. B*, 74:075404, 2006.

[30] Edward McCann and Vladimir I. Fal'ko. *Phys. Rev. Lett.*, 96:086805, 2006.

[31] Edward McCann. *Phys. Rev. B*, 74:161403(R), 2006.

[32] T. Ohta, A. Bostwick, T. Seyller, K. Horn, and E. Rotenberg. *Science*, 313:951, 2006.

[33] E V. Castro, K. S. Novoselov, S. V. Morozov, N. M. R. Peres, J. M. B. Lopes dos Santos, J. Nilsson, F. Guinea, A. K. Geim, and A. H. Castro Neto. *Phys. Rev. Lett.*, 99:216802, 2007.

[34] P. Blaha, K. Schwarz, G. K. H. Madsen, D. Kvasnicka, and J. Luitz. *WIEN2K, An Augmented Plane Wave+Local Orbitals Program for Calculating Crystal Properties.* Techn. Universitắt Wien, Vienna, Austria, 2001.

[35] J. Stahn, U. Pietsch, P. Blaha, and K. Schwarz. *Phys. Rev. B*, 63:165205, 2001.

[36] J. Hass, J. E. Millán-Otoya F. Varchon, M. Sprinkle, N. Sharma, W. A. de Heer, C. Berger, P. N. First, L. Magaud, and E. H. Conrad. *Phys. Rev. Lett.*, 100:125504, 2008.

[37] J. C. Charlier, J. P. Michenaud, and X. Gonze. *Phys. Rev. B*, 46:4531, 1992.

[38] P. D. Ritger and N. J. Rose. *Differential Equations with Applications.* McGraw-Hill Book Company, New York, 1968.

[39] F. Guinea, A. H. Castro Neto, and N. M. R. Peres. *Phys. Rev. B*, 73:245426, 2006.

[40] J. J. Sakurai. *Modern Quantum Mechanics.* Addison Wesley, Reading, 1994.

[41] M. Koshino and T. Ando. *Phys. Rev. B*, 085425:76, 2007.

[42] J. L. Maňes, F. Guinea, and M. A. H. Vozmediano. *Phys. Rev. B*, 75:155424, 2007.

[43] M. Nakamura and L. Hirasawa. *Phys. Rev. B*, 77:045429, 2008.

[44] D. A. Abanin, P. A. Lee, and L.S. Levitov. *Phys. Rev. Lett.*, 96:176803, 2006.

[45] K. Nomura and A. H. MacDonald. *Phys. Rev. Lett.*, 96:256602, 2006.

[46] J. Alicea and M. P. A. Fisher. *Phys. Rev. B*, 74:075422, 2006.

[47] M. O. Goerbig, R. Moessner, and B. Doucot. *Phys. Rev. B*, 74:161407(R), 2006.

[48] K. Yang, S. Das Sarma, and A. H. MacDonald. *Phys. Rev. B*, 74:075423, 2006.

[49] Y. Barlas, R. Cote, K. Nomura, and A. H. MacDonald. arXiv:0803.0044 (unpublished).

[50] G. F. Giuliani and G. Vignale. *Quantum Theory of the Electron Liquid.* Cambridge University Press, Cambridge, 2005.

[51] V. S. Pribiag, I. N. Krivorotov, G. D. Fuchs, P. M. Braganca, O. Ozatay, J. C. Sankey, D. C. Ralph, and R. A. Buhrman. *Nat. Phys.*, 3:498, 2007.

[52] Hongki Min, B. Sahu, S. K. Banerjee, and A. H. MacDonald. *Phys. Rev. B*, 75:155115, 2007.

[53] J. Nilsson, A. H. Castro Neto, N. M. R. Peres, and F. Guinea. *Phys. Rev. B*, 73:214418, 2006.

[54] J. Martin, N. Akerman, G. Ulbricht, T. Lohmann, J. H. Smet, K. von Klitzing, and A. Yacoby. *Nat. Phys.*, 4:144, 2008.

[55] J. M. Blatt, K. W. Bőer, and W. Brandt. *Phys. Rev.*, 126:1691, 1962.

[56] L. V. Keldysh and A. N. Kozlov. *Sov. Phys. JETP*, 27:521, 1968.

[57] I. B. Spielman, J. P. Eisenstein, L. N. Pfeiffer, and K. W. West. *Phys. Rev. Lett.*, 84:5808, 2000.

[58] J. P. Eisenstein and A. H. MacDonald. *Nature*, 432:691, 2004.

[59] L. V. Butov. *J. Phys. Condens. Matt.*, 19:295202, 2007.

[60] J. Kasprzak, M. Richard, S. Kundermann, A. Baas, P. Jeambrun, J. M. J. Keeling, F. M. Marchetti, M. H. Szymańska, R. André, J. L. Staehli, V. Savona, P. B. Littlewood, B. Deveaud, and Le Si Dang. *Nature*, 443:409, 2006.

[61] D. Sarchi and V. Savona. *Solid State Commun.*, 144:371, 2007.

[62] Y. E. Lozovik and A. G. Semenov. *JETP Letters*, 86:28, 2007.

[63] J. A. Seamons, D. R. Tibbetts, J. L. Reno, and M. P. Lilly. *Appl. Phys. Lett.*, 90:052103, 2007.

[64] K. Das Gupta, M. Thangaraj, A.F. Croxall, H.E. Beere, C.A. Nicoll, D.A. Ritchie, and M. Pepper. *Physica E*, 40:1693, 2008.

[65] K. Moon, H. Mori, K. Yang, S. M. Girvin, A. H. MacDonald, L. Zheng, D. Yoshioka, and S.-C. Zhang. *Phys. Rev. B*, 51:5138, 1995.

[66] A. V. Balatsky, Y. N. Joglekar, and P. B. Littlewood. *Phys. Rev. Lett.*, 93:266801, 2004.

[67] J.-J. Su and A.H. MacDonald. arXiv:0801.3694 (to appear in Nat. Phys.).

[68] Hongki Min, G. Borghi, M. Polini, and A. H. MacDonald. *Phys. Rev. B*, 77:041407(R), 2008.

[69] Y. Barlas, T. Pereg-Barnea, M. Polini, R. Asgari, and A. H. MacDonald. *Phys. Rev. Lett.*, 98:236601, 2007.

[70] H. Heiselberg, C. J. Pethick, H. Smith, and L. Viverit. *Phys. Rev. Lett.*, 85:2418, 2000.

[71] A. R. Champagne, J. P. Eisenstein, L. N. Pfeiffer, and K. W. West. *Phys. Rev. Lett.*, 100:096801, 2008.

[72] S. De Palo, F. Rapisarda, and Gaetano Senatore. *Phys. Rev. Lett.*, 88:206401, 2002.

[73] E. Bascones, A. A. Burkov, and A. H. MacDonald. *Phys. Rev. Lett.*, 89:086401, 2002.

[74] M. Y. Veillette and L. Balents. *Phys. Rev. B*, 65:014428, 2001.

[75] Yong-Il Shin, Christian H. Schunck, André Schirotzek, and Wolfgang Ketterle. *Nature*, 451:689, 2008.

[76] S. H. Abedinpour, M. Polini, A. H. MacDonald, B. Tanatar, M. P. Tosi, and G. Vignale. *Phys. Rev. Lett.*, 99:206802, 2007.

[77] M. C. Payne, M. P. Teter, D. C. Allan, T. A. Arias, and J. D. Joannopoulos. *Rev. Mod. Phys.*, 64:1045, 1992.

[78] Richard M. Martin. *Electronic structure: basic theory and practical methods.* Cambridge University Press, Cambridge, 2004.

Index

ab initio theory
    graphene bilayers, 26
    graphene monolayers, 17
    review, 118

abstract, vii
acknowledgments, v
appendices, 113

bibliography, 145

chiral decomposition table, 68
collective-electron device scheme, 110
conclusion, 110
Cooper instability, 97
counter flow, 104

dedication, iv
density functional theory, 118
device
    energy band gap control, 25
    exciton condensation, 98

effective Hamiltonian
    AB stacking, 70
    ABC stacking, 55, 69
    ABC+B stacking, 72
    arbitrary stacking, 74
    graphene bilayers, 36, 84
    graphene monolayers, 14, 68
energy band gap control
    by gate voltage, 30
    by quantum confinement, 4
energy band structure
    AA stacking, 50
    AB stacking, 53
    ABC stacking, 56
    arbitrary stacking, 57
    graphene bilayers, 29
    graphene monolayers, 18
exchange-correlation, 122

graphene
    bilayers, 23
    monolayers, 1
    multilayers, 46

Hartree-Fock theory
    exciton condensation, 101
    pseudospin magnetism, 86
    review, 126
Hohenberg-Kohn theorem, 118

introduction, 1

Kohn-Sham equation, 119
Kosterlitz-Thouless temperature, 104

Landau level spectrum
    AA stacking, 59
    AB stacking, 61
    ABC stacking, 63
    arbitrary stacking, 64
    as a function of γ_2, 78
    as a function of γ_3, 77
linearized gap equation
    exciton condensation, 104
    pseudospin magnetism, 88

momentum-space vortex, 85, 95

outline, 4

perturbation theory
  2nd order degenerate state, 14
  Nth order degenerate state, 69
phase diagram
  exciton condensation, 100, 105
  pseudospin magnetism, 90
phase stiffness, 104
Poisson equation, 33
pseudopotential theory, 123

quantum Hall effect
  graphene monolayers, 2
  graphene multilayers, 79
  quantization, 66
quantum spin Hall effect, 21

screening in graphene bilayers, 35
spin-orbit interactions
  atomic, 12
  intrinsic, 17
  Rashba, 21
stacking diagram, 47
stacking rules, 66

tight-binding Hartree theory, 37
tight-binding model
  chain, 48
  $eE_{ext}z$ matrix elements, 13
  graphene monolayers, 10
  Hamiltonian matrix elements, 117
  Hamiltonian matrix elements at K/K', 14
  hopping parameters, 16
  $\boldsymbol{L} \cdot \boldsymbol{S}$ matrix elements, 12
  review, 114
  two-center approximation, 116
  two-center matrix elements, 11
two-component formalism, 134

work function, 28

Vita

Hongki Min was born in Seoul, Korea on April 6th, 1976, the son of Byoung-mook Min and Sook-ja Hwang. He received the Bachelor of Science degree in Physics from Seoul National University in February, 2001. He entered the Graduate School of the University of Texas at Austin in August, 2001.

Permanent address: Department of Physics
The University of Texas at Austin
1 University Station C1600
Austin Texas 78712

This dissertation was typeset with LaTeX[†] by the author.

[†] LaTeX is a document preparation system developed by Leslie Lamport as a special version of Donald Knuth's TeX Program.